Computer Modelling of Virtual Cathode Oscillators (Vircators)

P. A. Lindsay
X. Chen
J. Watkins
W. K. Toh

28th February 2003

Final Report
15th January 2000 – 30th November 2002

28th February 2003   Final: 15th Jan 2000 – 30th November 2002

Computer Modelling of Virtual Cathode Oscillator (Vircator)

P. A. Lindsay
X. Chen
J. Watkins
W. K. Toh

US Air Force Office of Scientific
Research (AFOSR) - NE
4015 Wilson Blvd
Room 713, Arlington
VA 22203 – 1954 USA

European Office of Aerospace
Research And Development,
223/231 Old Marylebone Rd
London NW1 5TH UK

20030610 120

REPORT DOCUMENTATION PAGE

AFRL-SR-AR-TR-03-

0087

Public reporting burden for this collection of information is estimated to average 1 hour per response, including the time for re the data needed, and completing and reviewing this collection of information. Send comments regarding this burden estimat reducing this burden to Washington Headquarters Services, Directorate for Information Operations and Reports, 1215 Jeffer Management and Budget, Paperwork Reduction Project (0704-0188), Washington, DC 20503

1. AGENCY USE ONLY (Leave blank)	2. REPORT DATE 28-02-2003	3. REPORT TYPE AND DATES COVERED Final Report: 15 Jan 2000 – Nov 2002	

4. TITLE AND SUBTITLE	5. FUNDING NUMBERS
Computer Modelling of virtual Cathode Oscillators (Vircators)	F49620-00-1-0157

6. AUTHOR(S)

Lindsay, Peter A.
Chen, Xiaodong
Watkins, John   and   Toh, Weekian

7. PERFORMING ORGANIZATION NAME(S) AND ADDRESS(ES)	8. PERFORMING ORGANIZATION REPORT NUMBER
Queen Mary, University of London (QMUL) Mile End Road London E1 4NS, UK	--

9. SPONSORING / MONITORING AGENCY NAME(S) AND ADDRESS(ES)	10. SPONSORING / MONITORING AGENCY REPORT NUMBER
US Air Force Office of Scientific Research (AFOSR) - NE 4015 Wilson Blvd Room 713, Arlington VA 22203 - 1954 U S A	European Office of Aerospace Research and Development, 223/231 Old Marylebone Rd London NW1 5TH UK	--

11. SUPPLEMENTARY NOTES

--

12a. DISTRIBUTION / AVAILABILITY STATEMENT	12b. DISTRIBUTION CODE
Approved for public release; Distributed unlimited.	--

13. ABSTRACT (Maximum 200 Words)

This final report covers the results of investigations extending over the period 15 Jan 2000 – 30 Nov 2002. The report consists of two parts, in Part 1 a computer model of a vircator developed at the Texas Technical University is developed using a powerful code called MAGIC. Part 1 ends with design proposals leading to an increase in power output of 52 %. Part 2 is primarily concerned with the influence of an axial magnetic field on the performance of a coaxial vircator, including stability investigations.

14. SUBJECT TERMS High Power Microwaves, Vircators, Computer modeling, Beam Stability	15. NUMBER OF PAGES 153
	16. PRICE CODE

17. SECURITY CLASSIFICATION OF REPORT U	18. SECURITY CLASSIFICATION OF THIS PAGE U	19. SECURITY CLASSIFICATION OF ABSTRACT U	20. LIMITATION OF ABSTRACT UU

NSN 7540-01-280-5500

Standard Form 298 (Rev. 2-89)
Prescribed by ANSI Std. Z39-18
298-102

Abstract

This final report covers the results of investigations extending over the period 15 Jan 2000 – 30 Nov 2002. The report consists of two parts, in Part 1 a computer model of a vircator developed at the Texas Technical University is developed using a powerful code called MAGIC. Part 1 ends with design proposals leading to an increase in power output of 52 %. Part 2 is primarily concerned with the influence of an axial magnetic field on the performance of a coaxial vircator, including stability investigations.

Content

Summary

This is the Final Report covering the results of investigations extending over an approximately three year period, 15 Jan 99 – 30 Nov 2002. The Report is divided into two parts. In Part 1 computer model of a coaxial vircator is discussed in some detail, whereas Part 2 is solely devoted to the investigation of the effect that an axial magnetic field has on the performance of such a vircator.

In Part 1 a powerful computer code called MAGIC is used to model a coaxial vircator under development at the Texas Technical University (TTU) in Lubbock, TX. This required close collaboration with the team at TTU developing the device and involved exchange visits. The first seven months were spent on establishing the contact and developing an early computer model of the device. In the following period of 12 months the model was refined by incorporating ongoing design changes introduced at TTU. This directly led to improved accuracy of modelling, the frequency of oscillations and the output power now being reproduced to within $\pm$ 5%. The remaining period of 16 months was devoted to some additional design alterations and a detailed investigation of the interaction process at the electron cloud level. With a better understanding of the operation of the vircator it then proved possible to improve the power output of the device by 52 % by redesigning the sensitive anode area of the tube.

In Part 2 the effect of an axial magnetic field on the performance of an axial vircator is discussed in considerable detail, the results of the investigations confirming the expectation that the magnetic field hinders the performance of the device. In the process

careful analysis of a *conducting* magnetic diode has been performed, revealing some hitherto overlooked solutions resembling those obtained in the absence of the magnetic field.

The report ends with suggestions for future work based on the results of the above investigations.

It should be added that the above investigations generated two papers (one of them in a special issue on High Power Microwave Generation) and five contributions at international conferences.

Part 1.

1.1 General Introduction

All our investigations have been carried out in close cooperation with a research group in the Department of Electrical Engineering and Physics at Texas Technical University in Lubbock, TX; the research group under the leadership of Prof. Magne Kristiansen was then in the process of developing an axial vircator [1,2] and our task was to provide a suitable computer modelling support, primarily by using MAGIC [3]. Since this was a cooperative effort, it proved important to establish a close contact with our colleagues at TTU. We did that even before submitting our proposal. Our friends in Lubbock helped us greatly by sending us engineering drawings covering the design of their vircator tube and we in turn included some of the drawings in our Proposal. We then met some members of the group, in particular Prof. M. Kristiansen, at the ICOPS99 conference in Monterey, CA. Since the award of the grant, we have further developed our contracts by one of us (X. Chen) visiting Lubbok early in June 2000 after attending the ICOPS 2000 conference in New Orleans, LA. The visit proved to be most valuable, since in computer modelling it is always important to see the relevant device *in situ*, possibly when actually operating. Dr. Chen was warmly welcomed and the hosts went out of their way to help and make the visit well worthwhile. In turn this greatly speeded up the process of setting up the correct computer model on the equipment at QMUL. In November 2001 we had the pleasure of a visit from Prof. M. Kristiansen, who was touring Europe. This gave us the opportunity of introducing the staff involved in computer modelling and show the substantial computer facilities available at QMUL. Finally in April 2002 Dr Chen and Mr Toh, a post graduate student chiefly involved in the vircator modelling, visited TTU on the way back from IVEC02 conference in Monterey, CA.

7

Virtual Cathode Oscillators (vircators) have been studied quite extensively over the last two decades [4-6]. In principle a vircator employs an intense, mostly relativistic electron beam, the density of the beam greatly exceeding that in a space-charge-limited diode [7,8]; this leads to the formation of an unstable virtual cathode, which then generates relaxation oscillations. In practice the device is capable of generating pulsed power at levels of several GW and in the GHz range of frequencies. The main merit of a vircator is its simplicity of construction, the device in principle comprising a cathode, a semitransparent anode, usually in the form of a metal mesh, followed by an output waveguide and a window, as shown schematically in Fig. 1, no magnetic field being required. Since a vircator uses a low impedance relativistic electron beam, theoretically there should be no limit to the power level at which it can operate, nonetheless its inherent broadband characteristic and a wide spread of electron energies renders it an oscillator of low electronic efficiency, usually below 5%. Thus the principle of generating microwave radiation using virtual cathode oscillations is conceptually quite simple, however the actual process is highly non-linear. Consequently all the earlier attempts at mathematically analyzing the interaction process suffered from a number of limitations [1,4,9-14]. It would appear therefore that computer modelling presents a better method for the study and understanding of vircators.

As a first step in our modelling it seemed prudent to agree on the basic geometry of the TTU vircator. Following Fig. 4 of ref. 1 and some additional discussions during our visit to Lubbock, the basic dimensions of the device, as shown in Fig. 2, have been established. Here the cathode and the anode are respectively in the form of two coaxial and partly overlapping cylinders. This constituted an important development of a simple axial vircator and it has been initially suggested some time ago by the Russians [17]. The advantages of such a system are twofold: on the one hand the area where the virtual

cathode is likely to be formed is better defined and hence easier to control, on the other hand the generation of a hollow beam removes some of the power limitations imposed by the existence of a solid beam. The dimensions of the two overlapping cylinders are as follows: the outer cylinder of 130 mm radius acts as a cathode and has a 3 cm wide velvet band on the inside acting as an emitter. The inner cylinder of 100 mm radius acts as an anode and is made from a 10 μm thick aluminum foil; the anode then continues as a cylindrical output waveguide of 98 mm internal radius. A 500 kV, 30 ns Gaussian pulse is applied to the diode section of the tube. Microwave oscillations are then generated near the cathode/anode section, the microwave radiation traveling down the output waveguide for some 1600 mm. The waveguide is supported at one end by a vertical flange and at the other end it has a plastic window which is permeable to microwave radiation. In addition a number of thin axial rods are placed on the inside of the anode drum to support the foil. They will be ignored in our model since they merely affect the degree of transparency of the anode and form an integral part of it.

1.2 Early investigations – 2D model

Early investigations cover the period of approx. seven months, from the beginning of the grant on 15 January 2000 till 31 July 2000. In our original Proposal under the heading 'Statement of Objectives' we have indicated that during the first year of the investigations we intend to establish close co-operation with our colleagues at TTU and using MAGIC set up a computer model of the vircator. We have completed the initial part of this task in the first seven months of our investigations and a brief summary of the results is given below. In this we have used the 2D version of MAGIC for the sake of simplicity. As pointed out in Section 1.1 it took us some time to develop the computer model based on Fig. 2, MAGIC being quite an elaborate code. We then decided to perform a number of simple tests.

1.2.1 Pulse delay

We noticed in Fig. 6 of ref. 1 that there was a time delay of some 20 ns between the electron-beam and microwave power pulses, the latter being measured with a probe near the output window. Using MAGIC we have decided to model this particular aspect of the system by observing the propagation of a wavepacket down a circular waveguide. Here the wavepacket is supposed to represent a microwave pulse. The waveguide was chosen to have the same dimensions as the cylindrical output waveguide of the vircator. Also, following ref. 1 it was assumed that the waveguide operated in the TE11 mode.

A Gaussian 2 GHz microwave pulse was then applied to a suitably placed dipole at one end of the waveguide. The corresponding transit time measured at the other end was $\tau_{model} = 6.44$ ns, the theoretical value for a TE11 mode being $\tau_{theoretical} = 5.60$ ns (the actual computations appear on p. 6 of ref. 18); as mentioned above the experimental

value of the delay was $\tau_{exp} = 20$ ns. The difference between the two sets of results could be explained by the fact that in practice it takes approx. 5-10 ns for the microwave pulse to be formed and the oscillations to begin.

This simple measurement acted as a primitive test of our model and also confirmed our correct use of MAGIC.

1.2.2 Frequency spectrum

Having gained some confidence in the more rudimentary performance of our model we then decided to investigate the actual microwave output and its frequency spectrum. The radial field component E_ρ as a function of time and the corresponding FFT are respectively shown in Figs. 7 and 8 of ref. 1, the measurements being taken with the help of a probe 8 mm long situated 1.5 m down the waveguide. In our simulation experiment we have managed to repeat the above result with limited degree of accuracy. Since the vertical scale in Fig. 7 of ref. 1 is not marked we could not compare the amplitude of oscillations with our Fig. 3a, but the waveform of the microwave output is fairly similar in the two cases. The FFT of the output waveform is shown in Fig. 3b. We find that the largest frequency peak occurs at 2.7 GHz as against 2 GHz in Fig. 8 of ref. 1. The difference of 35 % is almost certainly due to some structural simplifications of the early model and possibly due to the use of a 2D version of MAGIC. As we shall see later this difference was finally reduced to 2.5 % when we have used a more detailed model and a 3D version of MAGIC. As an additional precaution we moved our E_ρ observation point from the circumference to the centre of the waveguide, but the results were similar to those shown in Figs. 3a and b.

1.2.3 Output waveguide

As one more preliminary test of our model, we investigated the electromagnetic field distribution inside the output waveguide. We noted that the mode pattern remained fairly coherent only at the beginning of the pulse and it disintegrated quite rapidly afterwards. This was to be expected for two reasons: vircators are well known for their broad-band output, Fig. 3b being a good example. Secondly, as has been pointed out before the output waveguide is heavily overmoded, a situation which encourages the transfer of energy to higher order modes.

We find from Figs. 4a and 5a that in the early stages of oscillations the two dominant modes appear to be respectively TM01 and TE01. The early appearance of the TM01 mode should not surprise us in view of the existence of a strong E_ρ field component near the anode surface. The appearance of the TE01 mode could be caused by some asymmetry in the virtual cathode region giving rise to azimuthal components of the electric field. However it is not clear how it could be generated in our model, since at this stage we have been using a 2D version of MAGIC. However, the above results differed from the experimental probe measurements at TTU, where they were inclined to deduce the presence of a TE11 mode at the end of the waveguide. The test also confirmed the versatility of MAGIC as a computer code for modelling microwave devices.

1.3 Intermediate investigations

1.3.1 Introduction

Intermediate investigations cover the second year of the grant, starting on 1 August 2000 and ending on 31 July 2002. In order to improve the convergence of our results with those obtained at TTU we have carefully incorporated in our model all the structural changes dictated by experience and introduced by our colleagues at TTU during the first seven months of our cooperation. In addition we gained enough confidence in using MAGIC to change from 2D to 3D. As we shall see both changes had quite a dramatic effect on the accuracy and reliability of the results.

1.3.2 Improved TTU vircator model – 3D model

1.3.2a Design alternations

A number of alternations in the design of the vircator have been introduced at TTU during the first seven months of our investigations, the final design of the important gun section being, shown in Fig. 6. In particular a rectangular septum has been added in order to improve the performance of the device. The corresponding model of the final version of the device is shown in Fig. 7a, the septum being shown separately in Fig. 7b. The overall system now consists of a Marx generator followed by a pulse forming line feeding two coaxial electrodes through a spark gap. The vircator itself comprises a coaxial diode in the form of a metal cylinder supporting a velvet emitter of 132 mm inner radius and an internal cylindrical anode made from a stainless steel mesh of 60 % transparency and of 98 mm radius. At one end the mesh anode is strengthened by a metal wire ring (wire radius 2.5 mm) and at the other end it is attached to a flange and a 1.5 m long cylindrical waveguide which has an output window at the far end. Two

orthogonal probes are placed at the end of the waveguide for both mode detection and power measurement.

In operation a single pulse of 500 kV and 70 ns duration is applied across the electrodes. Typical experimental input voltage and current pulses are shown in Fig. 22, where the measured peak values are respectively 731 kV and 36.7 kA. An indication of the input impedance is obtained by dividing peak voltage by peak current which gives 19.9 Ω. Fig. 23 shows typical experimental input and microwave output power pulses, their respective peak values being 24.7 GW and 558 MW. The quality of our computer modelling using MAGIC will be judged by the degree of convergence with the above parameters.

1.3.2b Computational details

Let us now consider some computational details of the simulation process. The MAGIC code is very flexible and therefore well suited to achieve the required accuracy. Since the vircator exhibits a large degree of axial symmetry it was natural to choose polar (r,φ,z) co-ordinates for our modelling. Since we are now using a 3D version of MAGIC the total number of cells has gone up by a factor of 80, which is approx. the number of cells in the azimuthal direction. Although the size of $\delta\varphi$ and δz cells is fixed, the δr cells can be graded by choosing smaller values in regions of special interest. The choice of cell size governs the maximum permissible time step which for reasons of stability must satisfy the COURANT criterion

$$\chi^2 = c^2 (\delta t)^2 \frac{1}{(\delta s)^2} < 1 \qquad (1.1)$$

14

$$(\delta s)^2 = (\delta r)^2 + (r\delta\varphi)^2 + (\delta z)^2$$

Here c is the velocity of light and δt the time step. Since the total number of cells is quite large, the overall time of a simulation run frequently last as much as 24 hours, even with powerful modern PC computers.

In practice the emitter is in the form of a bobin of velvet glued to the inside of the cathode cylinder, its action being that of a field emitter. The EXPLOSIVE EMITTER command in MAGIC is well suited to simulate the performance of such a cathode. In our model it is assumed that the thickness of the emitter and its emission efficiency are both uniform around the circumference. The anode of the vircator is in the form of a light metal mesh supported by eighty thin metal rods (not shown) and a thick metal ring. The simulation of the anode structure is based on another MAGIC command called FOIL, the command ensuring 60 % transparency to the electron stream in close agreement with experimental results.

In order to improve the performance of the vircator a rectangular septum has been introduced, as shown in Figs. 6, 7a & b. In principle there are two ways of modelling the septum: we can use either Cartesian, Fig. 8a or polar coordinates, Fig. 8b. When Cartesian coordinates are used, the septum has smooth edges but the cylindrical walls of the waveguide are quite rough, the accuracy of modelling now strongly depending on the size of δx and δy cells. In polar coordinates, the cylindrical walls remains smooth, but the shape of the septum is now critically dependent on the size of δφ and δr cells. Since we have decided to use polar coordinates anyhow, it was only natural to follow Fig. 8b in

modelling the septum. Also the angular cell size δφ was chosen to be 0.0785 radians, which corresponds to 80 cells around the circumference of the cylinder. The use of 80 cells for the angular resolution, together with a large number of δr and δz cells required computer runs often in excess of 12 hours.

We now have to consider the problem of power supplies and the modelling of the feed system. At TTU a Marx generator supplies a 500kV, 70 ns pulse. In our simulations we use a voltage pulse of the same amplitude but with an exponential rise time given by

$$V(t) = V_0 \left(1 - \exp\left(-t/T_0\right)\right), \quad V_1 = 500 \text{kv}, \, T_0 = 4.0 \text{ ns} \tag{1.2}$$

followed by an abrupt fall. Figs. 9a-d show different ways of connecting power supplies to the system. The first three have been rejected in favour of the fourth, since they are too near to the excitation (virtual cathode) region and additionally in Fig. 9c, the feed is orthogonal to the desired direction. Accordingly Fig. 9d with its coaxial feed geometry and clear separation from the general excitation region is the preferred method. Here the length of the separate feed channel needs to be taken into account when comparing the delay between the excitation and the output pulse appearing at the end of the waveguide.

Lastly let us consider TTU measurement techniques. Two perpendicular probes situated 1.5m down the wave guide were used to monitor the output with the help of a Hewlett Packard 8GHz digital oscilloscope HP54720D and an HP8719C network analyser. The microwave power generated by the vircator was then obtained by taking into account the attenuation of the probes, the cables, the connectors, the fixed attenuators and the crystal detectors. The corresponding frequency spectrum was obtained by applying a fast

Fourier transform (FFT) to the waveform directly recorded by a digital oscilloscope. As an example typical experimental results obtained at TTU are shown in Figs. 10a and b.

At this point we should compare Figs. 3b and 10b, the difference being mostly due to the introduction of the rectangular septum. The effect is quite dramatic, the frequency spectrum in Fig. 10b being much cleaner than in Fig. 3b, the septum presumably acting as a quasi-cavity. At the same time the main resonant frequency was shifted downwards from 2.7 to 1.834 GHz.

1.3.3 Testing of the new model

Having obtained information on the latest changes in the design of the vircator, as explained in Section 1.3.2a, we have decided to put our new model to the test by repeating the latest results conveyed to us by the TTU team and respectively shown in Figs. 10a & b.

1.3.3a Power and efficiency

Let us consider a particular simulation run, using the feed system of Fig. 9d where a voltage of 500kV would be applied between cathode and anode resulting in an input power characteristic shown in Fig. 11; here the value of T_0 in (1.2) was chosen to be 4.0 ns(rise time characteristic), the input reaching a steady state input power of 7.80 GW. In Fig. 12 we have the microwave output power measured over the cross-section of the waveguide near the window. There is a delay of some 20 ns in the rise of output power due to the time it takes for the pulse to travel from the generator through the coaxial feed system, the emitter anode space and along the waveguide, before reaching the observation probes. The shape of the output power pulse roughly follows that of the

17

input power. Taking the value of 160 MW for the output power the device efficiency is of the order of 2.0% – a typical figure for a vircator and very close to the experimental value quoted by TTU (see also Fig. 23). The resulting radial component of the electric field E_ρ at a point near the centre of the exit plane of the waveguide can be seen in Fig. 13a, its frequency spectrum (FFT) being shown in Fig. 13b.

The above results allow us to compare the experimental and simulation performance of the device. In Figs. 10a and 13a, we have the electric field component E_ρ at the output plane. Allowing for the fact that a Gaussian-shaped input voltage pulse was applied in the experimental case and a steady voltage reached by an exponential rise in the simulation runs, there is reasonable agreement between the two results. Figs 10b and 13b respectively show frequency spectra of the two cases. It can be seen that not surprisingly, a 'cleaner' response is obtained in computer simulation than in the actual experimental results; also the main resonant frequencies agree remarkably well to within 1%. All this indicates that good accuracy can be obtained by using MAGIC for modelling the operation of a vircator.

1.3.3b Size of cathode to anode gap

In this brief test we have investigated the influence that the size of the cathode to anode gap has on the frequency of oscillations. In order to allow for the thickness of the velvet emitter its height was set to be equal to two radial cells, as show in Figs. 9a – d. However, this effectively reduces the cathode to anode gap by ~ 1.0 cm and causes an upward shift in the oscillation frequency [19]. We have therefore decided to investigate the effect, the results being summarised in Table 1.1.

Table 1.1 Effect of the cathode to anode gap on the resonant frequency.

Height of emitter	1.0cm (two cells)	0.5 cm (one cell)	0.0 cm (0 cell)
Cathode/anode gap	3.2 cm	3.7 cm	4.2 cm
Main frequency	1.988 GHz	1.963 GHz	1.816 GHz

One can see that the operation frequency of the vircator is critically dependent on the size of the cathode to anode gap. When the gap is close to that in the experimental set up (zero height of the emitter), we find from Figs. 10b and 13b that the simulated frequency agrees to within 1% with the measured one.

1.3.3c Presence of the anode ring

A thick metal ring is mounted at the far end of the support rods (not shown) to add strength to the fragile anode mesh, as shown in Figs. 6 and 7a. When the ring is removed, there is a slight upward shift in the resonant frequency, as shown in the last line of Table 1.2.

Table 1.2 Frequency shift when the anode support ring has been removed.

Height of emitter	1.0 cm (two cells)	0.5 cm (one cell)	0.0 cm (0 cell)
Cathode/anode gap	3.2 cm	3.7 cm	4.2 cm
Main frequency	2.138 GHz	2.045 GHz	1.853 GHz

Again we find that the removal of the anode support ring has a direct bearing on the resonance frequency of the vircator. The results of Tables 1.1 and 1.2 are plotted in Fig. 14. One can see that the size of the cathode/anode gap would affect the transit time of the electrons and thus the oscillation frequency of the vircator. Similarly the presence or absence of the support ring would strongly affect the electric field in the sensitive interaction region of the vircator and thus influence the electron dynamics of the system. Thus, as was to be expected, the above investigations have confirmed the fact that the operation frequency of the vircator is critically influenced by the fields prevailing in the interaction region and the related electron dynamics (see also Section 1.3.3d and 1.4.1). This point further emphasizes the difficulties associated with attempts to investigate the performance of a vircator analytically (see also Section 1.4.2d).

1.3.3d Position and size of the septum

As shown in Figs. 6 and 7a, b a rectangular septum has been added to the TTU vircator. In general a septum can be regarded as a circuit element designed to improve the performance of a vircator by forming a quasi cavity. In Fig. 6 the distance between the vertical part of the cathode structure and the septum is 11.4 cm; this would constitute a half-wavelength at 1.59 GHz (TE11 mode) or at 1.76 GHz (TM01 mode), the latter being nearer to both measured and simulated values. There are however other factors to be taken into consideration, principally the presence 80 very thin anode supporting rods (not included in the model) and the electron cloud which would alter the resonant frequency by introducing a reactive term.

A number of computer runs have been made with the septum at different positions along the anode, the results being summarised in Table 1.3 and Fig. 15.

Table 1.3 Effect of septum position on the resonant frequency.

Location of the septum	4.6cm	5.6cm	6.6 cm	*7.6 cm	8.6 cm
'cavity' length	14.4cm	13.4 cm	12.4 cm	11.4 cm	10.4 cm
Operation Frequency	1.755 GHz	1.772 GHz	1.806 GHz	1.816 GHz	1.858 GHz

* The original location in TTU experiments

The shift in frequency is as we would expect – a decrease in frequency is associated with an increase in the length of the 'cavity' formed between the cathode base and the septum. This simple test confirms that in the presence of a septum the resonant frequency of the vircator critically depends on its position along the axis of the tube.

Another septum featuring a larger area and a smooth edge, as shown in Fig. 16, has also been examined. A brief comparison of the results is given in Table 1.4.

Table 1.4 Effect of the septum size on the operation of the vircator.

Septum size	Original	Large
Spectrum	1.816 GHz	1.882 GHz
Efficiency	2.05 %	1.54 %

The corresponding frequency spectrum with the new septum in place is shown in Fig. 17; the output is rather disappointing, showing a pronounced peak at 1.667 GHz in addition to the main resonant frequency at 1.882 GHz. Also, the efficiency has fallen from the

usual value of 2.05 % to 1.54 %, probably due to excessive blocking of the RF power

transmitted down the waveguide (impedance mismatch).

1.4 Final Investigations – 3D model

This period covers the last 16 months of our investigations, that is from 1st August 2001 till 30 Nov 2002. We have now reached a stage when our confidence in the reliability of our model was sufficient to attempt an overall simulation of the performance of the TTU vircator

1.4.1 Size and position of circular septum

1.4.1a General comments

During our visit to TTU at the end of April 2002 we have been asked to investigate the effect of a septum in the form of a circular disc with a rectangular cut-out, on the general performance of the vircator. This request was very much in line with our overall desire to bring investigations based on computer modelling and MAGIC as close as possible to the design requirements of the device and thus to achieve the main objective of being able to treat computer modelling as a genuine design tool. This can only be achieved when the code, in our case MAGIC, reaches a sufficient degree of sophistication and reliability to be able to replace machine modelling.

1.4.1b Dimensions and the simulation setup

An axial cross-section of the interaction region of the TTU vircator with the new septum is three different positions are shown in Fig. 18a where the dimensions (in mm) and relative positions of the cathode cylinder, the electron-emitting strip of velvet and the anode 'cage' are clearly indicated. Here the output waveguide is shown on the extreme right, its diameter as usual being the same as that of the anode cage.

The septum, which is in the form of a circular disc with a rectangular cut-out is shown in Fig. 18b. The thickness of the disc and the height of its rectangular cut-out are both fixed, but the width of the cut-out can vary between 10 and 50 mm. The three different positions of the disc relative to the flange are: 0.0 mm (right), 40.6 mm (middle) and 89.5 mm (left). Thus we are going to consider three different positions of the septum and four different widths of the rectangular cut-out, i.e. 3 x 4 = 12 different situations, as shown in Table 1.5

1.4.1c Simulation results

An overview of our simulation results is provided in Table 1.5 where the peak output power and the corresponding frequency of oscillations are shown as functions of the position of the septum and the corresponding width of the rectangular cut-out. In all cases the input power has been kept constant at 26 GW, which corresponds to an input impedance of 16.7 Ω.

Table 1.5 Peak output power and frequency as functions of position of the circular septum and the width of its rectangular cut-out.

	Input Voltage	Input Current	Input Power	Peak Power	Output Frequency
50mm Slot Left	650 kV	39 kA	26 GW	350 MW	2.074 GHz
50mm Slot Right	650 kV	39 kA	26 GW	280 MW	2.171 GHz
50mm Slot Middle	640 kV	40 kA	26 GW	175 MW	2.106 GHz
30mm Slot Left	640 kV	40 kA	26 GW	200 MW	2.074 GHz
30mm Slot Right	650 kV	39 kA	26 GW	150 MW	2.161 GHz
30mm Slot Middle	650 kV	39 kA	26 GW	140 MW	2.051 GHz
20mm Slot Left	640 kV	40 kA	26 GW	140 MW	2.081 GHz
20mm Slot Right	650 kV	39 kA	26 GW	62 MW	2.174 GHz
20mm Slot Middle	650 kV	39 kA	26 GW	80 MW	2.057 GHz
10mm Slot Left	650 kV	39 kA	26 GW	60 MW	2.078 GHz
10mm Slot Right	660 kV	38 kA	26 GW	30 MW	2.168 GHz
10mm Slot Middle	650 kV	39 kA	26 GW	58 MW	2.042 GHz

1.4.1c1 Influence on the output power

We find by varying the width of the rectangular cut-out, Fig. 18b, that the best results are obtained for the biggest size of the slot (50 mm width), when the peak output power is the highest, the opposite being true for the smallest size of the slot (10 mm width). Also we can see from Table 1.5 that placing the disc on the left (i.e. 89.5 mm away from the flange) again yields the best results; the peak output power drops down substantially when the disc is moved near the flange and it drops even further when the disc is placed in its 'middle' position (40.6 mm away from the flange), the three different positions being shown in Fig. 18a.

The first of the two effects is easy to understand, since a small slot prevents the flow of r.f. power towards the output, the disc beginning to act as a metal reflector. The second effect is more difficult to unravel — it is probably closely related to the mode pattern as it gradually develops at the build-up of oscillations; one could also think about it as a form of impedance mismatch.

1.4.1c2 Influence on the frequency of oscillations

Figs. 19a and b respectively show the E-field and its FFT obtained in the usual place i.e. near the end of the output waveguide. Here we have chosen the optimum conditions of a disc with a 50 mm wide slot and in its left position, i.e. 89.5 mm away from the flange, Table 1.5.

At this point it is interesting to compare the different geometries of a septum and the corresponding influence they have on the performance of a vircator. If we look at Figs. 13a, b which refer to the rectangular septum and Figs. 16a, b which represent the circular septum, then it is clear that in both cases the output is much steadier, the corresponding frequency spectrum being much cleaner than that obtained for a vircator without a septum of any form, Figs. 3a, b. However the effect that a septum has on the resonant frequency seems to depend on its geometry. In the case of a rectangular septum, the resonant frequency is shifted down from 2 GHz to 1.82 GHz; at the same time its value strongly depends on the position of the septum along the axis, Table 1.4. In the case of a circular septum the resonant frequency is moved upwards from 2 to 2.07 GHz, its value being only slightly affected by the axial position of the septum or the size of its rectangular slot, the total variation being less than 6 %, as can be seen in Table 1.5.

Finally Figs. 20 and 21 show the actual r.f. output power respectively for a circular and a rectangular septum. We can now see quite clearly that, although in the presence of a circular septum the vircator oscillates more smoothly for some 60 ns, its peak output power is only 350 MW; on the other hand in the presence of a rectangular septum the peak output power reaches 600 MW but only for some 20 ns, the output being somewhat less stable.

Thus with the aid of the cavity-like co-axial geometry of the vircator and by introducing a septum within the anode mesh, one can achieve a reasonably well defined resonant frequency at the output end of the waveguide, as shown in Figs. 13a, b and 16a, b. It would appear that septa have the effect of absorbing stray electrons that hinder clean virtual cathode oscillations. This suggestion is strongly supported by our detailed investigations of electron trajectories described in Section 1.4.2d.

1.4.2 Final model of TTU vircator

1.4.2a Introduction

As we pointed out before the principle of generating microwave radiation using virtual cathode oscillations is conceptually quite simple [1,2,4-6,9-15], however the actual process is highly non-linear; it is therefore singularly difficult to treat it analytically. It seems that computer modeling presents the only viable method for the study and understanding of the vircator interaction process. We have therefore decided to concentrate in this section on modelling in some detail the cathode/anode area where the main interaction process is taking place. We are fully aware of the fact that in the past [1,4,9-14] some efforts have been made to simplify matters by assuming that in principle there are two types of interaction going on at the same time. An oscillation due to

forward and backward movement of electrons between real and virtual cathodes, the semi-permeable anode being situated in-between and a sort of 'plasma-frequency' oscillation due to the movement of the virtual cathode itself, mostly in the form of space-charge density fluctuation around its theoretical saturation point. The two corresponding frequencies, usually referred to as f_{reflex} and f_p, invariably differ by a large factor and any attempts to use either as an expected vircator frequency of oscillations have not been very successful. The best one could say is that the actual frequency of oscillations occurs in the following range [1,4,10]

$$2.2 f_p < f_{osc} < 2.7 f_p \qquad (1.1)$$

We will see more clearly later on some reasons for the above discrepancy.

A close observation of the interaction process as displayed by the computer model revealed that, as perhaps we should have expected, the movement of electrons is much more complex than it was generally assumed. Certainly in the case of a coaxial vircator there is a strong whirl-like motion around the metal ring situated at the end of the anode cage, Figs. 27a-f. This motion clearly affects the frequency at which the virtual cathode oscillates around its saturation point. In addition we have a marked axial component of current, both inside and outside of the anode cage. In fact the electrons forming the space charge appear to be divided into three groups:

- those intermittently forming a virtual cathode on the inside of the anode,
- those in axial circular motion hugging the anode or whirling around the support ring and

28

- the 'rogue' or stray electrons which move towards the output waveguide and thus remove energy from the interaction mechanism and lower electronic efficiency of the power conversion process.

Having obtained some insight into the complexity of the interaction process we were then able to improve the efficiency of the device by trying to get rid of the rogue electrons. As explained in Section 1.3.3d this was achieved by altering the design of the anode and introducing a carefully shaped septum placed inside the anode, Figs. 28a and b. The septum succeeds in trapping the stray electrons which intern increases the microwave power output by some 52 %.

1.4.2b Input and output pulses

As a first step in our simulation process we have decided to repeat the results shown in Figs. 22 and 23. Introducing absorbing boundaries at both ends of our model and applying 500 kV pulse of 70 ns duration, we have obtained simulated input voltage and current as functions of time, as shown in Fig. 24. The peak values of 730 kV and 38.4 kA are within 1 – 5 % of the measured values shown in Fig. 22. The contour of the measured pulse is much more rugged than that obtain by simulation, but this tends to be true of many simulation processes, the rugged shape being influenced by local construction details not included in the model (e.g. the thin rods supporting the anode). Again dividing peak voltage by peak current we obtain 19.0 Ω, which is within 5 % of the measured value.

Let us now consider the simulated input and microwave output power, as shown in Fig. 25; we find that their respective peak values are 25.8 GW and 600 MW, Poynting's

theorem being used to obtain the simulated output microwave power. The computed peak values are again within 5-8 % of the measured values shown in Fig. 23. Both sets of results show two distinct peaks in the microwave output power; this could well be due to some impedance mismatch in the dynamics of virtual cathode oscillations. Also the range of small fluctuations in the computed output is typical of mode overlap in the heavily overmoded output waveguide. We find from Fig. 23 by dividing peak output by peak input power that the electronic efficiency of the tube is of the order of 2.3 %, which is usual for vircators. The corresponding simulation value obtained from Fig. 25 is also 2.3 % in close agreement with the measured value. This further supports our confidence in the adequacy of our modelling process.

Finally we note that there is a natural time delay between the input pulse measured near the cathode/anode space and the output power measured near the end of the waveguide, Figs. 23 and 25. In the computer model shown in Fig. 25, the delay is approx. 13 ns and it can be accounted for by the time it takes the pulse to travel down the system. (Analytical expressions for the time of travel cannot be easily obtained because the output waveguide is heavily overmoded). The measured delay, Fig. 23, is somewhat longer and of the order of 20 ns, probably due to a slower build up of oscillations than predicted by the model.

1.4.2c Frequency spectrum

The simulated frequency spectrum is shown in Fig. 26. It was obtained by applying FFT to the output from an E-field probe situated near the window of the output waveguide. We find that the main resonant frequency occurs at 2.108 GHz, which compares favourably with the measured value of 2.00 GHz (this is a different resonant frequency

30

than that quoted in Fig. 10b, the difference being due to more recent TTU structural adjustments concerning the cathode/anode gap, which we included in our model). The frequency spectrum is still fairly broad-band, in spite of the presence of a rectangular septum, Figs. 6 and 7a, b – this situation is typical of vircators. Without a septum the frequency spectrum is quite chaotic, as shown in Fig. 3b.

1.4.2d Electron trajectories

In order to consider the interaction process in detail it has been decided to create a movie which would simultaneously trace the movement of some 10, 000 electrons as they are emitted by the cathode, approach or pass the foil anode and then form a virtual cathode. The MAGIC code we have used is ideally suited for this kind of investigation. We then discovered that instead of reflexing radially between real and virtual cathodes, as postulated by some, the movement of the electrons is much more complicated. First of all there is a short period lasting some 6 ns, when the electron cloud is being set up, the electron cloud remaining relatively uniform, as shown in Fig. 27a. We then find that the electrons split into three distinct groups. The first group does indeed pass through the semipermeable anode and forms a virtual cathode which then saturates, sending electrons back towards the cathode, the repetition of this process giving rise to the usual form of relaxation oscillations. However not all electrons take part in this process. A second group of electrons fails to contribute to the virtual cathode and either travels in the axial direction close to the anode, Fig. 27b or even wraps itself in tight circles round the anode ring, Fig. 27c. Finally there is a third group of electrons, called 'stray' or 'rogue' electrons, which detach themselves from the cloud and travel in bunches down the system, finally landing either on the anode near the flange or even on the walls of the waveguide, Figs. 27d. All this can be seen very clearly in the 'movie' obtained by observing Figs. 27b-f in

quick succession on the screen. The stray electrons detract from the proper interaction process and should be eliminated if at all possible. Figs. 27b-f show a complete cycle of the interaction process which lasts for $T = 0.52$ ns, which corresponds to the $f = 1/T = 1.923$ GHz and is within 9 % of the oscillation frequency f=2.108 GHz, Fig. 26. The exact value should have been $T = 0.47$ ns, but it was difficult to freeze the 'frame' which would correspond more closely to the end of one cycle of oscillations.

1.4.2e Suggestion for an improved design

Having unravelled with the help of Figs. 27a-f some of the intricacies of the cylindrical vircator interaction process, we have decided to investigate the possibility of improving the performance of the tube. An obvious target was to get rid of the so-called stray electrons mentioned in the previous section. About eight or ten septa of varying geometry have been investigated, until finally the design shown in Figs. 28a and b proved to be the best. In addition it was necessary to replace the semipermeable mesh by solid metal over one half of its length near the flange, as shown in Fig. 28a. All these changes required many additional computations, each run lasting for some 12 – 16 hours.

The input and output power pulses are shown in Fig. 29. The model shows that for the same peak input power of 25.9 GW, the peak output power has grown from 600 to 913 MW, an increase of 52 %. At the same time the electronic efficiency calculated as the ratio of peak output to peak input power has grown from 2.3 % to 3.5 %, which is quite a welcome improvement.

Finally the FFT of the output from an E-field probe situated near the end of the waveguide is shown in Fig. 30. Comparing Figs. 30 and 26 we find that the main

resonance frequency has shifted upwards from 2.108 to 2.153 GHz, the whole spectrum being similar to that shown in Fig. 26. The shift in frequency was to be expected since it has been noted before that the main resonant frequency is very sensitive to the thickness of the anode ring and the length of the permeable section of the anode. As far as the 'cleaning up' of the spectrum is concerned we noted on several occasions that septa have that effect, presumably by acting somewhat like a quasi-cavity. Here one has to strike balance between this effect and a drop in power caused by the septum acting as an obstruction to the flow of power.

Conclusions – part 1.

Two main conclusions can be drawn from the above investigations. In the first place we have established that computer modelling of vircators has reached a degree of sophistication consistent with its use as a design tool. Secondly we were able to show that the interaction process between the beam and the e.m. field is not only highly nonlinear but also very complex, so that an analytical approach would be fraught with difficulties, computer modelling being the only practical solution. Finally having investigated the interaction process in some detail we have been able to suggest changes in design which should increase the microwave power output by some 52%.

References – part 1

1. W. Jiang, K. Woolverton, J. Dickens, M. Kristiansen, High-power microwave generation by a coaxial virtual cathode oscillator, IEEE Trans. Plasma Science, vol. 27, 1999, pp. 1538-1542.

2. W. Jiang, J. Dickens and M. Kristiansen, Efficiency enhancement of a coaxial virtual cathode oscillator, IEEE Trans, Plasma Science, vol. 27, 1999. 1543-1544.

3. B. Goplen, L. Ludeking, D. Smithe, and G. Warren, User-configurable MAGIC for electromagnetic PIC calculations, Computer Physics Communication, vol. 87, 1995, pp.54-86.

4. V. L. Granatstein and I. Alexeff, *High-Power Microwave Sources*, Boston, MA: Artech House, 1987, ch. 13, 14.

5. J. Benford and J. Swegel, *High-Power Microwaves*, Boston, Artech House, 1992, ch. 9.

6. R. J. Barker and E. Schamiloglu, *High-Power Micowave Sources and Technologies*, IEEE Press Series on RF and Microwave Technology, 2001, ch. 2.

7. C. K. Birdsall, *Electron Dynamics of Diode Regions*, Academic Press, New York, 1966, ch. 3.

8. H. R. Jory and A.W. Trivelpiece, Exact relativistic solution for the one-dimensional diode, J. Appl. Phys., vol. 40, 1969, pp. 3924-3926.

9. R. A. Mahaffey, P. Sprangle, J. Golden, and C. A. Kapetanakos, High-Power Microwaves from a Nonisochronic Reflecting Electron System, Phys. Rev. Lett. vol. 39, 1977, pp. 843-846.

10. D. J. Sullivan, High power microwave generation from a virtual cathode oscillator (vircator), IEEE Trans. Nuclear Science, vol. NS-30, 1983, pp. 3426-3428.

11. H. A. Davis, R. R. Bartsch, T. J. T. Kwan, E. G. Sherwood and R. M. String field, Experimental confirmation of the reditron concept, IEEE Trans, Plasma Science, vol. 16, 1988, pp. 192-198.

12. C. S. Hwang, M. W. Wu, P. S. Song and W. S. Hou, High power microwave generation from a tunable radially extracted vircator, J. Appl. Phys. vol 69, 1991, pp. 1247-1252.

13. B. V. Alyokhin, A. E. Dubinor, V. D. Selemir, O. A. Shamro, K. V. Shibalko, N. V. Stepauov and V. E. Vatrunin, Theoretical and experimental studies of virtual cathode microwave devices, IEEE Trans. Plasma Science, vol. 22, 1994, pp. 945-959.

14. W. Jiang, K. Masugata, and K. Yatsui, Mechanism of Microwave Generation by Virtual Cathode Oscillation, Phys. Plasma, vol. 2, 1995, pp. 982-986.

15. E. H. Choi, M. C. Choi, Y. Jung, M. W. Chong, J. J. Ko and Y. Seo, High-power microwave generation from an axially extracted virtual cathode oscillator, IEEE Trans. Plasma Science, vol. 28, 2000, pp.

16. S. A. Kitsanov, A. I. Klimov, S. D. Korovin, I. K. Kurkan, I. V. Pegel and S. D. Polevin, A vircator with electron beam premodulation based on high-current repetitively pulsed accelerator, IEEE Trans. Plasma Science vol. 30, 2002, pp. 274-285.

17. A. G. Zherlitsyn, Microwave generation in a coaxial triode with virtual cathode, Sov. Tech. Phys. Lett, vol 6, 1990, pp. 879-880.

18. P. A. Lindsay, X. Chen, J. Watkins and W. K. Toh, Computer modelling of cirtual cathode oscillators (Vircators); Grant No: F49620-00-1-0157, Progress Report 15 Jan – 31 July 2000.

19. W. K. Toh, X. Chen, J. Watkins, P. A. Lindsay, K. Woolverton and M. Kristiansen, Computer modelling of a coaxial vircator, IEEE PPPS01 Conference in Las Vegas; Conference Proceedings p. 503 (poster presentation).
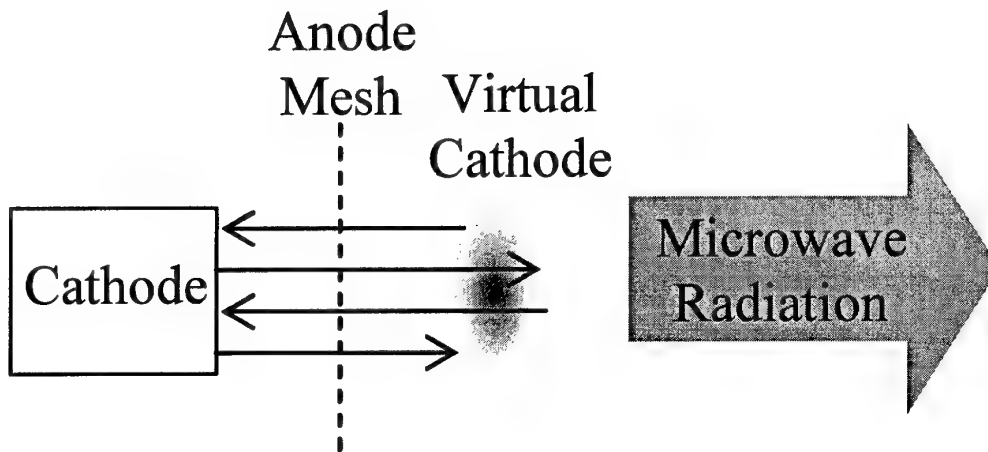
Figures – part 1

Figure 1 Schematic diagram of a plane vircator.

Figure 2 Cross-section of an early model of the TTU vircator.

Figure 3a E_ρ field intensity as recorded near the output window.

Figure 3b Frequency spectrum of the microwave output (FFT of Fig. 3a) – main resonant peak at 2.73 GHz.

Figure 4 Snapshot of E_ρ contours near the output window.

Figure 5 Snapshot of B_ρ contours near the output window.

Figure 6 Gun Section of the TTU vircator.

Figure 7a Axial cross-section of the improved TTU vircator model.

Figure 7b Transverse view of the rectangular septum situated in plane A-A' of Fig. 6a.

Figure 8a Rectangular septum and part of the anode in Cartesian co-ordinates.

Figure 8b Rectangular septum and part of the anode in polar co-ordinates.

Figure 9 Various ways of applying the anode voltage.

Figure 10a Typical vircator output – TTU E-field probe measurements.

Figure 10b Frequency spectrum – fast Fourier transform (FFT) of Fig. 10a – main resonant peak at 1.834 GHz.

Figure 11 Simulated input power pulse.

Figure 12 Simulated microwave output power pulse.

Figure 13a Simulated E-probe output.

Figure 13b FFT of Fig. 13a – peak resonant frequency at 1.816 GHz.

Figure 14 Resonant frequency as a function of cathode/anode gap.

Figure 15 Peak resonant frequency as a function of axial position of the rectangular septum, Fig. 8b.

Figure 16 Enlarged smooth edge septum.

Figure 17 Frequency spectrum with enlarged, smooth-edge septum in place.

Figure 18a Axial Cross Section of the interaction region.

Figure 18b Septum in the form of a circular disc with a rectangular cut-out.

Figure 19a E-field output in the presence of a circular septum ('left'position, slot 50mm wide)

Figure 19b FFT plot of Fig. 19a; main resonance now at 2.074 GHz.

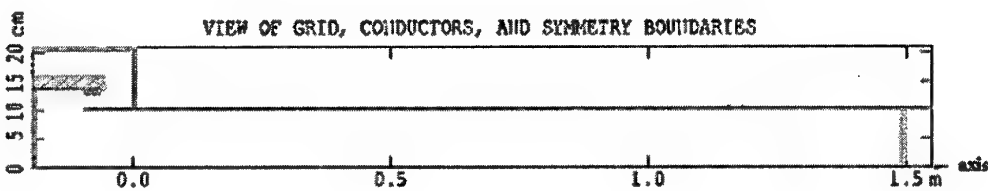*Figure 1 Schematic diagram of a plane vircator.*

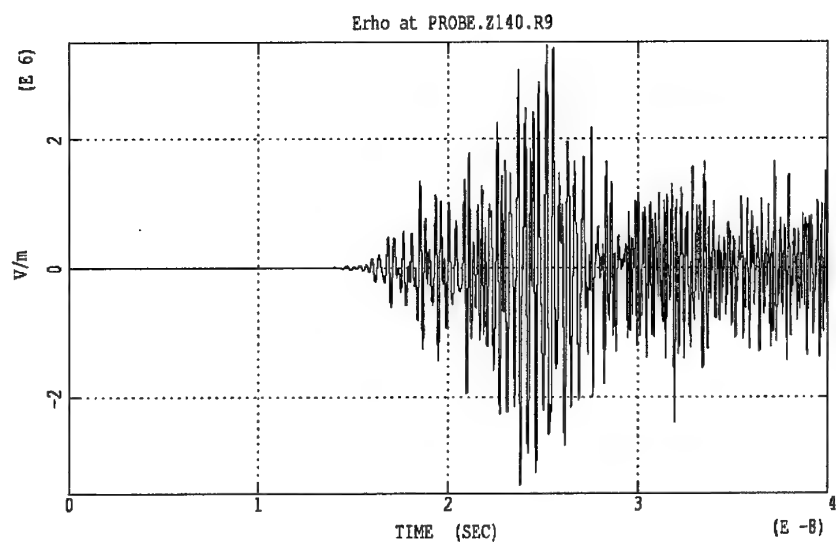*Figure 2 Cross-section of an early model of the TTU vircator.*

Figure 3a E_ρ *field intensity as recorded near the output window.*

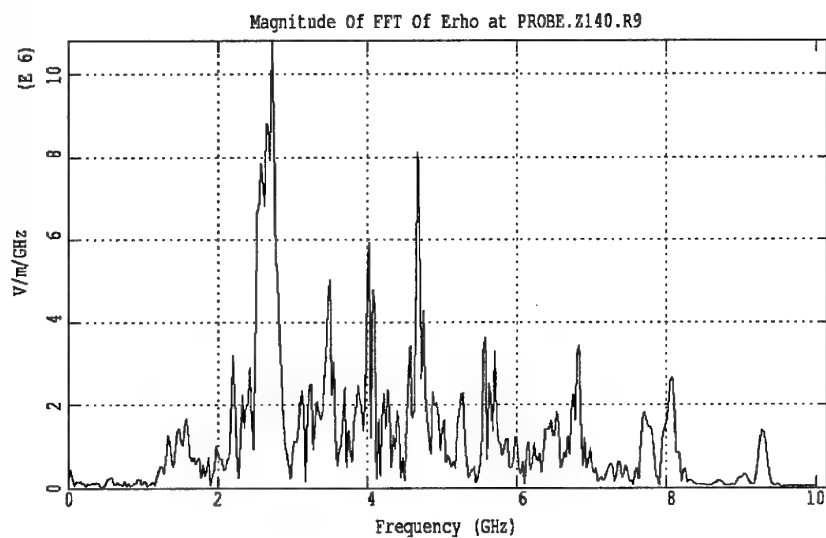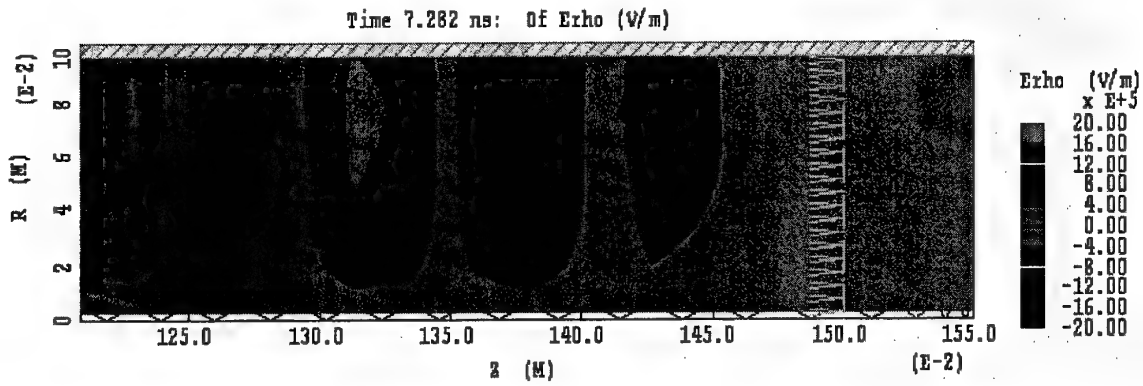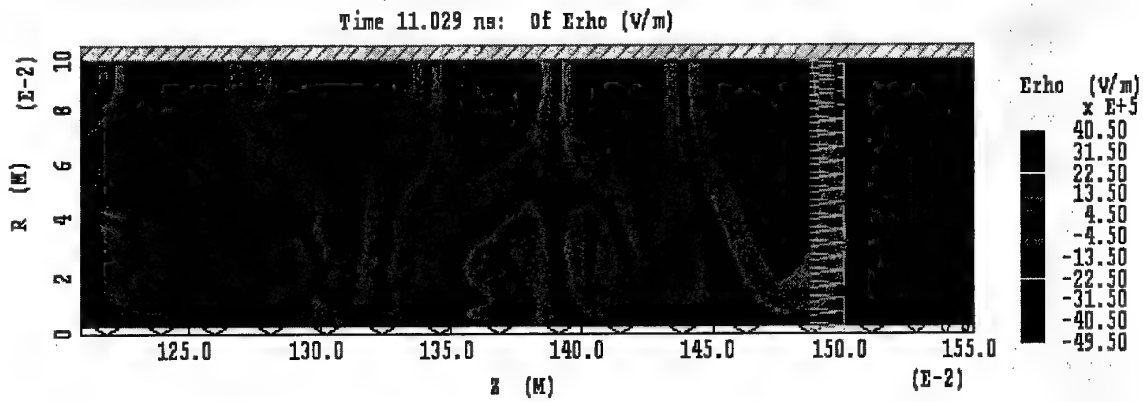*Figure 3b Frequency spectrum of the microwave output (FFT of Fig. 3a) – main resonant peak at 2.73 GHz.*

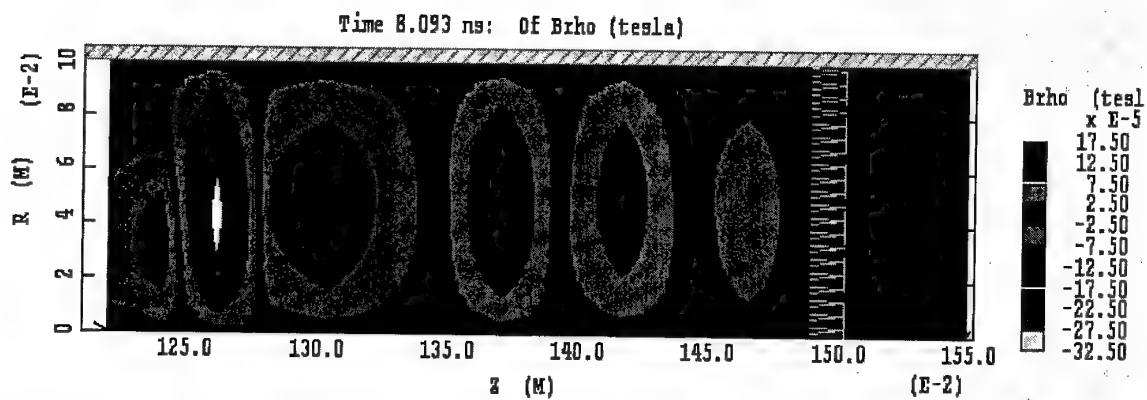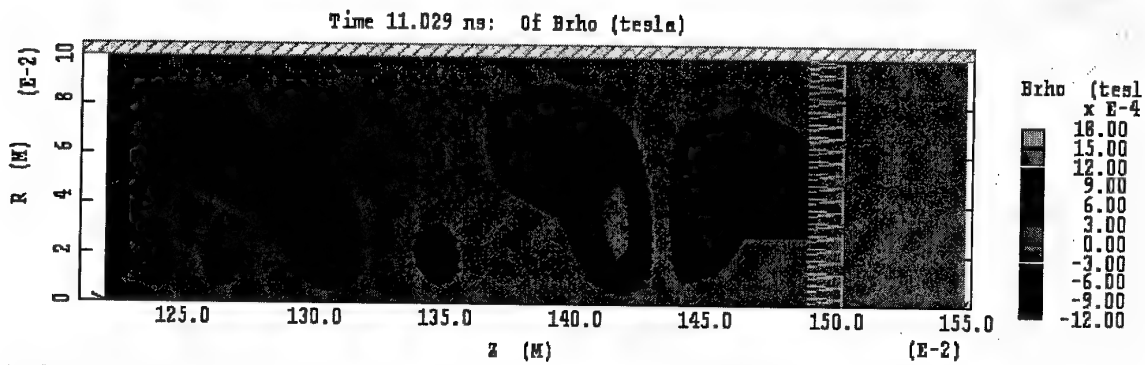*(a) early stage of oscillations, t=7.282 ns.*

(b) advanced stage of oscillations, t=11.029 ns.

Figure 4 Snapshot of E_ρ contours near the output window.

41

Time 8.093 ns: Of Brho (tesla)

(a) *early stage of oscillations, t=8.093 ns*

Time 11.029 ns: Of Brho (tesla)

(b) *advanced stage of oscillations*

Figure 5 Snapshot of B_ρ contours near the output window.

42

Cathode Base — **Velvet Emitter** — **Output Waveguide** — **Stainless Steel Mesh Screen (Anode)** — **Septum** — **Side View** — **End View**

Figure 6 Gun Section of the TTU vircator.

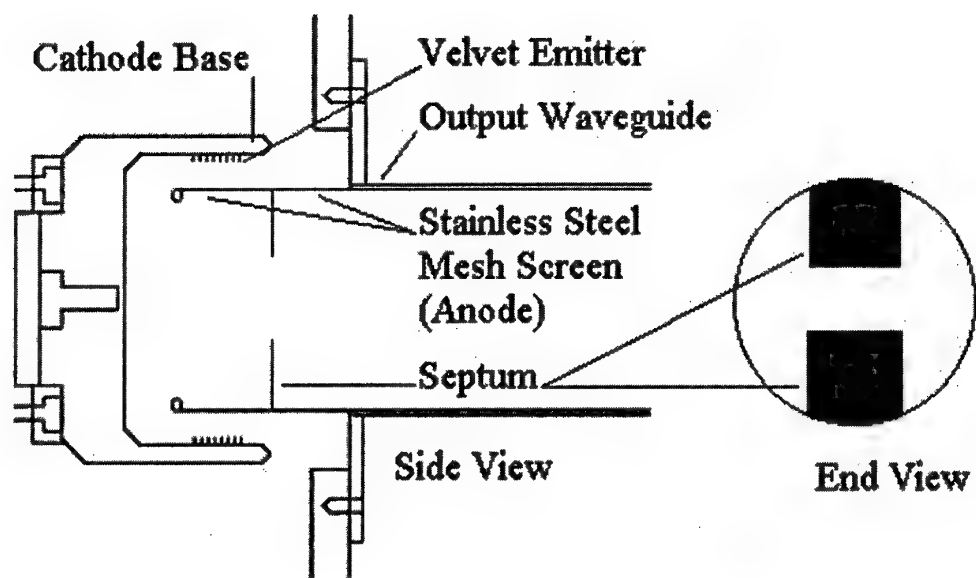A — Anode mesh — Circular waveguide — Input pulsed power — Flange — Output microwave power — Anode ring — Rectangular Septum
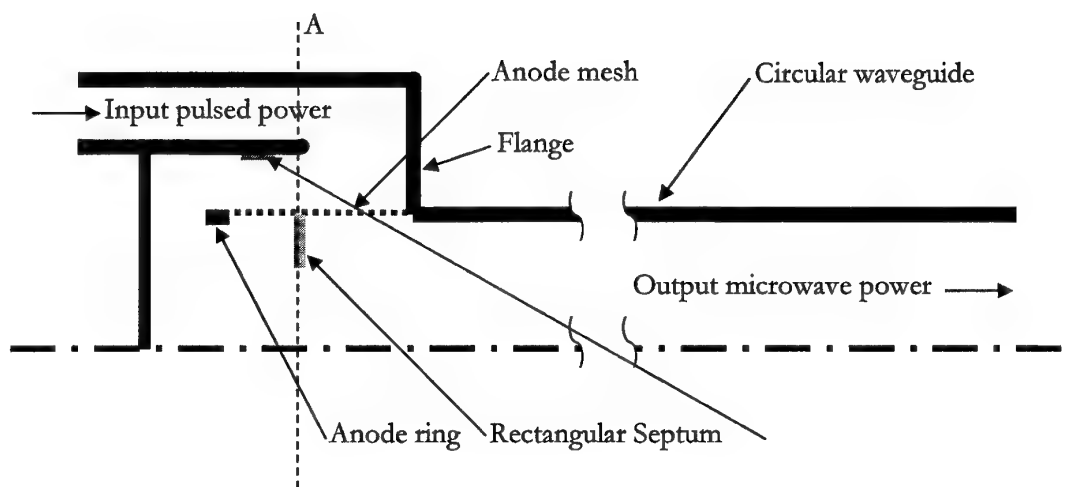
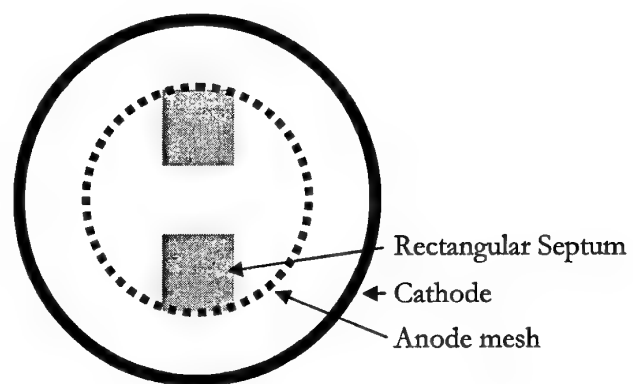*Figure 7a Axial cross-section of the improved TTU vircator model.*

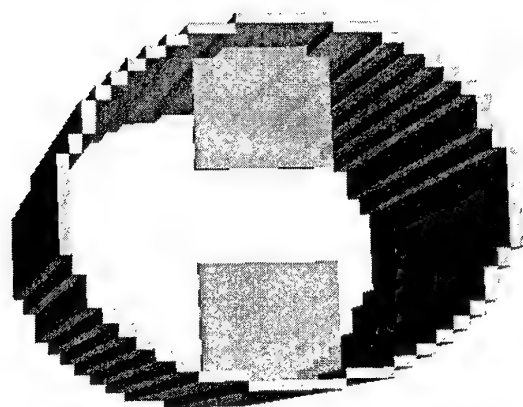*Figure 7b Transverse view of the rectangular septum situated in plane A-A' of Fig. 6a.*

Figure 8a Rectangular septum and part of the anode in Cartesian co-ordinates.
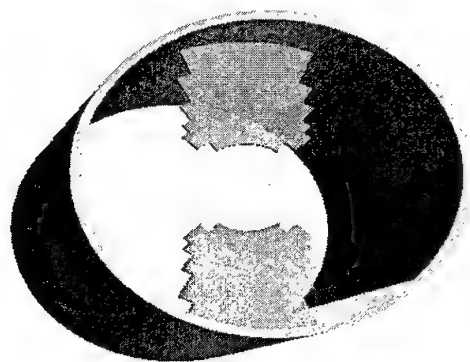

Figure 8b Rectangular septum and part of the anode in polar co-ordinates.

45

(a)

(b)

(c)

(d)

Figure 9 *Various ways of applying the anode voltage.*

Figure 10a Typical vircator output – TTU E-field probe measurements.

Figure 10b Frequency spectrum – fast Fourier transform (FFT) of Fig. 10a – main resonant peak at
*   1.834 GHz.*

FIELD_POWER S.DA at AKFEED

Figure 11 Simulated input power pulse.

FIELD_POWER S.DA at EXIT_WAVE

Figure 12 Simulated microwave output power pulse.

FIELD Erho at R0.P90.Z1500

Figure 13a Simulated E-probe output.

FIELD Magnitude Of FFT Of Erho at R0.P90.Z1500

Figure 13b FFT of Fig. 13a – peak resonant frequency at 1.816 GHz.

49

Figure 14 Resonant frequency as a function of cathode/anode gap.

Figure 15 Peak resonant frequency as a function of axial position of the rectangular septum, Fig. 8b.

⊕ Standard TTU septum position.

Computer grid of area septum

Figure 16 Enlarged smooth edge septum.
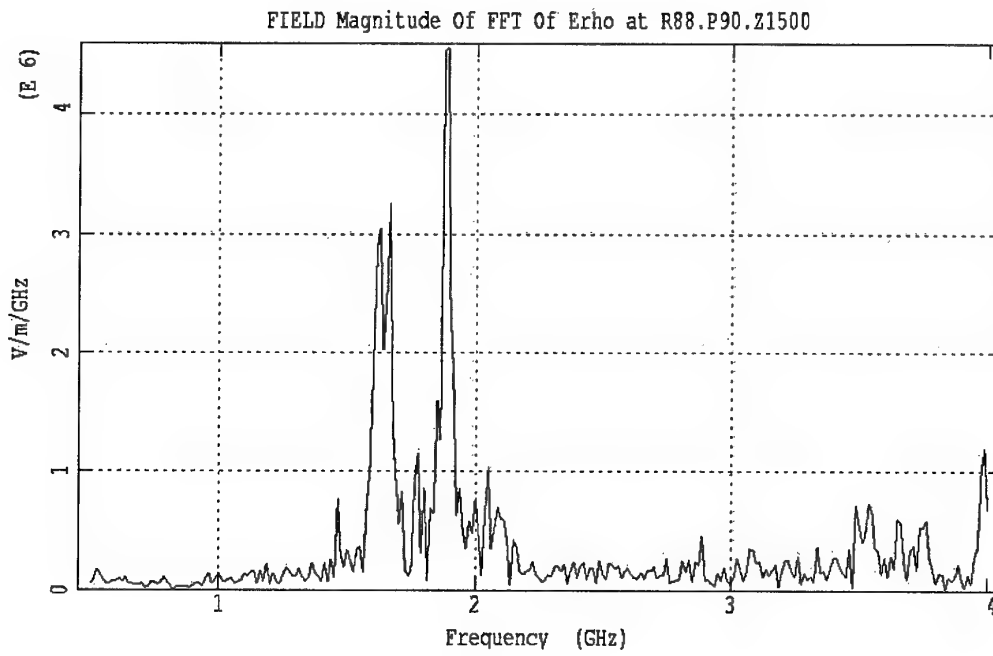
FIELD Magnitude Of FFT Of Erho at R88.P90.Z1500

Figure 17 *Frequency spectrum with enlarged, smooth-edge septum in place.*

Figure 18a Axial Cross Section of the interaction region.

Figure 18b Septum in the form of a circular disc with a rectangular cut-out.

FIELD Erho at R88.P90.Z1500

Figure 19a E-field output in the presence of a circular septum ('left' position, slot 50mm wide)

FIELD Magnitude Of FFT Of Erho at R88.P90.Z1500

Figure 19b FFT plot of Fig. 19a; main resonance now at 2.074 GHz.

56

FIELD_POWER S.DA at OUT.RIGHT.IN
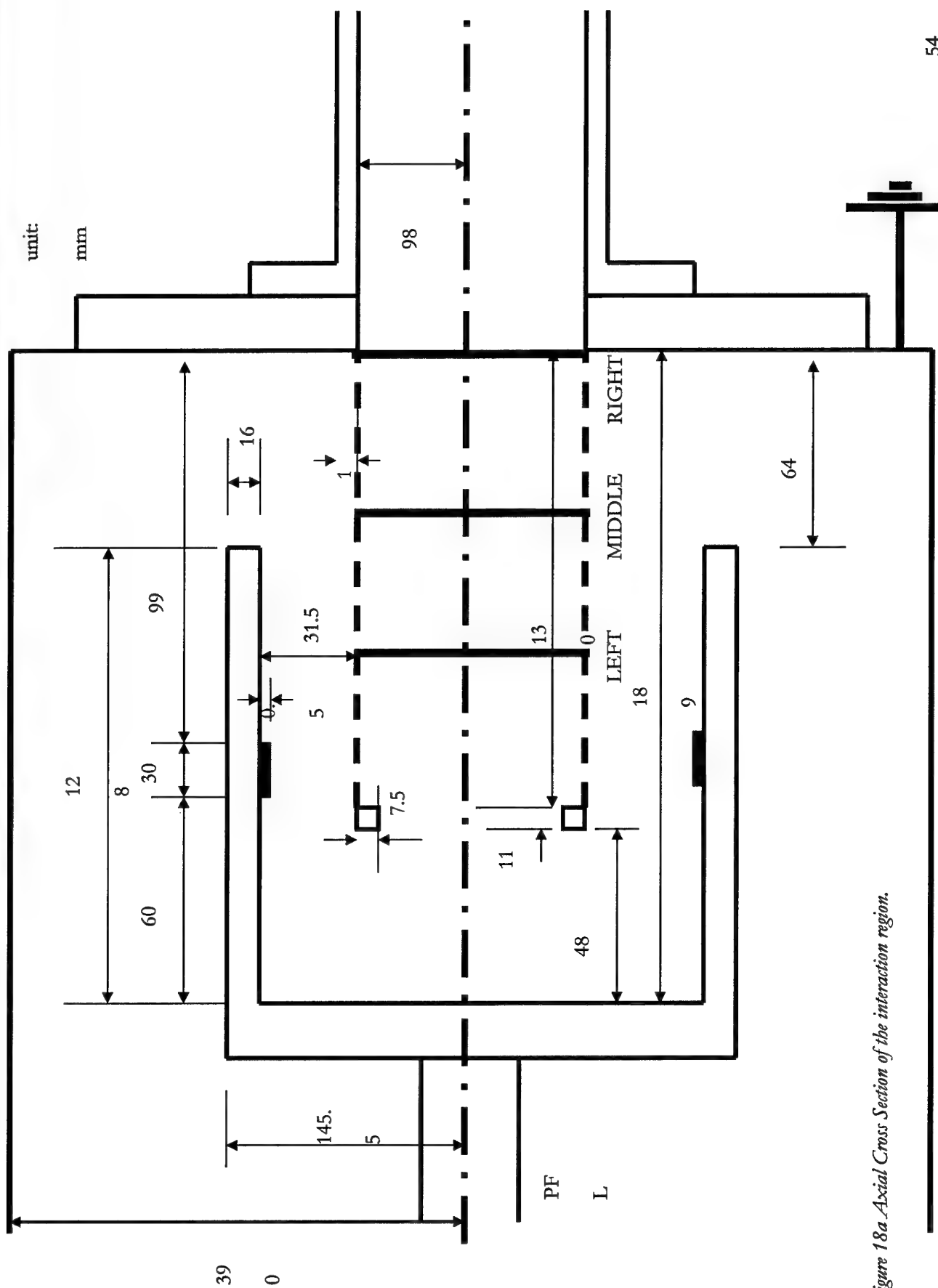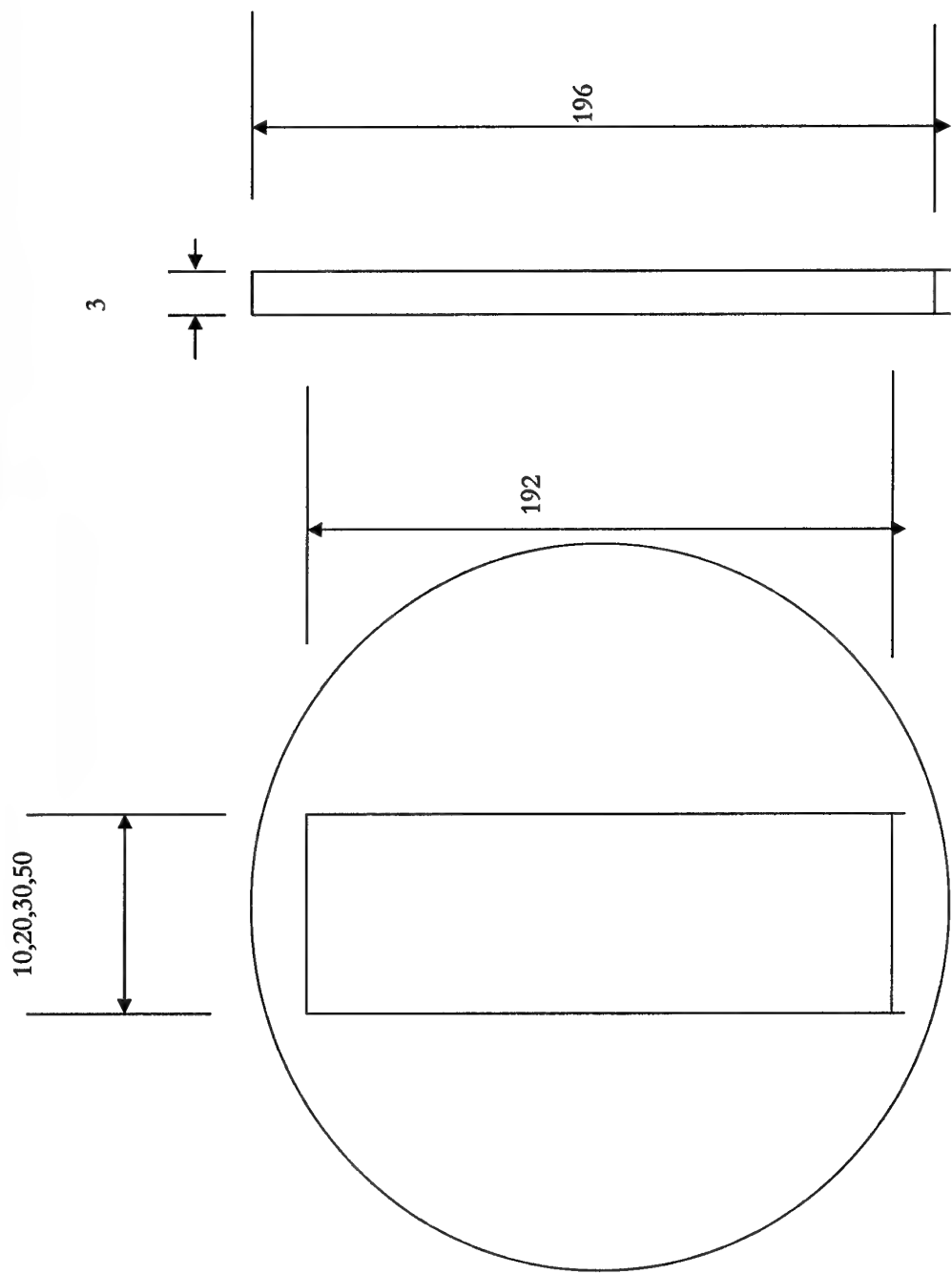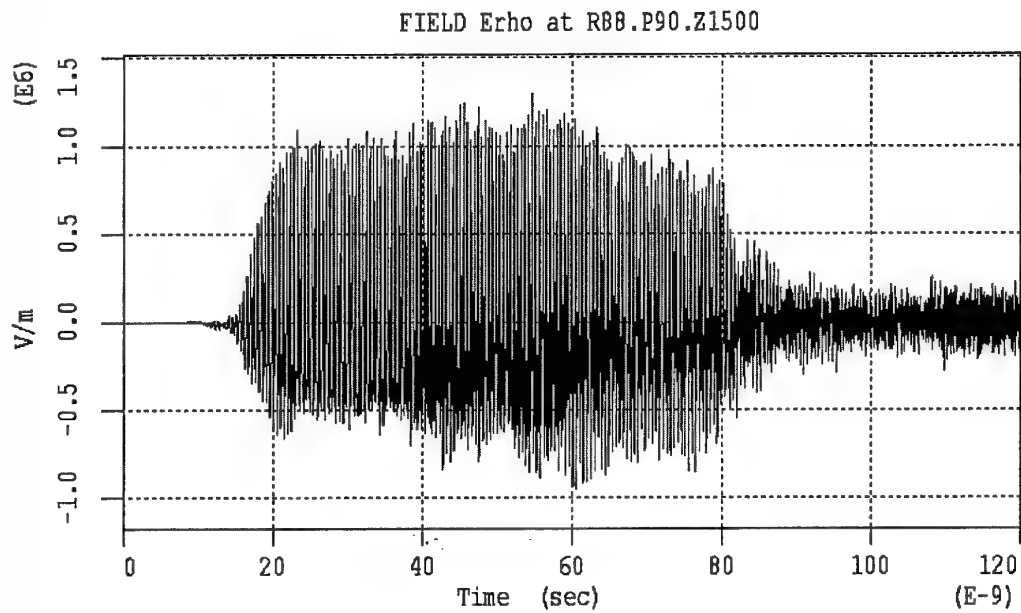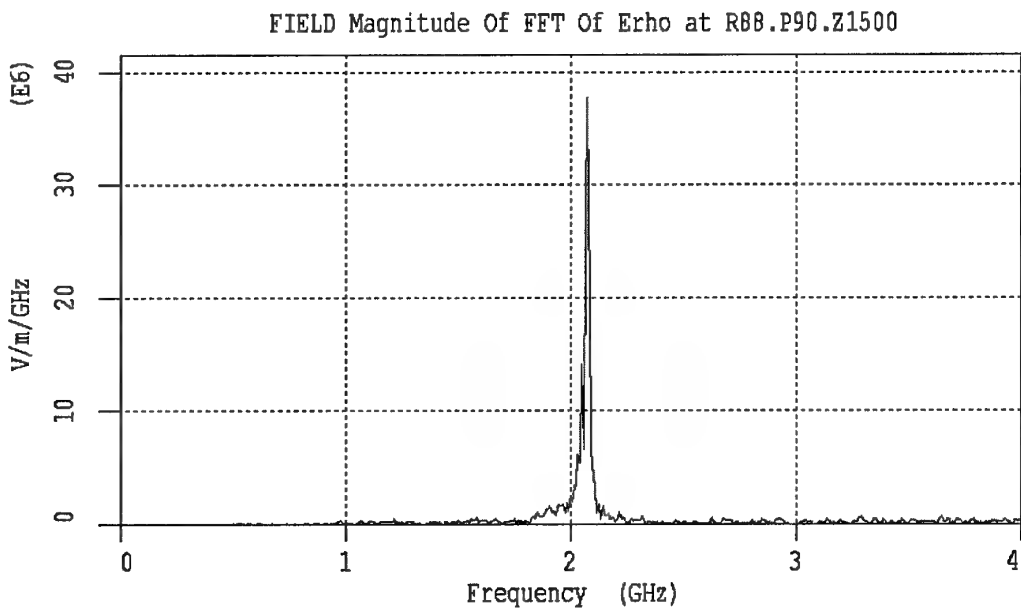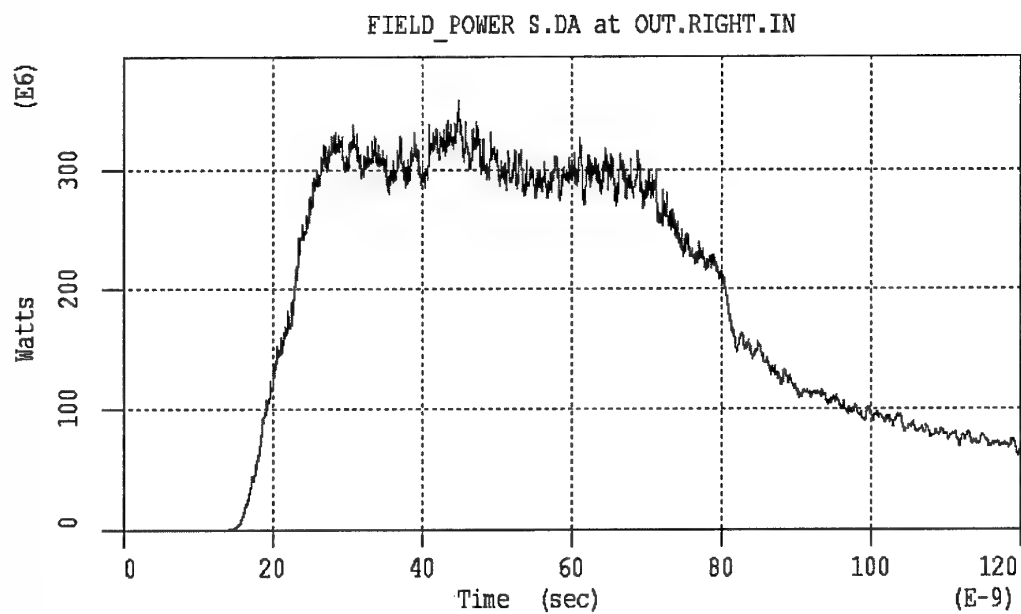
Figure 20 Output power pulse in the presence of a circular septum ('left' position, slot 50mm wide)

FIELD_POWER S.DA at OUT.RIGHT.IN
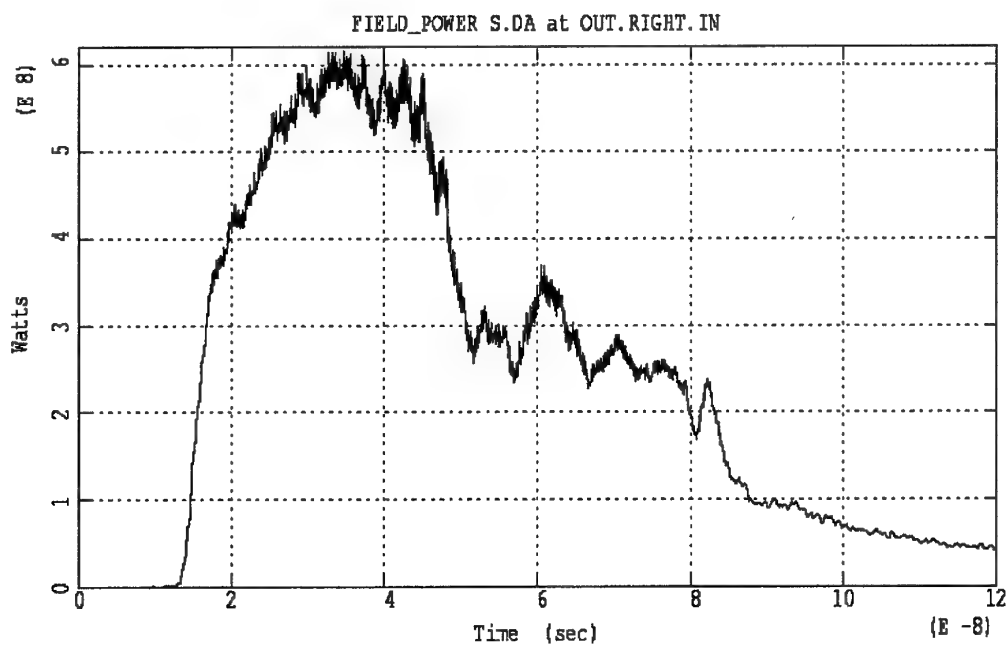
Figure 21 Output power pulse in the presence of a rectangular septum.

57
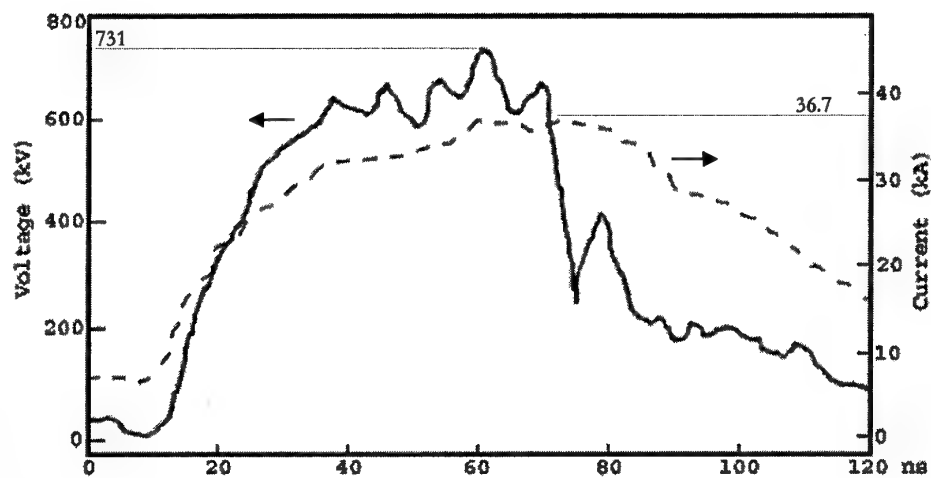
Figure 22 Typical TTU input voltage and current pulses.
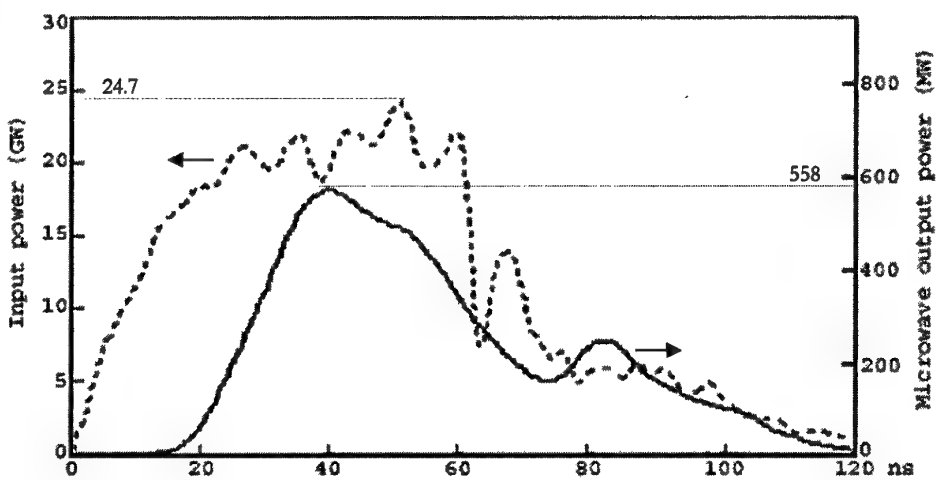
Figure 23 Typical TTU input power and microwave output power pulses.
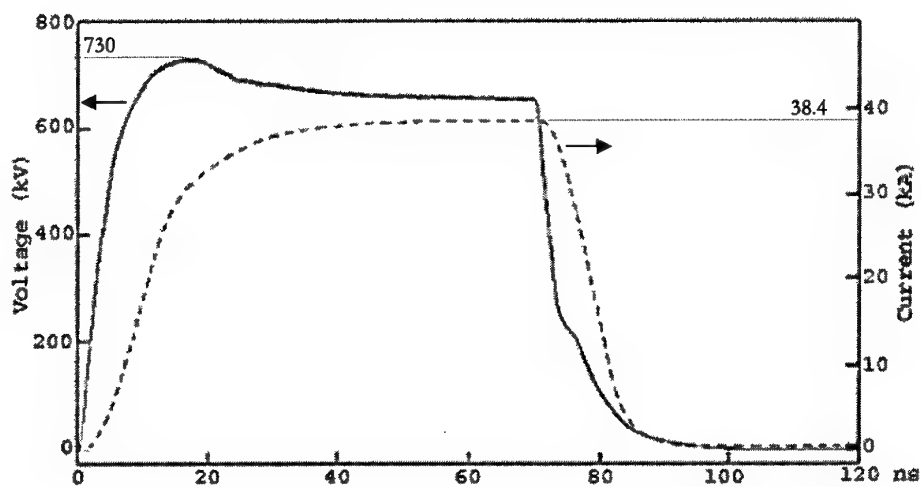
Figure 24 Simulation input voltage and current pulses.
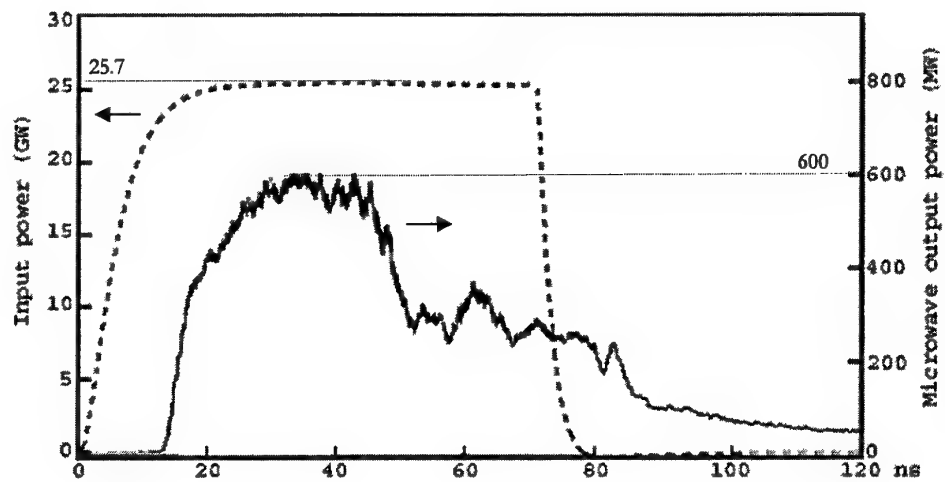
Figure 25 Simulation input and microwave output power pulses.

59
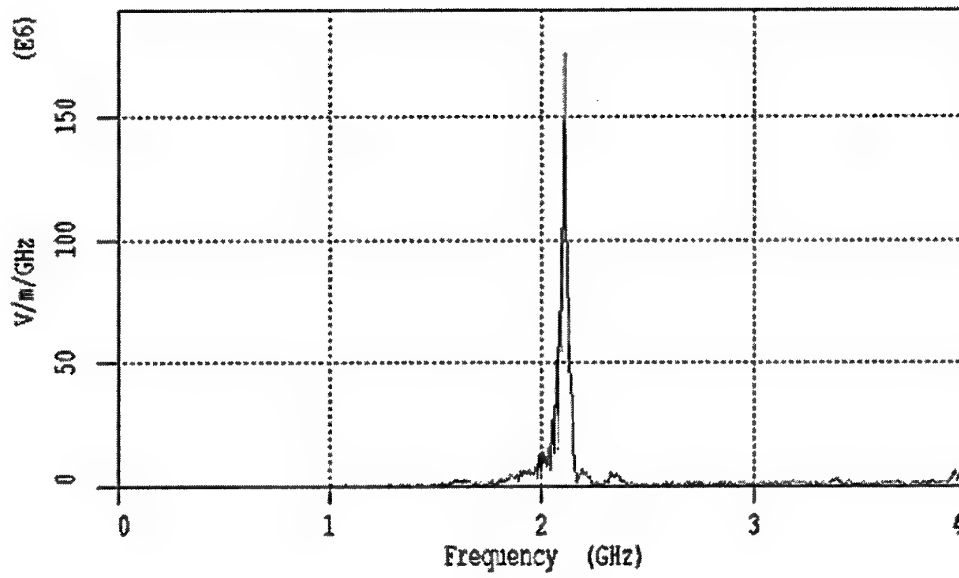
Figure 26 Simulated frequency spectrum – main resonant frequency at 2.108 GHz.
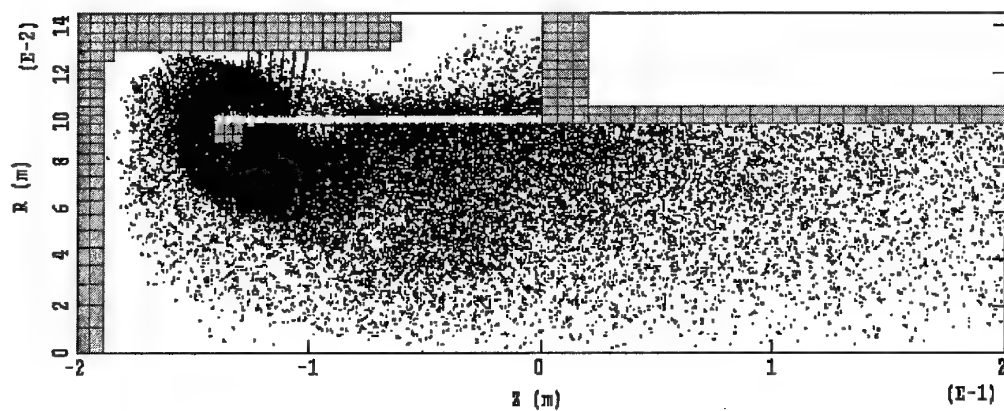
Figure 27a Electron cloud prior to the start of oscillations, t = 6.60 ns.
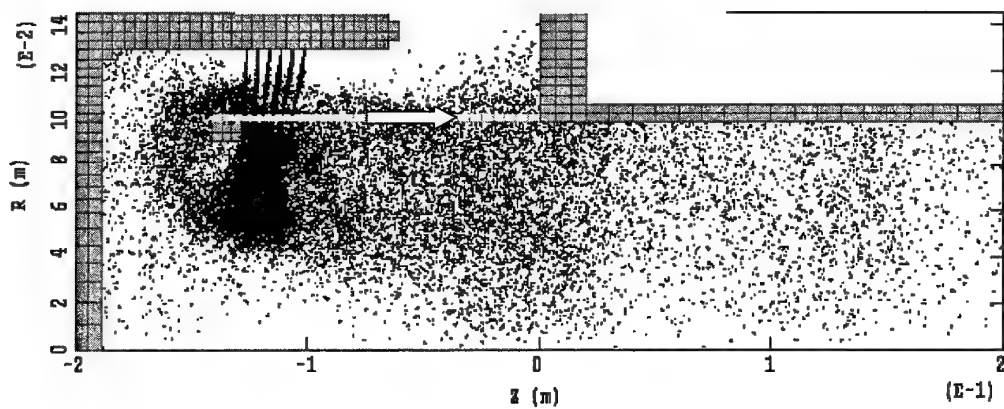
Figure 27b Electron cloud at t = 20.00 ns; arrow indicating the electrons lingering near the anode foil and drifting towards the flange.

61
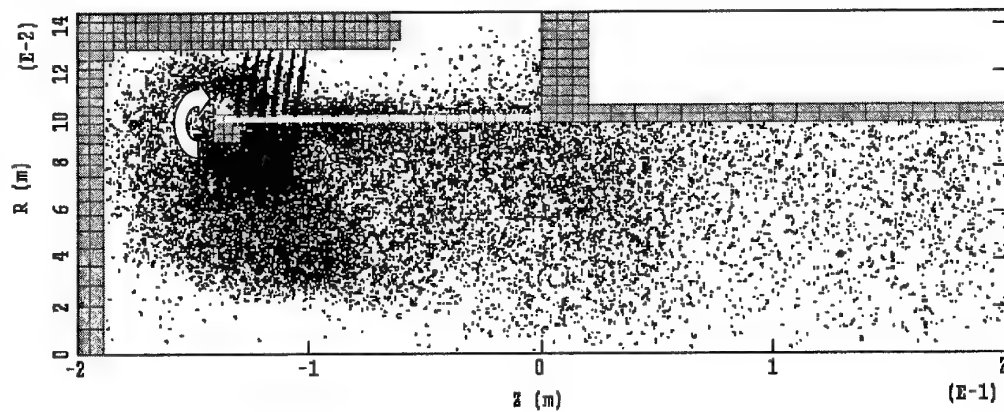
Figure 27c Electron cloud at t = 20.12 ns; arrow indicating electrons curling around the anode supporting ring.
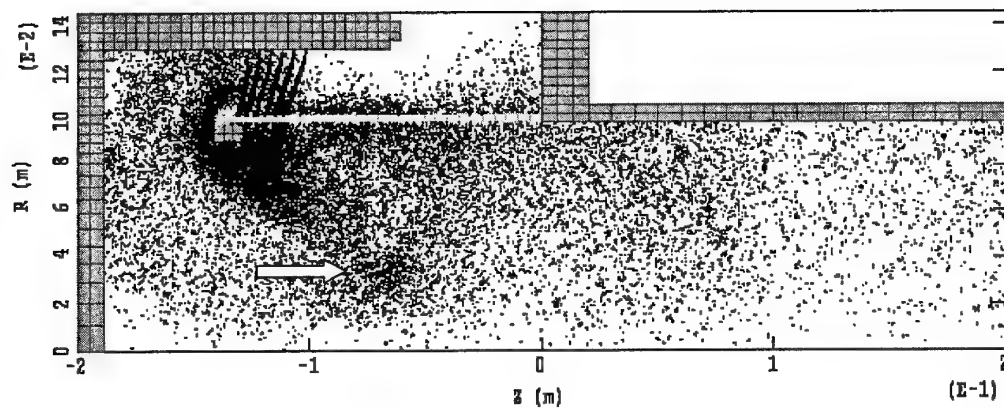
Figure 27d Electron cloud at t = 20.24 ns; arrow indicating electrons moving in bunches towards the waveguide.
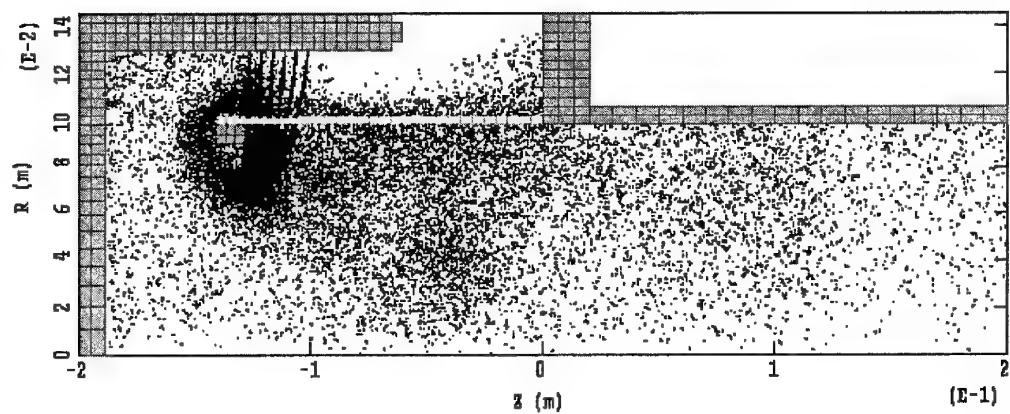
Figure 27e Electron cloud at t = 20.36 ns.
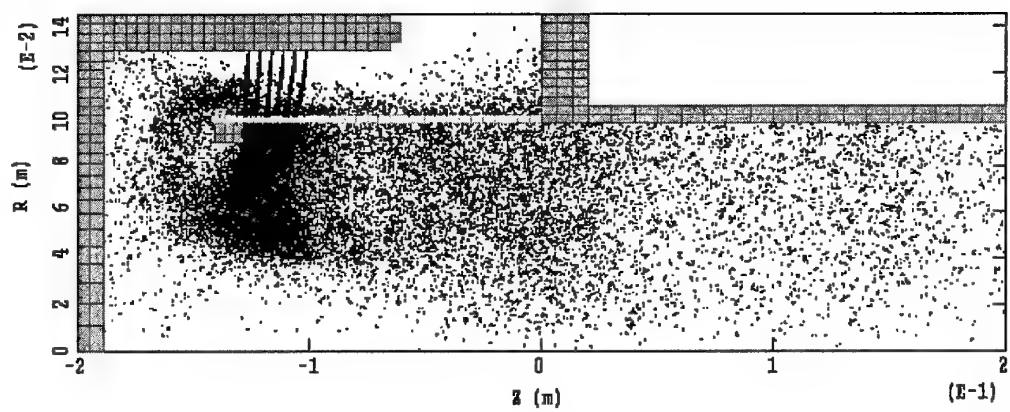
Figure 27f Electron cloud at the end of one cycle of oscillations, t = 20.52 ns.

63
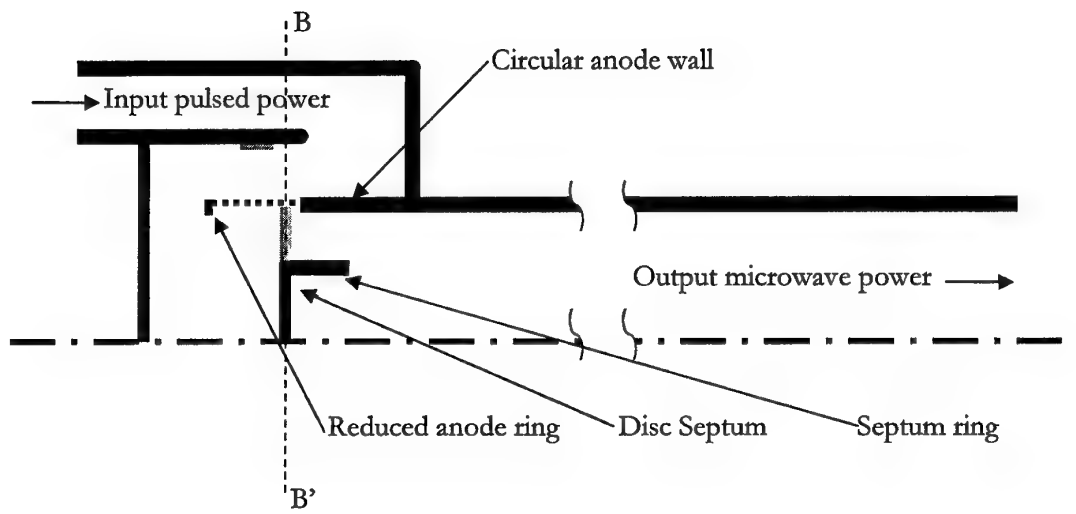
Figure 28a Cross-section of the vircator-improved design.
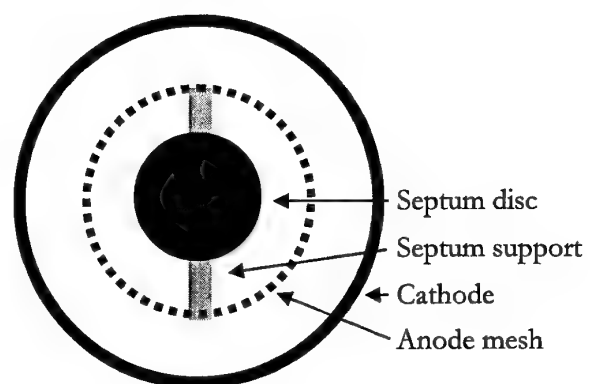
Figure 28b New septum design; plane B-B' of Fig. 28a.
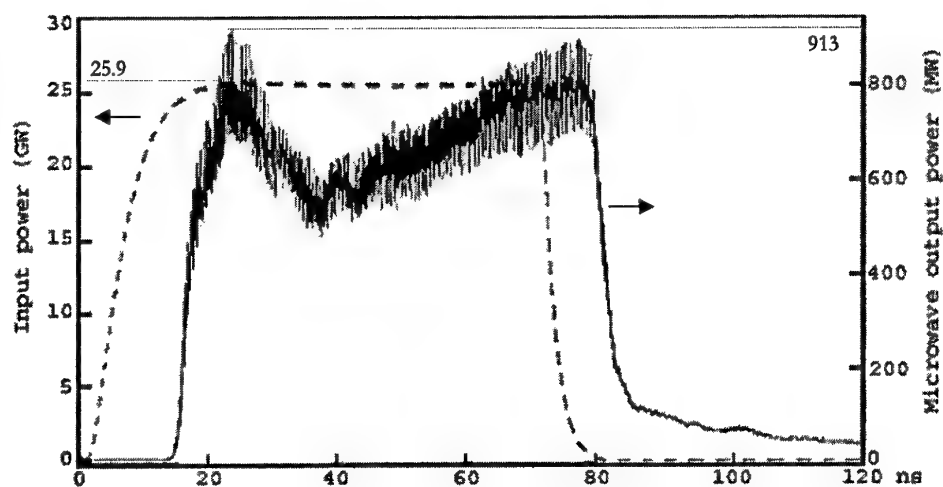
Figure 29 Simulation input and microwave output power pulses – improved design.
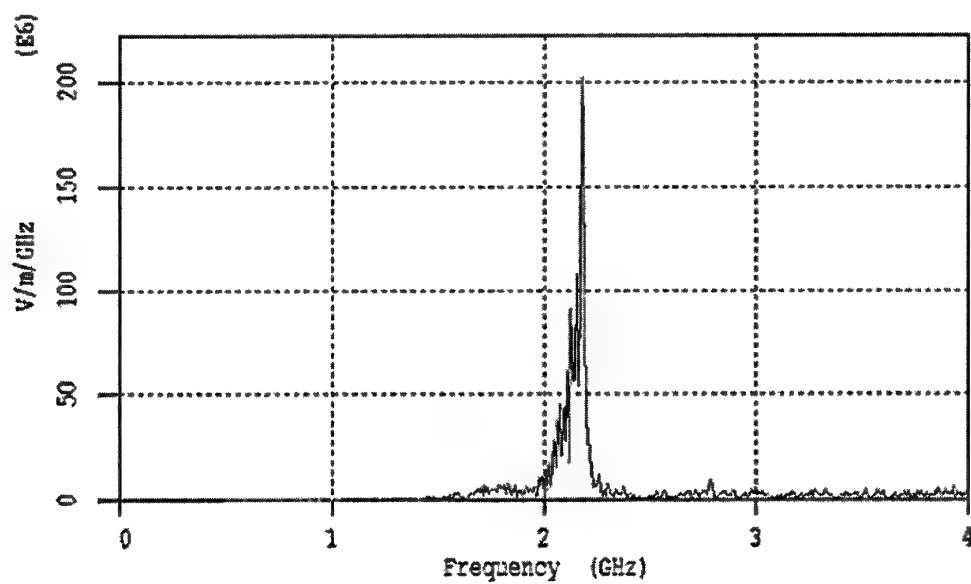
Figure 30 Frequency spectrum – improved design; main resonance at 2.153 GHz.

66

Part 2.

2.1. Introduction

In principle the electron beam generating element in an axial vircator, such as that shown in Fig. 1, can be represented by an inverted cylindrical diode with the cathode on the outside and the anode on the inside [1]. In the case of a vircator it is common to use a velvet cathode which is capable of delivering very high-density electron emission for a period of ~100 ns. Since the anode is semi-permeable, the electron beam passes through it virtually unhindered and enters the space inside the anode, where a virtual cathode can be formed, Fig. 2. It is this part of the device which we are now going to consider.

In order to simplify the algebra of the problem we choose plane rather than cylindrical geometry and use a short-circuited plane diode as a model for the space within the vircator's cylindrical anode, see II in Fig. 3. Here we assume that a single-velocity electron stream is generated in I and enters the inter-electrode space II, the entrance velocity of the electrons being governed by the anode/cathode potential difference V_a. Since the diode II is short-circuited, the exit electrode (collector) is kept at the same potential as the entrance electrode (anode). Also it is assumed that most of the time the anode collects no current, its sole purpose being to establish an idealised plane at potential V_a relative to the cathode. In the actual vircator there is no collector and the electrons gradually lose their radial velocity as they approach the axis, as shown in Fig. 2, but we would like to suggest that the addition of the collector, which is necessary to complete the circuit, is not likely to affect the basis of our argument.

Those of us who still recall vacuum tubes may remember that a system shown in Fig. 3 was thoroughly analysed by no lesser a man than Shockley [2]. However, he and others did it in the absence of a magnetic field and our task will be to see what happens when we introduce an external magnetic field parallel to the electrodes, as indicated in Fig. 3. Here, we have limited the presence of the magnetic field to region II; its presence in region I can be safely ignored, since no virtual cathode would be formed there, region I merely acting as a source of current for region II.

2.2. Magnetic diode model

It is generally recognised that the presence of a magnetic field substantially increases the power-handling capacity of a microwave tube; this feature greatly contributed to the success of the so-called M-type devices [3]. A simple physical explanation of the phenomenon can be gained with the help of Fig. 4, where we have a graphic representation of the Poisson equation in the absence and in the presence of a magnetic field. In the absence of the field we have a 'simple' form of the Poisson equation given by (2.1) and shown in Fig. 4, where curve (1) is a hyperbola asymptotic to horizontal and vertical axes.

$$\frac{d^2\bar{\phi}}{d\bar{x}^2} = -\bar{\rho} = -\frac{\bar{J}_c}{\bar{x}^{\cdot}} = -\frac{\bar{J}_c}{\sqrt{\bar{\phi}}} \tag{2.1}$$

Here we have used the 'bar' notation as explained in Appendix 1 in order to simplify the algebraic form of the equations. The main advantage of the bar notation is that the distance between the electrodes $\bar{x} = x/d$, and the electron entrance velocity $\bar{v} = v/v_1$ are both equal to unity.

In the absence of the magnetic field $\bar{x}^{\cdot 2} = \bar{\phi}$, which leads directly to (2.1). The introduction of a magnetic field alters the situation substantially since now $\bar{y}^{\cdot} \neq 0$ and hence the new energy balance is expressed by $\bar{\phi} = \bar{x}^{\cdot 2} + \bar{y}^{\cdot 2}$ (see (2.13)). Substituting for $\bar{x}^{\cdot}$ in the Poisson equation we now obtain

$$\frac{d^2\bar{\phi}}{d\bar{x}^2} = \frac{-\bar{J}_c}{\sqrt{\bar{\phi} - \bar{\omega}_{c0}^2 \bar{x}}} \qquad (2.2)$$

The corresponding curve (2) in Fig. 4 is asymptotic not to the vertical axis $\bar{\phi} = 0$, but to a vertical line $\bar{\phi} = \bar{\omega}_{c0}^2 \bar{x}^2 > 0$ and thus lies everywhere above curve (1). The physical meaning of the difference between curves (1) and (2) is quite significant. Let us consider the conditions at a fixed potential $\bar{\phi}$ and a fixed injection current density $\bar{J}_c$. Fig. 4 indicates that in the presence of the magnetic field the system can absorb a much higher space-charge density $\bar{\rho}$, curve (2) lying everywhere above curve (1), the difference growing as we approach $\bar{\phi} = \bar{\omega}_{c0}^2 \bar{x}^2$. Simplistically one could say that the electrons now have more 'room' for manoeuvre, being able to move sideways as well as forward. Algebraically the difference relies on the fact that only $\bar{x}$ enters in the calculation of the injection current density $\bar{J}_c$, whereas the energy balance expressed by $\bar{\phi}$ incorporates both $\bar{x}$ and $\bar{y}$.

2.3 Solution in terms of time

It is well known that in the analysis of steady-state electron beams it is algebraically much simpler to use time $\bar{t}$ rather than distance $\bar{x}$ as an independent variable, the two variables being interchangeable, $\bar{x} = \bar{x}(\bar{t})$. We propose therefore to carry out our analysis in terms of $\bar{t}$.

2.3.1 Basic equations

Using our bar notation the usual equations of motion for a single electron in the presence of a magnetic field are given by:

$$\bar{x}^{\cdot\cdot} = -\frac{1}{2}\bar{E} - \bar{\omega}_{c0}\bar{y}^{\cdot} \tag{2.3}$$

$$\bar{y}^{\cdot\cdot} = \bar{\omega}_{c0}\bar{x}^{\cdot} \tag{2.4}$$

where $\bar{E} = -\dfrac{d\bar{\phi}}{d\bar{x}}$, $\omega_{c0} = eB/m_0$ and $\bar{\omega}_{c0}$ is defined in Appendix 1. Similarly in a steady state the current density is defined by writing:

$$\bar{J}_c = \bar{\rho}\bar{x}^{\cdot} = \frac{d\bar{E}}{d\bar{x}}\bar{x}^{\cdot} = \bar{E}^{\cdot} \tag{2.5}$$

Differentiating (2.3) once with respect to time, substituting from (2.4) and then again from (2.5), we obtain

$$\bar{x}^{\cdots} = -\frac{1}{2}\bar{E}^{\cdot} - \bar{\omega}_{c0}\bar{y}^{\cdot\cdot} = -\frac{1}{2}\bar{J}_c - \bar{\omega}_{c0}^2\bar{x}^{\cdot}$$

or

$$\bar{x}^{\cdots} + \bar{\omega}_{c0}^2\bar{x}^{\cdot} = -\frac{1}{2}\bar{J}_c = \text{const} \qquad (2.6)$$

$\bar{J}_c$ being constant in 1D. We can easily recognise (2.6) as the DC part of the Llewellyn-Peterson equation when a magnetic field is present; the effect of the space charge is represented in (2.6) by the current density term $-\frac{1}{2}\bar{J}_c > 0$, electrons carrying negative charge. The solution of (2.6) is quite straightforward bearing in mind that in our notation we have at the entrance electrode: $\bar{x}_1 = 0$, $\bar{x}_1^{\cdot} = 1$ and $\bar{y}_1^{\cdot} = 0$.

$$\bar{x} = \frac{\bar{x}_1^{\cdot\cdot}}{\bar{\omega}_{c0}^2}(1-c) + \frac{1}{\bar{\omega}_{c0}}s - \frac{\bar{J}_c}{2\bar{\omega}_{c0}^3}(\theta - s) = -\frac{\bar{E}_1}{2\bar{\omega}_{c0}^2}(1-c) + \frac{1}{\bar{\omega}_{c0}}s + \frac{2t}{9\bar{\omega}_{c0}^3}(\theta - s) \qquad (2.7)$$

$$\bar{x}^{\cdot} = \frac{\bar{x}_1^{\cdot\cdot}}{\bar{\omega}_{c0}}s + c - \frac{\bar{J}_c}{2\bar{\omega}_{c0}^2}(1-c) \qquad = -\frac{\bar{E}_1}{2\bar{\omega}_{c0}}s + c + \frac{2t}{9\bar{\omega}_{c0}^2}(1-c) \qquad (2.8)$$

$$\bar{x}^{\cdot\cdot} = \bar{x}_1^{\cdot\cdot}c - \bar{\omega}_{c0}s - \frac{\bar{J}_c}{2\bar{\omega}_{c0}}s \qquad = -\frac{\bar{E}_1}{2}c - \bar{\omega}_{c0}s + \frac{2t}{9\bar{\omega}_{c0}}s \qquad (2.9)$$

where

$$\bar{\tau} = \bar{t} - \bar{t}_1, \quad s = \sin\bar{\omega}_{c0}\bar{\tau}, \quad c = \cos\bar{\omega}_{c0}\bar{\tau}, \quad \theta = \bar{\omega}_{c0}\bar{\tau} \qquad (2.10)$$

and

$$\bar{x}_1^{..} = -\frac{1}{2}\bar{E}_1 \qquad \text{from (2.3)} \qquad\qquad\qquad (2.11)$$

$$-\bar{J}_c = \frac{4}{9}\iota = \mathscr{I} \qquad \text{from (A1.2)} \qquad\qquad\qquad (2.12)$$

Once $\bar{E}_1$ is known for any give ι, the problem of potential and velocity distribution is solved since $\bar{x}$, $\bar{x}^{.}$ can be obtained from (2.7), (2.8) and $\bar{y}$, $\bar{y}^{.}$ from integrals of (2.4). This is a much quicker procedure, especially in the presence of an initial velocity, than any attempt to solve the Poisson equation (2.2) directly, as was common in the past for a zero initial velocity [4,5].

At this point it is convenient to introduce the usual energy balance equation. Multiplying (2.3) by $\bar{x}^{.}$, (2.4) by $\bar{y}^{.}$, adding and then integrating with respect to $\bar{t}$ we obtain

$$\bar{\phi} = \bar{x}^{.^2} + \bar{y}^{.^2} \qquad\qquad\qquad (2.13)$$

Here we have assumed, bearing in mind Fig. 3, that all electrons start with zero velocity at a cathode which is at zero potential, so that $\bar{\phi}_c = \bar{x}_c^{.} = \bar{y}_c^{.} = 0$. Thus, at the entrance electrode we have, by definition (see Appendix 1): $\bar{x}_1 = 0$, $\bar{\phi}_1 = \bar{x}_1^{.} = 1$, $\bar{y}_1^{.} = 0$. Since by integrating (2.4) once we obtain

$$\overline{y}^{\cdot} = \overline{\omega}_{c0}\overline{x} \qquad\qquad (2.14)$$

the substitution of (2.14) in (2.13) yields

$$\overline{\phi} = \overline{x}^{\cdot^2} + \overline{\omega}_{c0}^2 \overline{x}^2 \qquad\qquad (2.15)$$

For a short-circuited diode we have at the exit electrode $\overline{x}_2 = \overline{\phi}_2 = 1$ and the energy balance (2.15) reduces to

$$\overline{x}_2^{\cdot^2} = 1 - \overline{\omega}_{c0}^2 \qquad\qquad (2.16)$$

Soon we will use (2.16) as one of the boundary conditions.

2.3.2 Derivation of $\overline{E}_1(\iota)$

The next step in our investigations is to obtain a relationship between the injection current density ι and the electric field at the entrance electrode $\overline{E}_1$. In the absence of a magnetic field this relationship can be expressed directly in the form $\iota = \iota\left(\overline{E}_1\right)$ by writing (see (A2.12) in Appendix 2)

$$\mathscr{I} = \overline{E}_1\left(1 \mp \sqrt{1 - \frac{1}{3}\overline{E}_1}\right) \qquad\qquad (2.17)$$

This is no longer possible in the presence of the magnetic field. The best we can do now is to obtain the relevant curve in its parametric form by writing $\iota(\bar{\tau}_d)$, $\bar{E}_1(\iota,\bar{\tau}_d)$ where $\bar{\tau}_d$ is the total transit time between the electrodes. By assuming $\bar{y}_1 = 0$, putting $\bar{x} = \bar{x}_2 = 1$ in (2.7) and $\bar{x}_2' = \sqrt{1-\bar{\omega}_{c0}^2}$ in (2.8), we obtain from the two equations:

$$1 = -\frac{\bar{E}_1}{2\bar{\omega}_{c0}^2}(1-c_d) + \frac{1}{\bar{\omega}_{c0}}s_d + \frac{2\iota}{9\bar{\omega}_{c0}^3}(\theta_d - s_d) \tag{2.18}$$

$$\bar{x}_2' = \sqrt{1-\bar{\omega}_{c0}^2} = -\frac{\bar{E}_1}{2\bar{\omega}_{c0}}s_d + c_d + \frac{2\iota}{9\bar{\omega}_{c0}^2}(1-c_d) \tag{2.19}$$

where

$$s_d = \sin\bar{\omega}_{c0}\bar{\tau}_d, \quad c_d = \cos\bar{\omega}_{c0}\bar{\tau}_d, \quad \theta_d = \bar{\omega}_{c0}\bar{\tau}_d \tag{2.20}$$

Here as before the subscripts 1 and 2 refer respectively to entrance and exit electrodes. Substituting for $\bar{E}_1$ from (2.19) we obtain from (2.18), after some heavy algebra

$$\iota = \frac{9}{2}\bar{\omega}_{c0}^2 \frac{\left(1+\sqrt{1-\bar{\omega}_{c0}^2}\right)\tan\left(\frac{1}{2}\bar{\omega}_{c0}\bar{\tau}_d\right) - \bar{\omega}_{c0}}{2\tan\left(\frac{1}{2}\bar{\omega}_{c0}\bar{\tau}_d\right) - \bar{\omega}_{c0}\bar{\tau}_d} \tag{2.21}$$

We can now substitute (2.21) in (2.19) in order to obtain the following expression for the electric field at the entrance electrode:

$$\bar{E}_1 = 2\bar{\omega}_{c0} \left[\frac{\left(1 - \sqrt{1 - \omega_{c0}^2}\right) - \left(1 + \sqrt{1 - \omega_{c0}^2}\right)\tan^2\left(\frac{1}{2}\bar{\omega}_{c0}\bar{\tau}_d\right)}{2\tan\left(\frac{1}{2}\bar{\omega}_{c0}\bar{\tau}_d\right)} + \frac{2\iota}{9\bar{\omega}_{c0}^2}\tan\left(\frac{1}{2}\bar{\omega}_{c0}\bar{\tau}_d\right) \right] \qquad (2.22)$$

At the cut-off we have, by definition, $\bar{x}_2 = \sqrt{1 - \bar{\omega}_{c0}^2} = 0$, so that $\bar{\omega}_{c0} = 1$ and (2.21), (2.22) acquire a simpler form given by

$$\iota = \frac{9}{4} \frac{\tan\left(\frac{1}{2}\bar{\tau}_d\right) - 1}{\tan\left(\frac{1}{2}\bar{\tau}_d\right) - \frac{1}{2}\bar{\tau}_d} \qquad (2.23)$$

$$\bar{E}_1 = 2 \left[\frac{1 - \tan^2\left(\frac{1}{2}\bar{\tau}_d\right)}{2\tan\left(\frac{1}{2}\bar{\tau}_d\right)} + \frac{2\iota}{9}\tan\left(\frac{1}{2}\bar{\tau}_d\right) \right] \qquad (2.24)$$

An expression similar to (2.21) has been derived by others [6], but their boundary conditions and notation differ from ours.

A graphical presentation of the results is provided in Fig. 5 where we have the electric field at the entrance electrode $\bar{E}_1$ as a function of the injection current density ι for different values of the magnetic field B, expressed in terms of the reduced electron gyro-frequency $\bar{\omega}_{c0}$ defined in Appendix 1. Two points of particular interest have been respectively marked A and B in Fig. 5 and they will be considered separately. It should be noted that all curves start at the origin in Fig. 5; this confirms the obvious fact that irrespective of the value of the magnetic field, the electric field at the entrance electrode $\bar{E}_1 = 0$ in the absence of space charge, $\bar{\rho} = 0$ or $\iota = 0$ in a single-stream *conducting* diode.

76

Point A

At point A the injection current density ι reaches its maximum value for a given $\bar{\omega}_{c0}$.

The value ι_{max} is obtained by differentiating (2.21) with respect to $\bar{\tau}_d$ and then putting

$\frac{d\iota}{d\bar{\tau}_d} = 0$. After some algebra we obtain

$$\left(1+\sqrt{1-\bar{\omega}_{c0}^2}\right)\left(\theta_d - s_d\right) = \bar{\omega}_{c0}\left(1-c_d\right) \tag{2.25}$$

which must be satisfied by $\bar{\tau}_d$ for any given $\bar{\omega}_{c0}$. The maximum value of the injection current is then given by

$$\mathscr{I}_{max} = \frac{4}{9}\iota_{max} = \frac{2\bar{\omega}_{c0}^3}{\theta_d - s_d} = \frac{2\bar{\omega}_{c0}^2\left(1+\sqrt{1-\bar{\omega}_{c0}^2}\right)}{1-c_d} \tag{2.26}$$

Here θ_d, s_d and c_d are defined in (2.20).

We now find from Fig. 5 that as the magnetic field increases, i.e. as $\bar{\omega}_{c0}$ grows from zero for $B=0$ to $\bar{\omega}_{c0}=1$ for the cut-off value $B=B_H$, the maximum value of the injection current ι (point A) decreases until it suddenly drops to zero for $B > B_H$ (not shown). All this is in agreement with our discussion of the general effect of the magnetic field presented in Section 2.2. As the magnetic field increases at a fixed value of the space charge density $\bar{\rho}$ the tangential component $-\bar{J}_y$ grows at the expense of the perpendicular component $-\bar{J}_x = -\bar{J}_c = (4/9)\iota$; thus for $B=0$ or $\bar{\omega}_{c0}=0$ we have

$-\overline{J}_y = 0$, $-\overline{J}_x > 0$ and for $B > B_H$ or $\overline{\omega}_{c0} > 1$ we have $-\overline{J}_y > 0$, $-\overline{J}_x = 0$ (note: $-\overline{J}_x = 0$ or $\iota = 0$ *does not* imply $\overline{\rho} = 0$ in the presence of a double-stream flow). Table 2.1 gives the values of ι_{max} and $\mathscr{S}_{max} = (4/9)\iota_{max}$ for several values of the magnetic field expressed by $\overline{\omega}_{c0}$. The curve joining all the $\iota = \iota_{max}$ or A points is shown dotted in Fig. 5. For the sake of completeness the corresponding values of the transit time $\overline{\tau}_{d,max}$, the transit angle $\overline{\theta}_{max} = \overline{\omega}_{c0}\overline{\tau}_{d,max}$ and the electric field at the entrance electrode $\overline{E}_1$ have also been included.

Typical potential $\overline{\phi}$ and velocity $\overline{x}^{\cdot 2}$ distributions for different values of $\overline{\omega}_{c0}$ are shown in Figs. 6a and b respectively. Here for typographic convenience we have called the x-directed velocity $\overline{u}$ rather than $\overline{x}^{\cdot}$.

Point B

Let us now consider the second point of interest, viz point B. It has been shown by others [7] that in the absence of the magnetic field, $\overline{\omega}_{c0} = 0$, all points lying on the lower branch of the curve between the origin and point A represent stable conditions, whereas all points between A and B represent unstable solutions, the curve becoming meaningless beyond B due to the formation of a virtual cathode which introduces discontinuity in ι. Physically when an attempt is made to increase the injection current ι beyond its maximum value ι_{max}, the system rapidly collapses: first the potential $\overline{\phi}$ and hence the electron velocity precipitously drops to zero, point B in Fig. 5 and then the position of the virtual cathode is shifted by splitting ι into ι_2 reaching the exit electrode and $\iota_1 = \iota - \iota_2$ returning to the entrance electrode. The best physical description of the

78

process can be found in [8]. It is now suggested that similar conditions should prevail in the presence of the magnetic field, i.e. that the lower section of each curve for $0 < \iota < \iota_{max}$ would represent stable solutions, whereas the upper part of each curve would indicate unstable solutions. Since the operation of a vircator depends on the formation of a virtual cathode, it is essential to know what happens to it in the presence of a magnetic field, bearing in mind that now $\bar{\phi}$ is no longer equal to $\overline{x}^{-2}$ but is given by (2.15).

At this point it is essential to distinguish between two types of instability. In Fig. 9 curve A′ is stable, curve A is conditionally stable ($\iota = \iota_{max}$) and curve B is inherently unstable; that means that in the case of curve B the real part of the corresponding Llewellyn-Peterson coefficient (in this case a_{11}) has a positive real part. In this case of curves A′ and A the real part of a_{11} is respectively negative and zero. When we attempt to increase the injection current ι beyond its maximum value ι_{max}, the system jumps from solution A , to solution C , momentarily going through a potential distribution resembling B (the corresponding idealized 'stead state' solution would have $\iota < \iota_{max}$). The solution C is characterised by the appearance of a virtual cathode and the corresponding partial reflection of current. Although possible in theory, such a situation cannot exist in practice, largely due to inhomogeneities of the system. Therefore in practice the solution becomes unstable, the system continuously relaxing between solutions with and without a virtual cathode, thus giving rise to oscillations. Exactly the same argument applies in the presence of the magnetic field, as indicated in Figs. 10a and b, Fig. 8a merely indicating a general scheme of things. What is important from the point of view of a vircator, that as the magnetic field increases, the amplitude of the corresponding oscillations decreases until they are finally extinguished when the magnetic

field approaches its cut-off value. In the limit at the collector $v_x = 0$, $\rho = \infty$, $\iota = \iota_{injection}$, the next step being an abrupt drop of ι to zero as the magnetic field increases beyond its cut-off value, the flow of electrons across region II in Fig. 2 ceasing altogether.

Let us continue with our idealised model of an infinitely smooth or jelly-like electron stream. The first step in finding point B is to note that the moment of electron 'hesitancy' ($\overline{x}^{\cdot} = \overline{x}^{\cdot\cdot} = 0$), which in the absence of the magnetic field is normally referred to as a 'virtual cathode', is no longer associated with $\overline{\phi} = 0$, but occurs at some other value of $\overline{\phi} = \overline{\phi}_B$. As an example let us consider electron trajectories for $\overline{\omega}_{c0} = 0.5$ and several values of the injection current ι, as shown in Fig. 7. Clearly there is one value of $\iota = \iota_B$ for which an electron momentarily travels parallel to the cathode, $\overline{x}^{\cdot} = 0$. We then find from (2.9) that at the same point we also have $\overline{x}^{\cdot\cdot} = 0$; thus just as was the case for $\overline{x}^{\cdot} = 0$ and $\overline{\omega}_{c0} = 0$, the electron now 'hesitates' whether to turn towards the exit or the entrance electrode. Physically this implies that at point B the electric force $-\frac{1}{2}\overline{E}_B > 0$ exactly balances the magnetic force $-\overline{\omega}_{c0}\overline{y}^{\cdot} < 0$ (see (2.3)). In general point B can be found by first putting $\overline{x}^{\cdot\cdot} = \overline{x}^{\cdot} = 0$ in (2.8), (2.9) and then expressing $\overline{E}_1$ and ι in terms of $\overline{\tau}_B$. This gives us

$$\mathscr{I}_B = \frac{4}{9}\iota_B = \frac{2\overline{\omega}_{c0}^2}{1-c_B}, \qquad\qquad \overline{E}_{1B} = \frac{2\overline{\omega}_{c0}s_B}{1-c_B} \qquad\qquad (2.27)$$

where

$$s_B = \sin\overline{\omega}_{c0}\overline{\tau}_B, \quad c_B = \cos\overline{\omega}_{c0}\overline{\tau}_B \qquad\qquad (2.28)$$

80

(2.27) being a parametric representation of a curve. The cross section of (2.27) and $\overline{E}_1(\iota)$ gives us point B which defines the one particular trajectory for which momentarily the x-directed velocity and acceleration disappear, $\overline{x}^{\cdot} = \overline{x}^{\cdot\cdot} = 0$. For clarity B points have been connected by a dotted line in Fig. 5. The corresponding values of ι_B, $\mathscr{I}_B$, $\overline{\tau}_{d,B}$, $\overline{\theta}_B$, $\overline{E}_{1B}$ and $\overline{\tau}_B$ are shown in Table 2.2.

It should be noted that for the cut-off condition, $\overline{\omega}_{c0} = 1$ the two points A and B coalesce, the large loop of the $\overline{E}_1 = \overline{E}_1(\iota)$ curve collapsing to a cusp.

2.3.3 The new 'virtual cathode'

In the presence of a magnetic field the conditions for virtual cathode have to be reconsidered. We start by suggesting that *all* B points represent a highly unstable solution, which is similar to that obtained in the absence of a magnetic field. A more likely stable solution is shown in Fig. 8a where, following the example of $\overline{\omega}_{c0} = 0$, we have abandoned the continuity of ι by assuming that only its fraction ι_2 reaches the exit electrode (collector), the rest, i.e. $\iota_1 = \iota - \iota_2$ turning back and landing on the entrance electrode (anode). We shall see that this requires a shift in the position of the $\overline{x}^{\cdot\cdot} = \overline{x}^{\cdot} = 0$ plane from $\overline{x}_B$ to some new position $\breve{\overline{x}}$, an example of corresponding electron trajectories for $\overline{\omega}_{c0} = 0.5$ being shown in Fig. 8b . However we will show that for a cut-off magnetic field, $B \rightarrow B_H$ or $\overline{\omega}_{c0} \rightarrow 1$ from below, the plane $\overline{x} = \breve{\overline{x}}$ must move to the exit electrode, making then $\breve{\overline{x}} = \overline{x}_2 = 1$. Since the potential of the exit electrode is kept

constant, this will destroy the function of a 'virtual cathode' and should stop the vircator oscillations altogether.

When discussing either a diode [7] or a vircator [10-12] we invariably start with the assumption that the beam is perfectly smooth. We then discover as we have pointed out before that in the absence of the magnetic field some solutions are stable and other solutions are unstable, the unstable solution (B in Fig .9) leading to the discontinuity of current flow and the formation of a virtual cathode (C in Fig. 9). This is an idealized situation based on an infinitely smooth model of electron flow. Any departure from that assumption causes instability and fluctuations in the form of appearance and disappearance of the virtual cathode, thus forming the basis of operation of a vircator. Thus in practice the system is capable of generating relaxation oscillations which then generate electromagnetic oscillations in the output waveguide, Fig. 1. We have followed exactly the same path in analyzing the situation in the presence of a magnetic field. In the process we have defined an equivalent of the C distribution, but now in the presence of the magnetic field (Fig. 8a & C in Fig. 10b), and have shown that the amplitude of the corresponding virtual cathode oscillations gradually decreases as the magnetic field increases.

Let us now put the above brief discussion into an algebraic form. First of all we require equations of motion which would apply in part a of the inter-electrode space, Fig. 8a. Since $\bar{x}^{\cdot} = \bar{x}^{\cdot\cdot} = 0$ by definition at $\bar{x} = \breve{x}$, we obtain from (2.7)-(2.9):

$$\breve{\bar{x}} = -\frac{\bar{E}_1}{2\bar{\omega}_{c0}^2}\left(1-\breve{c}\right)+\frac{1}{\bar{\omega}_{c0}}\breve{s}+\frac{\mathcal{J}_a}{2\bar{\omega}_{c0}^3}\left(\breve{\theta}-\breve{s}\right) \tag{2.29}$$

$$\breve{\overline{x}}{}^{\cdot} = 0 = -\frac{\overline{E}_1}{2\overline{\omega}_{c0}}\breve{s} + \breve{c} + \frac{\mathscr{I}_a}{2\overline{\omega}_{c0}^2}\left(1 - \breve{c}\right) \tag{2.30}$$

$$\breve{\overline{x}}{}^{\cdot\cdot} = 0 = -\frac{\overline{E}_1}{2}\breve{c} - \overline{\omega}_{c0}\breve{s} + \frac{\mathscr{I}_a}{2\overline{\omega}_{c0}}\breve{s} \tag{2.31}$$

where $\breve{\theta} = \overline{\omega}_{c0}\breve{\overline{\tau}}$, $\breve{s} = \sin \overline{\omega}_{c0}\breve{\overline{\tau}}$, $\breve{c} = \cos \overline{\omega}_{c0}\breve{\overline{\tau}}$ \hfill (2.32)

$\breve{\overline{\tau}}$ being the electron transit time from the entrance electrode at $\overline{x} = \overline{x}_1 = 0$ to the point $\overline{x} = \breve{\overline{x}}$. Here $\mathscr{I}_a$ is the 'current' density in section a of the diode; it consists of the injection current $\mathscr{I}$ and the additional part $\mathscr{I}_1 = \mathscr{I} - \mathscr{I}_b$ which represents the electrons returning to the entrance electrode. Therefore from the point of view of electron space charge the two current streams travelling in opposite directions must be *added* and we write

$$\mathscr{I}_a = 2\mathscr{I} - \mathscr{I}_b = \frac{4}{9}\left(2\iota - \iota_2\right) \tag{2.33}$$

since $\iota_b = \iota_2$ and $\mathscr{I}_b = \mathscr{I}_2$. In part b of the inter-electrode space the equations of motion and the boundary conditions are somewhat different. Introducing new variables:

$$\overline{X} = \overline{x} - \breve{\overline{x}}, \quad \overline{X}{}^{\cdot} = \overline{x}{}^{\cdot} - \breve{\overline{x}}{}^{\cdot} = \overline{x}{}^{\cdot}$$

$$\tag{2.34}$$

$$\overline{Y} = \overline{y} - \breve{\overline{y}}, \quad \overline{Y}{}^{\cdot} = \overline{y}{}^{\cdot} - \breve{\overline{y}}{}^{\cdot} = \overline{\omega}_{c0}\overline{X}$$

83

we can write in place of (2.7)-(2.9):

$$\bar{X} = \frac{\mathscr{I}_2}{2\bar{\omega}_{c0}^3}(\Theta - S) \qquad (2.35)$$

$$\bar{X}^{\cdot} = \frac{\mathscr{I}_2}{2\bar{\omega}_{c0}^2}(1 - C) \qquad (2.36)$$

$$\bar{X}^{\cdot\cdot} = \frac{\mathscr{I}_2}{2\bar{\omega}_{c0}}S \qquad (2.37)$$

where

$$\Theta = \bar{\omega}_{c0}T = \theta_d - \breve{\theta} = \bar{\omega}_{c0}\left(\bar{\tau}_d - \breve{\tau}\right), \; S = \sin\bar{\omega}_{c0}T, \; C = \cos\bar{\omega}_{c0}T, \; \mathscr{I}_b = \mathscr{I}_2. \qquad (2.38)$$

We note that, by definition, $\breve{\bar{x}}^{\cdot\cdot} = \breve{\bar{x}}^{\cdot} = 0$ in the plane $\bar{x} = \breve{\bar{x}}$ and only $\mathscr{I}_2 = \frac{4}{9}\iota_2$ reaches the exit electrode. Introducing boundary conditions at the exit electrode we now obtain from (2.35), (2.36):

$$\bar{X}_2 = 1 - \breve{\bar{x}} = \frac{\mathscr{I}_2}{2\bar{\omega}_{c0}^3}(\Theta_2 - S_2) \qquad (2.39)$$

$$\bar{X}_2^{\cdot} = \bar{x}_2^{\cdot} = \sqrt{1 - \bar{\omega}_{c0}^2} = \frac{\mathscr{I}_2}{2\bar{\omega}_{c0}^2}(1 - C_2) \qquad (2.40)$$

84

The system has now been fully specified, since there are five simultaneous equations (2.29)-(2.31), (2.39), (3.40) and five unknowns: $\breve{\bar{x}}$, $\mathcal{I}_a$ (or $\mathcal{I}_2$), $\breve{\bar{\tau}}$, $\bar{\tau}_d$ and $\bar{E}_1$, the values of the magnetic field $\bar{\omega}_{c0}$ and the injection current $\mathcal{I} = \frac{4}{9}\iota$ being given.

At this point it is preferable to reduce the number of equations from five to two. We do that by noting that by eliminating $\bar{E}_1$ we obtain from (2.30), (2.31)

$$\mathcal{I}_a = \frac{2\bar{\omega}_{c0}^2}{1-\breve{c}} = 2\mathcal{I} - \mathcal{I}_2 \tag{2.41}$$

and hence from either (2.30) or (2.31):

$$\frac{1}{2}\bar{E}_1 = \frac{\bar{\omega}_{c0}\breve{s}}{1-\breve{c}} \tag{2.42}$$

Substituting in (2.29) we now obtain

$$\breve{\bar{x}} = \frac{\breve{\theta} - \breve{s}}{\bar{\omega}_{c0}\left(1-\breve{c}\right)} \tag{2.43}$$

Eliminating $\breve{\bar{x}}$ between (2.39) and (2.43) we have

$$\frac{\breve{\theta} - \breve{s}}{\bar{\omega}_{c0}\left(1-\breve{c}\right)} = 1 - \frac{\mathcal{I}_2}{2\bar{\omega}_{c0}^3}\left(\Theta_2 - S_2\right) \tag{2.44}$$

Using now (2.41) to eliminate $\mathcal{I}_2$ in favour of $\mathcal{I}$, which is given, we finally obtain

$$\frac{\breve{\theta}-\breve{s}}{\bar{\omega}_{c0}\left(1-\breve{c}\right)}=1-\frac{\mathcal{I}\left(1-\breve{c}\right)-\bar{\omega}_{c0}^2}{\bar{\omega}_{c0}^3\left(1-\breve{c}\right)}\left(\Theta_2-S_2\right) \tag{2.45}$$

Also eliminating $\mathcal{I}_2$ from (2.39) and (2.40) we obtain, by substituting for $\breve{\bar{x}}$ from (2.43)

$$1-\frac{\breve{\theta}-\breve{s}}{\bar{\omega}_{c0}\left(1-\breve{c}\right)}=\sqrt{1-\bar{\omega}_{c0}^2}\;\frac{\Theta_2-S_2}{\bar{\omega}_{c0}\left(1-C_2\right)} \tag{2.46}$$

Using (2.46) the previous equation (2.45) can be further simplified by writing

$$\bar{\omega}_{c0}^2\sqrt{1-\bar{\omega}_{c0}^2}=\left[\mathcal{I}\left(1-\breve{c}\right)-\bar{\omega}_{c0}^2\right]\frac{1-C_2}{1-\breve{c}} \tag{2.47}$$

Thus the problem has now been reduced to the solution of two simultaneous algebraic equations, (2.46), (2.47) with two unknowns, $\breve{\theta}$ (or $\breve{\bar{\tau}}$) and $\Theta_2=\theta_d-\breve{\theta}$ (or $\bar{\tau}_2=\bar{\tau}_d-\breve{\bar{\tau}}$), both the magnetic field $\bar{\omega}_{c0}$ and the injection current $\mathcal{I}=\frac{4}{9}\iota$ being given. Once that has been achieved, the remaining unknowns, i.e. $\breve{\bar{x}}$, $\mathcal{I}_1$ (or $\mathcal{I}_2$) and $\bar{E}_1$, can be obtained respectively from (2.41)-(2.43). As an example we have in Table 2.3 the values of the above variables for $\iota=\iota_{max}$ and six different values of $\bar{\omega}_{c0}$.

Table 2.1 Maximum injection current at different values of the magnetic field $\bar{\omega}_{c0}$

$\bar{\omega}_{c0}$	l_{max}	$\mathscr{I}_{max}$	$\bar{\tau}_{d,max}$	$\bar{\theta}_{max}$	$\bar{E}_1$
0.00	8.0000	3.5556	1.5000	—	2.6667
0.50	7.1360	3.1715	1.5745	0.78722	2.4080
0.80	5.5425	2.4633	1.7518	1.4014	1.8969
0.90	4.6428	2.0635	1.8872	1.6984	1.5837
0.95	4.0082	1.7814	2.0071	1.9067	1.3491
1.00	2.5781	1.1458	2.4120	2.4120	0.76376

Table 2.2 Parameters for defining point B for different values of the magnetic field $\bar{\omega}_{c0}$

$\bar{\omega}_{c0}$	l_B	$\mathscr{I}_B$	$\bar{\tau}_{d,B}$	$\bar{\theta}_B$	$\bar{E}_{1,B}$	$\bar{\tau}_B$
0.00	4.0000	1.7778	3.0000	—	2.6667	1.50000
0.50	3.5426	1.5745	3.1637	0.8197	2.3017	1.6295
0.80	2.9228	1.2990	3.3840	1.5562	1.6245	1.9344
0.90	2.7262	1.2116	3.2577	1.9146	1.2675	2.1253
0.95	2.6651	1.1845	3.3065	2.1222	1.0620	2.2458
1.00	2.5781	1.1458	2.4120	2.4120	0.7637	2.4120

Table 2.3 Conditions at a 'virtual cathode' in the presence of a magnetic field $\bar{\omega}_{c0}$

$\bar{\omega}_{c0}$	ι_{max}	$\breve{\bar{\tau}}$	$\bar{\tau}_d$	$\breve{\bar{x}}$	$\bar{E}_1$	ι_2
0.00	8.0000	0.7977	3.0000	0.2659	5.0145	1.8558
0.50	7.1360	0.8481	3.2112	0.2844	4.6455	1.5699
0.80	5.5425	0.9724	3.7588	0.3308	3.9040	1.0718
0.90	4.6428	1.0717	4.2310	0.3687	3.4384	0.8129
0.95	4.0082	1.1630	4.7025	0.4041	3.0822	0.6420
1.00	2.5781	2.4120	2.4120	1.0000	0.7638	(0.0000)

2.3.4 Numerical examples

Let us now consider some numerical examples by choosing three different cases: $\bar{\omega}_{c0} = 0$ (no magnetic field), $\bar{\omega}_{c0} = 0.5$ and $\bar{\omega}_{c0} = 1.0$ (cut-off condition). In Fig. 9 we have four well-known potential distributions when $\bar{\omega}_{c0} = 0$ [2]: they are $\iota = \iota_{max} = 8.0$ (curve A — marginally stable), $\iota = \iota_{+}$ where ι_{+} is fractionally greater than ι_{max} and thus generates a virtual cathode at $\breve{x} = 0.2659$ (see Table 3.3) and the dotted unstable potential distribution (curve B) associated with point B in Fig. 5. This distribution is by-passed on the way to the ι_{+} distribution, which is nominally stable, curve C. It is well known that if $\iota = \iota_{+}$ is then reduced, the virtual cathode persists until $\iota = 4.0$ and $\breve{x} = 0.5$, when the potential minimum suddenly jumps to $\bar{\phi}_{m} = 0.75$, thus giving rise to a new distribution A'. This generates a hysteresis effect which was of great interest in the past [2] and is now of fundamental importance in the operation of vircators.

A word of explanation is required at this point. According to our model, Fig. 3, the value of the injection current ι is determined by the space charge limited diode I; for a fixed V_a we have $\iota = 1$ when $d_0 = d$ and $\iota >< 1$ for $d_0 <> d$. When the potential distribution in the short-circuited diode II follows A or A' in Fig. 9, then $\iota_2 = \iota$ and hence $\iota - \iota_2 = 0$, no current flowing from the anode to the battery, the whole of the injection current ending up on the collector. When we try to increase the injection current beyond $\iota = \iota_{max}$ to what we have called ι_{+}, the system responds discontinuously and adopts the potential distribution C. Now only ι_2 part of the 'injection current' ι reaches the collector, the rest i.e. $\iota - \iota_2$ reaching the battery directly via the anode connection, as shown in Fig. 3. Since more electrons enter the short-circuited diode than

reach the collector, we allow for it from the *space-charge* point of view by writing, using Figs. 8a and 8b, $t_a = 2t - t_2$, $t_b = t_2$. Here possible misunderstanding may arise since following the tradition we use current density, which is a vector quantity, to simulate space charge density, which is a scalar.

In the presence of the magnetic field the situation is more complex since we now have $\bar{\phi} = \bar{x}^{\cdot 2} + \bar{y}^{\cdot 2} \neq \bar{x}^{\cdot 2} = \bar{u}^2$. Putting $\bar{\omega}_{c0} = 0.5$ and $t = t_{max} = 7.1360$ from Table 2.1 we now obtain Fig. 10a, where again curve A is plotted for $t = t_{max}$ and curve C for $t = t_+$, the unstable solution B being shown dotted. A similar hysteresis effect is present if we now start reducing t_+, the zero point of the $\bar{u}^2$-curve creeping along until it reaches $\breve{\bar{x}} = 0.55548$; the continuity of the current is then momentarily restored at $t = t_2 = 3.5831$, but since the distribution is unstable the zero point of the $\bar{u}^2$-curve jumps up to $\bar{u}^2_{min} = 0.6800$ to form the minimum of a stable distribution represented by curve A′. In Fig. 10b we have a similar sequence of events, but now expressed in terms of the potential distribution $\bar{\phi}$. Here we note that due to the presence of $\bar{y}$-directed velocities the potential function is never equal to zero, even when $\bar{u}^2 = 0$. Also, if we compare the size of the $\bar{u}^2$ jump in Fig. 10a, it is only 91% of that in the absence of the magnetic field, Fig. 9. This trend continues as the magnetic field increases (e.g. 68% for $\bar{\omega}_{c0} = 0.8$) and it is bound to affect unfavourably the performance of a vircator.

As another example let us consider the distribution of the velocity function $\bar{u}^2$ for different values of the injection current t (or $\mathcal{T}$) and a fixed value of $\bar{\omega}_{c0}$, choosing $\bar{\omega}_{c0} = 0.5$ and 1.0 as lying at two ends of the range of values of the magnetic field for a

conducting diode. We find that the value of the injection current has a profound effect on the shape of the velocity function $\bar{u}^2(\bar{x})$, as could be inferred from Fig. 3.10. Thus in the case of $\bar{\omega}_{c0} = 0.5$ the curve corresponding to zero value of the injection current exhibits a negative second derivative, whereas all the other curves shown in Fig. 11a have a positive second derivative. At the same time the position of the minimum moves towards the centre as $\mathscr{I}$ increases, although it never quite reaches it. The situation is even more interesting in the cut-off case, i.e. for $\bar{\omega}_{c0} = 1$. Now the only two curves which exhibit a min/max are those for $\iota = 0$ and $\iota = \iota_{max}$, the first having a maximum at the entrance electrode, $\bar{x} = 0$ and the second having a minimum at the exit electrode, $\bar{x} = 1$. The remaining curves exhibit neither a minimum nor a maximum point, but only an inflexion point at $\bar{u}^2 = \frac{1}{4}\mathscr{I}^2$, as indicated in Fig. 3.9 for $\bar{\omega}_{c0} = 1$.

It is interesting to note that unlike the potential $\bar{\phi}$, some $\bar{u}^2$ - curves, in particular those shown in Fig. 11, exhibit *negative* curvature over part of the inter-electrode space. This is in keeping with the corresponding differential equation which is obtained from (2.15) and (2.2) by writing

$$\frac{d^2\bar{u}^2}{d\bar{x}^2} = \frac{d^2\bar{\phi}}{d\bar{x}^2} - 2\bar{\omega}_{c0}^2 = \frac{\mathscr{I}}{\bar{u}} - 2\bar{\omega}_{c0}^2 \tag{2.48}$$

The related Fig. 12 clearly indicates that the second derivative of $\bar{u}^2$ may have both positive *and* negative values, the point of inflexion D in Fig. 11b being given by

$$\bar{u} = \frac{\mathcal{I}}{2\bar{\omega}_{c0}^2} = \frac{2\iota}{9\bar{\omega}_{c0}^2}$$

(2.49)

As the third example we must now consider the crucial case of $\bar{\omega}_{c0} = 1$, i.e. the 'cut-off' condition. We find from Table 2.3 that for $\iota = \iota_{max}$ the point $\breve{\bar{x}}$ has moved to the exit electrode, the corresponding $\bar{u}^2$-distribution being shown in Fig. 11b; at the same time ι_2 disappears altogether. It is important from our point of view to note that $\breve{\bar{x}} = \bar{x}_2 = 1$ and thus it is now situated at the collector where $\bar{u}^2 = 0$ and the potential is fixed, $\bar{\phi}_2 = 1$; consequently any attempt at increasing the injection current from ι_{max} to ι_+ would be rejected by the system, the excess current $\iota_+ - \iota_{max}$ merely flowing back to the battery through the anode conductor. Thus in this case the hysteresis effect and with it the generating mechanism for vircator oscillations would disappear altogether.

2.4 Solutions in terms of distance

In order to obtain an alternative description of our system, let us now use the distance $\overline{x}$ as an independent variable and attempt to solve the corresponding Poisson equation. We would then obtain either the potential $\overline{\phi}$ or the velocity $\overline{x}^{\cdot}$ directly as functions of $\overline{x}$. In the absence of an initial velocity such solutions have been obtained in a distant past [7,8], but to our knowledge they have never been extended to the more general case which is of interest to us here, and which includes the presence of a single initial velocity, in our case $\overline{x}_i^{\cdot} = 1$.

It should be added that in principle (2.7) – (2.9) are adequate to obtain all the information we require, since for any given $\overline{\tau}$ the distance $\overline{x}$ and the corresponding velocity $\overline{x}^{\cdot}$ can be obtained respectively from (2.7) and (2.8), once $\overline{\omega}_{c0}$ and ι have been chosen. The corresponding potential function $\overline{\phi} = \overline{\phi}(\overline{x})$ can then be obtained from (2.15). However, it seemed desirable for the sake of completeness and as an additional check on the correctness of our earlier results to solve the Poisson equation directly. In 1D the two basic equation are given, by the following simplified expressions

$$\frac{d^2\overline{\phi}}{d\overline{x}^2} = -\frac{d\overline{E}}{d\overline{x}} = -\overline{\rho} > 0 \qquad\qquad \text{Poisson equation} \qquad\qquad (2.50)$$

$$\frac{d}{d\overline{x}}\overline{J}_c = \frac{d}{d\overline{x}}(\overline{\rho}\overline{x}^{\cdot}) = 0 \qquad\qquad \text{Continuity equation} \qquad\qquad (2.51)$$

The latter equation establishes the following important property of $\overline{J}_c$ in 1D

$$\overline{J}_c = \text{const} \tag{2.52}$$

Substituting (2.15) in the Poisson equation (2.50) and using our definition for the current density (2.5) we obtain

$$\frac{d^2\overline{\phi}}{d\overline{x}^2} = -\overline{\rho} = \frac{-\overline{J}_c}{\overline{x}^{\cdot}} = \frac{\mathscr{I}}{\overline{u}} = \frac{\mathscr{I}}{\sqrt{\overline{\phi} - \overline{\omega}_{c0}^2 \overline{x}^2}} \tag{2.53}$$

Here we have used $\mathscr{I} = -\overline{J}_c$ and $\overline{u} = \overline{x}^{\cdot}$ for typographical convenience. At this point it is important to note that in the absence of the magnetic field $\overline{u}^2 = \overline{\phi}$, so that the two functions are identical. This is no longer the case in the presence of the magnetic field, as is indicated by (2.15). Since now the appearance of a virtual cathode is associated with $\overline{u}^2 = 0$ and not $\overline{\phi} = 0$, we must alter (2.53) in order to obtain $\overline{u}^2 = \overline{u}^2(\overline{x})$ rather then $\overline{\phi} = \overline{\phi}(\overline{x})$. This also conveniently removes the independent variable $\overline{x}$ from the denominator on the right hand side of (2.53). Differentiating (2.15) twice with respect to $\overline{x}$ we obtain.

$$\frac{d^2\overline{\phi}}{d\overline{x}^2} = \frac{d^2\overline{u}^2}{d\overline{x}^2} + 2\overline{\omega}_{c0}^2 \tag{2.54}$$

and after substitution in (2.53)

$$\frac{d^2\overline{u}^2}{d\overline{x}^2} = \frac{\mathscr{I}}{\overline{u}} - 2\overline{\omega}_{c0}^2 \tag{2.55}$$

At this point it is important to note that the transition from (3.54) to (3.55) i.e. from $\bar{\phi}$

to $\bar{u}^2$ is by no means trivial. Comparing Fig. 12 and Fig. 4 we find that although the

second derivative of $\bar{\phi}$ must be always positive in the presence of negatively charged

electrons, this no longer applies to the second derivative of $\bar{u}^2$ when the magnetic field is

present, although there is a limit on its negative values given by $\dfrac{d\bar{u}^2}{d\bar{x}^2} \rightarrow -2\bar{\omega}_{c0}^2$ as

$\bar{u} \rightarrow \infty$, the point of inflection occurring when $\bar{u} = \dfrac{\mathscr{I}}{2\bar{\omega}_{c0}^2}$. All this is directly related to

the fact that in the presence of a magnetic field we have at any given point two

competing forces, the electric force $-\dfrac{1}{2}\bar{E}$ and the magnetic force $\bar{\omega}_{c0}\bar{y}^{\cdot} = \bar{\omega}_{c0}^2 \bar{x}$, as

indicated in (2.3).

Multiplying both sides of (2.55) by $d\bar{u}^2/d\bar{x}$ and integrating with respect to $\bar{x}$ we obtain

$$\frac{1}{2}\frac{d\bar{u}^2}{d\bar{x}} = \bar{u}\frac{d\bar{u}}{d\bar{x}} = \sqrt{\mathscr{I}\,\bar{u} - \bar{\omega}_{c0}^2 \bar{u}^2 + C_1} \tag{2.56}$$

It is interesting to compare (2.56) and (A2.15); they are identical except for the presence

of an extra term $-\bar{\omega}_{c0}^2 \bar{u}^2$ due to the presence of the magnetic field. It should be noted

that this term opposes the effect of space charge expressed by the $\mathscr{I}\,\bar{u}$ term. A similar

term appears in the presence of positive ions [13], so that, as has already been pointed

out in Section 2.2, the presence of the magnetic field has the effect of increasing the

'perveance' of the system.

A second integration with respect to $\bar{x}$ now leads to the following expression

$$\frac{1}{\omega_{c0}^2}\sqrt{\mathscr{I}\,\overline{u}-\overline{\omega}_{c0}^2\overline{u}^2+C_1}-\frac{\mathscr{I}}{2\overline{\omega}_{c0}^3}\sin^{-1}\frac{2\overline{\omega}_{c0}^2\overline{u}-\mathscr{I}}{\sqrt{\mathscr{I}^2+4\overline{\omega}_{c0}^2C_1}}=\overline{x}+C_2 \qquad (2.57)$$

The above equation substantially differs from (A2.16), largely due to the presence of the

$\sin^{-1}$ function, which makes it possible for $\dfrac{d\overline{u}^2}{dx^2}$ to become negative for $\overline{u} > \mathscr{I}/2\overline{\omega}_{c0}^2$,

as shown in Fig. 3.10. This is quite a marked departure from the case of $B=0$ and is the

basis of the so-called striations observed by others [4].

The first constant of integration C_1 can be easily eliminated by nothing that $\overline{u}=1$ when

$\overline{x}=0$. Hence (2.57) reduces to:

$$\overline{x}=\frac{1}{\overline{\omega}_{c0}^2}\left\{\sqrt{\mathscr{I}\,\overline{u}-\overline{\omega}_{c0}^2\overline{u}^2+C_1}-\sqrt{\mathscr{I}\cdot\overline{\omega}_{c0}^2+C_1}\right\}-$$
$$\frac{\mathscr{I}}{2\overline{\omega}_{c0}^3}\left\{\sin^{-1}\frac{2\overline{\omega}_{c0}^2\overline{u}-\mathscr{I}}{\sqrt{\mathscr{I}^2+4\overline{\omega}_{c0}^2C_1}}-\sin^{-1}\frac{2\overline{\omega}_{c0}^2-\mathscr{I}}{\sqrt{\mathscr{I}^2+4\overline{\omega}_{c0}^2C_1}}\right\} \qquad (2.58)$$

The other constant of integration is more difficult to eliminate. In fact, following an

earlier example [2] indicated in (A2.19), we can choose a new constant which is $\overline{u}_m$, i.e.

the min/max value of the velocity $\overline{u}$, when it exists between the electrodes. Writing

$d\overline{u}^2/d\overline{x}=0$ on the LHS of (2.56) we obtain

$$0=\mathscr{I}\,\overline{u}_m-\overline{\omega}_{c0}^2\overline{u}_m^2+C_1 \qquad (2.59)$$

or

96

$$\bar{u}_m = \frac{1}{2\bar{\omega}_{c0}^2}\left[\mathscr{I} \pm \sqrt{\mathscr{I}^2 + 4\bar{\omega}_{c0}^2 C_1}\right] \tag{2.60}$$

Substituting in (2.57) we obtain

$$\bar{x} = \frac{1}{\bar{\omega}_{c0}^2}\left\{\sqrt{\mathscr{I}(u - u_m) - \bar{\omega}_{c0}^2(\bar{u}^2 - \bar{u}_m^2)} - \sqrt{\mathscr{I}(1 - \bar{u}_m) - \bar{\omega}_{c0}^2(1 - \bar{u}_m^2)}\right\}$$
$$- \frac{\mathscr{I}}{2\bar{\omega}_{c0}^2}\left\{\sin^{-1}\frac{2\bar{\omega}_{c0}^2\bar{u} - \mathscr{I}}{2\bar{\omega}_{c0}^2\bar{u}_m - \mathscr{I}} - \sin^{-1}\frac{2\bar{\omega}_{c0}^2 - \mathscr{I}}{2\bar{\omega}_{c0}^2\bar{u}_m - \mathscr{I}}\right\} \tag{2.61}$$

One might argue that in the presence of a min/max between the electrodes the effect of the constant of integration is somewhat easier to comprehend in (2.61) than (2.58).

Let us now consider some examples of the potential and velocity distribution between the electrodes. In the absence of a magnetic field we have the well known distributions shown in Fig. A4. Since in this case $\bar{\phi} = \bar{u}^2$, the two sets of distributions are identical; they are all symmetrical with a minimum situated exactly in the middle plane at $\bar{x} = 0.5$. The situation is somewhat different when the magnetic field is present. In Figs. 3.11 and 3.12 we have respectively the two function $\bar{\phi}(\bar{x})$ and $\bar{u}^2(\bar{x})$ for $t = t_{max}$ and different values of $\bar{\omega}_{c0}$. We find from Fig. 6a that as $\bar{\omega}_{c0}$ increases from zero to 1.0 (cut-off condition), the position of the potential minimum $\bar{x}_m$ shifts from the center towards the exit electrode, however the potential at the entrance electrode reaches unity for all values of $\bar{\omega}_{c0}$. The situation is dramatically different in the case of velocity distribution. Due to the presence of the magnetic field the value of $\bar{u}^2$ at the exit electrode is given by $1 - \bar{\omega}_{c0}^2$, as shown in (2.16); in fact it is zero for $\bar{\omega}_{c0} = 1$, i.e. for the cut-off condition.

Also the shift of the minimum of the $\bar{u}^2$ function away from the middle plane is much greater than in the case of the potential function. In fact it can be shown that for $\bar{\omega}_{c0} = 1$ the position of the potential minimum of the $\bar{u}^2$ function coincides with the exit electrode, so that $\bar{x}_m = \bar{x}_2 = 1$.

As another example let us consider the distribution of the velocity function $\bar{u}^2$ for different values of the injection current $\imath$ (or $\mathscr{I}$) and a fixed value of $\bar{\omega}_{c0}$, choosing $\bar{\omega}_{c0} = 0.5$ and 1.0 as lying at two ends of the range of values of the magnetic field for a conducting diode. We find that the value of the injection current has a profound effect on the shape of the velocity function $\bar{u}^2(\bar{x})$, as could be inferred from Fig. 12. Thus in the case of $\bar{\omega}_{c0} = 0.5$ the curve corresponding to zero value of the injection current exhibits a negative second derivative, whereas all the other curves shown in Fig. 6b have a positive second derivative. At the same time the position of the minimum moves towards the centre as $\mathscr{I}$ increases, although it never quite reaches it. The situation is even more interesting in the cut-off case, i.e. for $\bar{\omega}_{c0} = 1$. Now the only two curves which exhibit a min/max are those for $\imath = 0$ and $\imath = \imath_{max}$, the first having a maximum at the entrance electrode, $\bar{x} = 0$ and the second having a minimum at the exit electrode, $\bar{x} = 1$. The remaining curves exhibit neither a minimum nor a maximum point, but only an inflexion point at $\bar{u}^2 = \frac{1}{4}\mathscr{I}^2$, as indicated in Fig. 8a for $\bar{\omega}_{c0} = 1$.

It should be added that most of the curves shown in Figs. 6a, b and 11 have been obtained using time as the independent variable, as explained in Section 2.3, although

they then have been checked against the much more cumbersome expressions derived in the present Section.

2.4.1 Zero magnetic field

Let us start our investigation with the simpler case of a zero magnetic field, $B = 0$. The question of stability of electron flow in a diode, when the system is not space-charge-limited, came into prominence in the late thirties in connection with the development of multi-grid tubes, the power tetrode in particular. The problem was formulated in two famous papers by Llewellin and Llewellin & Peterson [18], where the steady state solutions given by Fay et al. [2] have been perturbed by a small a.c. injection current. The relationship between the injection conditions, and the corresponding output potential, current and velocity (all ac) is expressed by the well-known 3x3 matrix of a_{ij} coefficients. An excellent summary of the derivation of the a_{ij} coefficients is provided in Section 3b of [19]. A more detailed discussion of the stability of such solutions based on the energy considerations and also on the algebraic properties of one of the a_{ij} coefficients, viz. a_{11} is provided in Ch. 3 of [7]. As mentioned before a physically convincing 'explanation' of the source of possible instability of the system, using a minimum of mathematics, in Section 10.6 of [8].

The a_{11} coefficient of the a_{ij} matrix relates the dc injection current $\bar{J}_c$ to the ac potential difference between electrodes $\tilde{\phi}_2 - \tilde{\phi}_1$. Using our bar notation we can write:

$$\bar{\tilde{\phi}}_2 - \bar{\tilde{\phi}}_1 = \bar{a}_{11}\bar{J}_c \qquad (2.63)$$

where from [19, p. 37]

$$\begin{aligned}
\bar{a}_{11} &= -\frac{\bar{\tau}_d}{i\bar{\omega}}\frac{\bar{v}_1+\bar{v}_2}{2}\left[1-\frac{1}{3}\zeta\left(1+2\Phi_4\right)\right] \\
&= -\frac{\bar{\tau}_d}{i\bar{\omega}}\left[1-\frac{1}{3}\zeta\left(1+2\Phi_4\right)\right]
\end{aligned}$$

(2.64)

since for a short-circuited diode we have in our bar notation (see Appendix 1) the injection velocity $\bar{v}_1 = \bar{v}_2 = 1$. Here $\bar{\tau}_d$ is the steady state transit time between the electrodes and ζ is the so-called space-charge factor given by two alternative definitions:

$$\zeta = 3\left(1-\frac{\bar{\tau}_{d0}}{\bar{\tau}_d}\right) = 3\left(1-\frac{1}{\bar{\tau}_d}\right)$$

(2.65a)

$$\zeta = \frac{-J_c\bar{\tau}_d^2}{4\left(\bar{v}_1+\bar{v}_2\right)} = \frac{1}{18}\imath\bar{\tau}_d^2$$

(2.65b)

where $\bar{\tau}_{d0}$ is the value of $\bar{\tau}_d$ in the absence of space charge and $\imath = -\frac{9}{4}\bar{J}_c$ is the normalized injection current density, as defined in Appendix 1 and then used in Fig. 5. Substituting (2.65b) in (2.64) we obtain

$$\begin{aligned}
\bar{a}_{11} &= -\frac{\bar{\tau}_d}{i\bar{\omega}}\left[1-\frac{1}{3}\zeta-\frac{2}{3}\zeta\Phi_4\right] \\
&= -\frac{\bar{\tau}_d}{i\bar{\omega}}\left[\frac{1}{\bar{\tau}_d}-\frac{2}{3}\frac{\imath\bar{\tau}_d}{18}\Phi_4\right] \\
&= -\frac{\imath\bar{\tau}_d^3}{27i\bar{\omega}}\left[\frac{27}{\bar{\tau}_d^3}-\Phi_4\right]
\end{aligned}$$

(2.66)

Since for a shortcircuited diode we have $\tilde{\tilde{\phi}}_2 = \tilde{\tilde{\phi}}_1$, the l.h.s. of (2.63) is zero and we thus obtain from (2.66) the required relationship

$$\overline{a}_{11} = 0 \text{ or } A_\phi = \Phi_4, \ A_\phi = \frac{27}{i\tau_d^3} \tag{2.67}$$

where Φ_4 is given by

$$\Phi_4 = -\frac{6}{z^3}\left(2 - z - 2e^{-z} - ze^{-z}\right) \tag{2.68}$$

Thus the question of stability of the solutions has now been reduced to the investigation of (2.67). In the initial derivation of (2.64) the variable z was assumed to be purely imaginary, $z = i\omega t$, since it related directly to the initial sinusoidal perturbation of the system by adding an ac term to the dc Llewellyn – Peterson equation (2.6). Taking z to be pure real and introducing some approximations to Φ_4 the stability of solutions has already been discussed by Birdsall [7]. We decided to avoid any approximations to Φ_4 as being too dangerous, bearing in mind that in the presence of a magnetic field the equivalent of Φ_4 acquires quite a complicated form, (2.76). We have therefore adopted a more general approach by treating z as a complex variable $z = x + iy$, keeping (2.68) as it stands and simply looking for zeros of (2.67).

The real and imaginary parts of Φ_4 are respectively shown in Figs. 13 a and b. We find that in spite of its apparent algebraic complexity the function can be envisaged as a

simple combination of exponentials along the real x-axis and trigonometric oscillations in the imaginary iy -direction.

The solution of (2.67) is simplified by the fact that the l.h.s. is pure real, the values of ι and $\bar{\tau}_d^3$ directly relating to Fig. 5. Thus in order to solve (2.67) we simply plot the contours Re $\Phi_4 = A_\phi$ and Im $\Phi_4 = 0$, the points where the two sets of contours cross being the required solution.

As an example let us consider point A in Fig. 5, which represents the maximum permissible value of the injection current in a short-circuited diode given by $\iota = \iota_{max} = 8.0$, Table 2.1. For $\bar{\omega}_{co} = 0$, (2.21) acquires a much simpler form given by (see A2.8).

$$\iota = \frac{54}{\bar{\tau}_d^3}\left(\bar{\tau}_d - 1\right) \tag{2.69}$$

Solving (2.69) for $\iota = 8.0$ we obtain $\bar{\tau}_d = 1.5$; substituting for both ι and $\bar{\tau}_d$ in (2.55) we find that

$$A_\phi = \frac{27}{\iota\bar{\tau}_d^3} = 1.0000 = \Phi_4 \tag{2.70}$$

The superposition of the two sets of contours Re $\Phi_4 = 1.0$, Im $\Phi_4 = 0.0$ is shown in Fig. 14a, the corresponding positions of the zeros being indicated by circles. As was to be expected the important main zero lies at the origin of the complex z-plane, indicating

that point A represents a conditional equilibrium separating the stable and unstable regimes of the system.

In order to familiarize ourselves with our technique of testing the stability of solutions, let us briefly consider two more points, one stable (point A') and one unstable (point B). We find from (A2.8), Table 2.2 and Fig. 5 that the important parameters for the two points are given by:

Table 2.4 Parameters of Points A' and B

	$\bar{\tau}_d$	ι	$\bar{E}_1$	A_ϕ
A'	1.0981	4.0000	0.9762	5.0977
B	3.0000	4.0000	2.6667	0.2500

We can now repeat our procedure for solving (2.67) with new values of A_ϕ. Figs. 14b and c respectively show the contours of Re Φ_4 for the two values of A_ϕ given in Table 2.4 and for Im $\Phi_4 = 0.0$. Again the roots of (2.67) occur where the two sets of contours cross. We now find, as to be expected, that for point A' the main root of (2.67) lies on the negative part of the real axis, indicating that the solution is stable. Similarly, the main root of (2.67) for point B lies on the positive part of real axis, indicating that the solution is unstable.

At this point it should be clarified that the above analysis, although useful, is highly idealized. In practice an electron stream is not a homogeneous jelly, but consists of a large number of individual particles which contribute to noise, the other contributions

being random velocities and random times of emission of individual electrons [20]. This means that in practice the unstable branch A-B can never be reached, the system breaking out into relaxation oscillations, forming the basis of operation of a vircator [7]. However the idealized solutions based on (2.6) and Llewellyn - Peterson equations are useful in proving the fundamental instability of physical situations they represent. Similar comments apply when the magnetic field is present.

2.4.2 Magnetic field present

In the previous section we have considered the case of zero magnetic field as a way of introduction to our relatively straightforward method of investigating the stability of solutions. Let us now consider the more difficult case when the magnetic field is present. Fortunately considerable amount of work has been done on the extension of the Llewellyn-Peterson equations to the case of crossed-field geometries and we are going to rely heavily on the results of those investigations [21, 22]. The main difference is that the magnetic field forces us to consider the current flow in two dimensions. Consequently the usual perturbation of the steady state equation (2.6) now leads to a set of a_{ij} coefficients which form a 4x4 rather than 3x3 matrix, as they did before. Since there are no a.c. components of current or velocity at the entrance electrode, the d.c. injection current being perpendicular to the entrance electrode, (2.61) still holds, except that now $\overline{a}_{11}$ is much more elaborate than the corresponding expression in (2.64). Using our bar notation we obtain from [21, p. 82]:

$$\overline{a}_{11} = -\frac{\overline{x}_i'}{i\overline{\omega}\,\overline{\omega}_{c0}}s_{\theta c} - \frac{\overline{x}_1''}{i\overline{\omega}\,\overline{\omega}_{c0}^2}\left(1-c_{\theta c}\right) - \frac{\overline{J}_c}{2i\overline{\omega}\,\overline{\omega}_c}\left[\frac{s_{\theta c}}{\overline{\omega}_c} + \frac{\theta_c}{\overline{\omega}_c\left(\overline{\omega}_c^2/\overline{\omega}^2 - 1\right)}\right] + \frac{\overline{J}_c}{2\left(\overline{\omega}_c^2 - \overline{\omega}^2\right)^2}\left(Q+P\right)$$

where

$$P = 1 - i\frac{\overline{\omega}}{\overline{\omega}_c} s_{\theta c} e^{-i\theta} - c_{\theta c} e^{-i\theta} \qquad (2.72)$$

$$Q = 1 - i\frac{\overline{\omega}_c}{\overline{\omega}} s_{\theta c} e^{-i\theta} - c_{\theta c} e^{-i\theta}$$

and

$$\theta = \overline{\omega}\overline{\tau}_d, \ \theta_c = \overline{\omega}_{c0}\overline{\tau}_d, \ s_{\theta c} = \sin \overline{\omega}_{c0}\overline{\tau}_d, \ c_{\theta c} = \cos \overline{\omega}_{c0}\overline{\tau}_d \qquad (2.73)$$

The new expression for $\overline{a}_{11}$ looks quite formidable, fortunately it can be reduced to a more manageable form for our particular task of stability investigations.

In (2.71) the coefficient $\overline{a}_{11}$ is expressed in terms of the initial velocity $\overline{x}_1^{\cdot}$ and initial acceleration $\overline{x}_1^{\cdot\cdot}$. It is more convenient for our purpose to express it in terms of interelectrode distance $\overline{x}_d$ which in the bar notation is equal to unity by definition (see (A1.1) in Appendix 1). Thus we can combine the first four terms on the r.h.s. of (2.71) and write with the help of (2.7):

$$\overline{a}_{11} = -\frac{\overline{x}_d}{i\overline{\omega}} - \frac{i\theta \overline{J}_c}{2(i\overline{\omega})^2 (\overline{\omega}_c^2 - \overline{\omega}^2)} + \frac{\overline{J}_c}{2(\overline{\omega}_c^2 - \overline{\omega}^2)^2}(Q+P) \qquad (2.74)$$

where $\bar{x}_d = 1$. Now the last two terms of (2.74) can be combined together. Putting

$\bar{J}_c = -\dfrac{4}{9}\iota$, as indicated in (A1.2) and writing $-\bar{\omega}^2\bar{\tau}_d^2 = (i\bar{\omega}\bar{\tau}_d)^2 = z^2$ we obtain from

(2.74)

$$\begin{aligned}
\bar{a}_{11} &= -\frac{\bar{x}_d}{i\bar{\omega}} + \frac{2\iota}{9}\left\{ \frac{i\omega\bar{\tau}_d}{(i\bar{\omega})^2\left(\bar{\omega}_c^2 + (i\bar{\omega})^2\right)} - \frac{1}{\left(\bar{\omega}_c^2 + (i\bar{\omega})^2\right)^2}(Q+P) \right\} \\
&= -\frac{1}{i\bar{\omega}} + \frac{2\iota\bar{\tau}_d^4}{9}\left\{ \frac{z}{z^2\left(\theta_c^2 + z^2\right)} - \frac{z}{\left(\theta_c^2 + z^2\right)^2}(Q+P) \right\} \\
&= -\frac{1}{i\bar{\omega}} + \frac{2\iota\bar{\tau}_d^3}{27i\bar{\omega}}\frac{6}{\left(\theta_c^2 + z^2\right)}\left\{ \left(\theta_c^2 + z^2\right) - z(Q+P) \right\} \\
&= -\frac{1}{i\bar{\omega}} + \frac{2\iota\bar{\tau}_d^3}{27i\bar{\omega}}\Phi_{4c} \\
&= \frac{\iota\bar{\tau}_d^3}{27i\bar{\omega}}\left(\frac{27}{\iota\bar{\tau}_d^3} - \Phi_{4c} \right)
\end{aligned}$$

(2.75)

where

$$\Phi_{4c} = -\frac{6}{\left(z^2 + \theta_c^2\right)^2}\left\{ 2z - \left(z^2 + \theta_c^2\right) - \left(\frac{z^2}{\theta_c} - \theta_c\right)\sin\theta_c\, e^{-z} - 2z\cos\theta_c\, e^{-z} \right\} \qquad (2.76)$$

The main difference between (2.76) and (2.68) is that Φ_{4c} contains $\theta_c = \bar{\omega}_{c0}\bar{\tau}_d$, where

$\bar{\omega}_{c0}$ refers to the strength the magnetic field as defined in (A1.1) of Appendix 1. Figs.

17a and b respectively show the real and imaginary part of Φ_{4c} for $\bar{\omega}_{c0} = 0.8$. Strangely

enough in spite of the apparent algebraic complexity of (2.76), the difference in the

appearance of the corresponding surfaces in Figs. 17a, b and 13a, b is not that great. It

should be added that, as was to be expected $\Phi_{4c} \to \Phi_4$ as $\theta_c \to 0$. Since the crossed-field diode we are considering is short circuited, as indicated in Fig. 3, the l.h.s. of (2.63) is again zero, leading to

$$\bar{a}_{11} = 0 \text{ or } A_c = \Phi_{4c}, \ A_c = \frac{27}{i\bar{\tau}_d^3} \tag{2.77}$$

which is the equivalent of (2.67) when the magnetic field is present.

The real and imaginary parts of Φ_{4c} are respectively shown in Figs. 15a and b for $\bar{\omega}_{c0} = 0.8$. It is interesting to note that in spite of the algebraic diversity of (2.68) and (2.76), corresponding surfaces representing their real and imaginary parts are remarkably similar, as can be seen from Figs. 13a, b and 15a, b.

In order to obtain the roots of (2.77) for the three points A, A' and B and for different values of $\bar{\omega}_{c0}$, we follow the same procedure as before, except that instead of using Φ_4 we now use Φ_{4c}, as indicated in (2.77), the corresponding values of i and $\bar{\tau}_d$ being obtained from (2.21), (2.22) and Tables 2.1 and 2.2. The results of our computations are shown respectively in Figs. 16a-c. In Fig. 16a we have the roots of (2.76) for point A and for six different values of the magnetic field, including $\bar{\omega}_{c0} = 0$. We find that the main root firmly remains at the origin, the solution for $i = i_{max}$ being conditionally stable, irrespective of the corresponding values of the magnetic field.

In the case of point A' which is situated on the lower branch of the curves shown in Fig. 5, the main root is always placed on the negative part of the x-axis, as shown in Fig. 16b,

whatever the value of the magnetic field. The only exception is the limiting case $\bar{\bar{\omega}}_{c0} = 1$, when the three points coalesce, the corresponding root appearing at the origin.

Finally the main roots of (2.77) for point B are all placed on the positive part of real axis whatever the value of the magnetic field, the corresponding solutions being fundamentally unstable. The only exception again is the 'cut-off' condition when $\bar{\bar{\omega}}_{c0} = 1$; now the A'-A-B loops of Fig. 5 collapse to a cusp, the solution becoming singular. It should be added that the A-B branch of each curve is the equivalent of the well-known 'overlap' solution fully discussed for $\bar{\bar{\omega}}_{c0} = 0$ elsewhere [2,7].

The above results extend the stability investigations to a conducting crossed-field diode and thus confirm the validity of the assumptions made in a recent publication [23, special issue on High-Power Microwave Generation] which covered the results reported in Section 2.3. The stability investigations, Section 2.5, have been presented in a poster session at the IEEE Int. Conf. IVEC2002 [24]. It should be added that the method of stability investigations described above is more general than it would appear from (2.67) or (2.77), since it is not limited to a short-circuited diode. In the presence of a load $\bar{a}_{11} \neq 0$ and (2.63) can then be suitably adjusted to allow for $\tilde{\bar{\phi}}_2 - \tilde{\bar{\phi}}_1 \neq 0$.

2.5 Stability considerations

In Section 2.3 we have assumed that some solution of (2.6) are stable or conditionally stable and that other solutions are not. We will now attempt to prove that this indeed is the case. It is necessary for us to do so, because the only existing proofs apply to the simpler case when the magnetic field is not present [7, 8].

The problem of stability, or lack of it, has a long history. It all started with the question of stability of planetary orbits, possibly first raised by Newton, and in greater detail by Kepler. It was then defined with great precision by Poinearé in his magnum opus on celestial mechanics [14]. Poinearé also indicated how to treat stability in more general systems than those based on particle orbits. Almost at the same time Liapunov wrote his seminal thesis, now available in English [15], on the general approach to the question of stability in a set of equations of the form

$$\frac{dX_i}{dt} = X_i, \; i = 1, \; \ldots\ldots \; \text{n} \tag{2.62}$$

It is interesting to note that in the work on chaos, where the question of stability is of crucial importance, it is Liapunov approach in the form of Liapunov exponentials which seems to prevail [16]. It may not be out of place to repeat here a quotation from one of the best textbooks on classical mechanics [17]: 'the general subject of stability of motion [of a system] is today a very active field of investigation, often using sophisticated mathematical tools....' I am sure the author must have had TAKOMAK and plasma physics in mind when he was writing it. By contrast, in our investigations we are going to use the simplest mathematics available. In many cases the problem of stability can be formulated as a small perturbation of the system which may well take the form of a

dispersion equation. The analysis of the (complex) roots of the perturbed system then gives us some idea whether the system is stable or unstable. It is this approach we are going to adopt in our investigations.

Conclusions – part 2

A plane magnetic diode has been used as a simplified model of the effect that an axial magnetic field would have on the operation of an axial vircator. Having discussed in some detail the electron trajectories, we were able to indicate a hitherto overlooked solution reminiscent of a virtual-cathode distribution common in the absence of a magnetic field. However, due to the presence of the magnetic field, $\overline{u}^2 = 0$ *does not* imply $\overline{\phi} = 0$ and the 'vircator' effect is weakened. In fact when the magnetic field reaches its near cut-off value, $\overline{\omega}_{c0} \rightarrow 0$, the point $\overline{u}^2 = 0$ moves to the exit electrode, where the potential is fixed, $\overline{\phi} = 1$. This must suppress vircator oscillations altogether, an effect which has been observed in practice. A further increase of the magnetic field beyond its cut-off value would stop the current flow altogether.

References – part 2.

1. W.Jiang, K.Woolverton, J.Dickens and M.Kristiansen, High power microwave generation by a coaxial virtual cathode oscillator, IEEE Trans. Plasma Science vol 27, No. 5, 1999, pp26 – 30.

2. C. E. Fay, A. L. Samuel and W. Shockley, On the theory of space charge between parallel plane electrodes, BSTJ vol 17, 1938, pp. 49 – 79.

3. E. Okress, (Ed.), *Crossed-field Microwave Devices*, vols. 1 and 2, Academic Press, New York 1961.

4. L. Page and I. Adams, Jr., Space charge in plane magnetron, Phys, Rev. vol 69, 1946, pp. 492 – 494.

5. J. C. Slater, *Microwave Electronics*, Van Nostrand, New York 1950; Section 13.6.

6. Y. Y. Lau, P. J. Christenson and D. Chernin, Limiting current in a crossed-field gap, Phys. Fluids B vol. 5, 1993, pp. 4486 – 4488.

7. C. K. Birdsall and W. B. Bridges, *Electron Dynamics of Diode Regions*, Academic Press, New York 1966; Chapters 2 and 3.

8. K. R. Spangenberg, *Vacuum Tubes*, McGraw-Hill, New York 1948; section 10.6, p. 260.

9. X. Chen, P. A. Lindsay and J. Zhang, Chaos and oscillations in a loaded plasma-filled diode, IEEE Trans. Plasma Science vol 28, No 3, June 2000, pp. 462-471.

10. V. L. Granatstein and I. Alexeff, (Ed.), 'High-Power Microwave Sources', Artech House, Boston 1987; Chapter 1, B. Levush and A. T. Drobot, p. 21 and Chapter 13, D. J. Sullivan, J. E. Walsh and E. A. Coutsias, pp. 441-467.

11. R. B. Miller, 'An Introduction to the Physics of Intense Charged Particle Beams', Plenum Press NY 1982; Section 3.3.

12. R. J. Barker and E. Schamiloglu, 'High-Power Microwave Sources and Technologies', IEEE Press NY 2001, pp. 465-469.

13. P. A. Lindsay, X. Chen, J. Watkins and J. Zhang, Controlling chaos in plasma-filled diodes, Grant No: F49620-97-1-0035, Final Report, February 2000.

14. H. Poincaré, Les Méthods Nonvelles de la Méchanique Céleste, Gauthier-Villars, Paris 1892 (an English translation is being prepared).

15. A. M. Liapunov, The General Problem of the Stability of Motion (English translation), Tayler & Francis, London 1992.

16. R. C. Hilborn, Chaos and Nonlinear Dynamics, Oxford U. Press, Oxford 1994.

17. H. Goldstein, Classical Mechanics, 2nd Ed., Addison-Wesley, Reading MA, 1980.

18. F. B. Llewellyn, Operation of ultra-high frequency tubes, Bell System Tech. J., vol 14, 1935, pp. 632-665; F. B. Llewellyn and L. C. Peterson, Vacuum tube networks, Proc. IRE, vol. 32, 1944, pp. 144-166.

19. W. J. Kleen, Electronics of Microwave Tubes, Academic Press, New York 1958.

20. V. Petridis and P. A. Lindsay, New formulation of noise in collision-free systems III, Int. J. Electronics vol. 42, 1977, pp. 313-338.

21. T. van Duzer, Transformation of fluctuations along accelerating crossed-field beams, IRE Trans. Electron Devices, vol. ED-8, 1961, pp. 78-86.

22. M. A. Pollack, Noise transport in the crossed-field diode, Electron Research Lab., U. of California, Berkeley. CA; Institute of Engineering Research, Series No. 60, Issue No. 485.

23. P. A. Lindsay, W. K. Toh and X. Chen, The influence of an axial magnetic field on the performance of a coaxial vircator, IEE Trans. Plasma Science, vol. 30, 2002, pp. 1186-1195.

24. P. A. Lindsay, W. K. Toh and X. Chen, The influence of the magnetic field on the problem of stability in a crossed-field diode, Proceedings IEEE Int. Conf. IVEC 2002, April 23-25, 2002, Monterey, CA, p. 155.
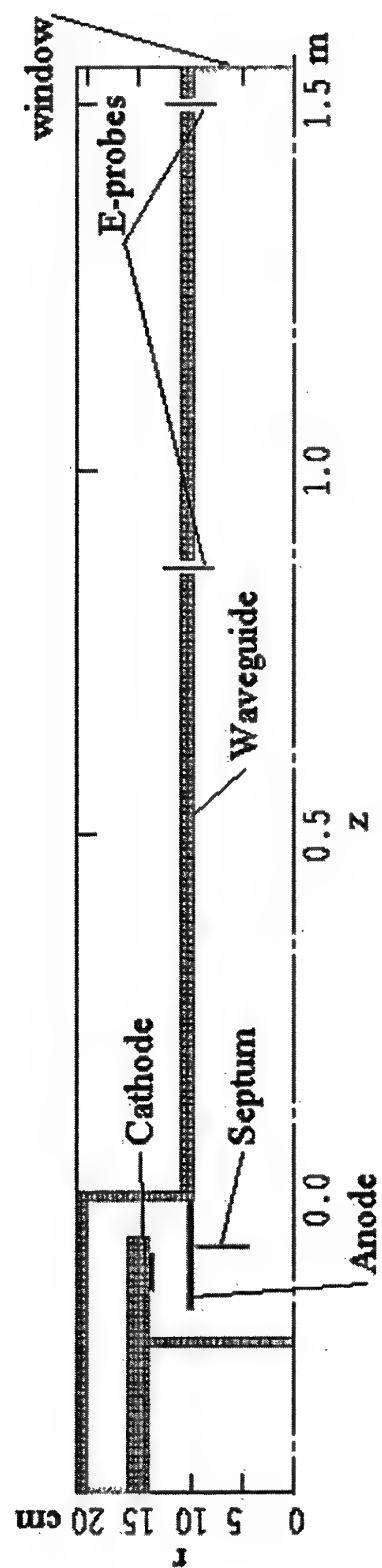
Figures – part 2

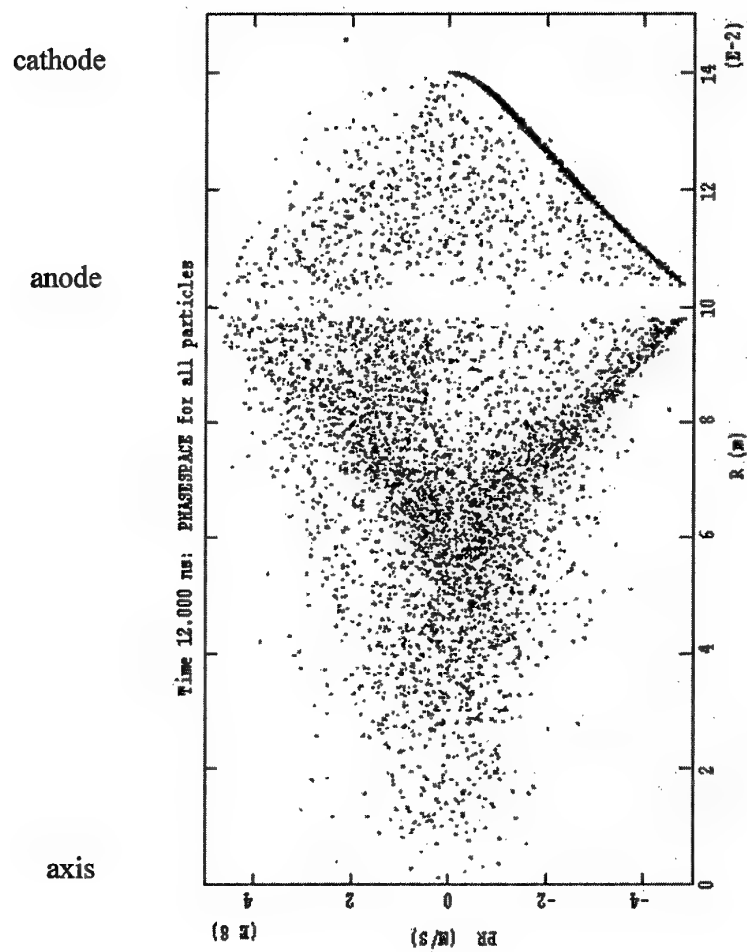Figure 1 Cross-section of a typical coaxial vircator.

Figure 2 Radial electron velocity v_r in the middle plane of the anode as a function of radius r.
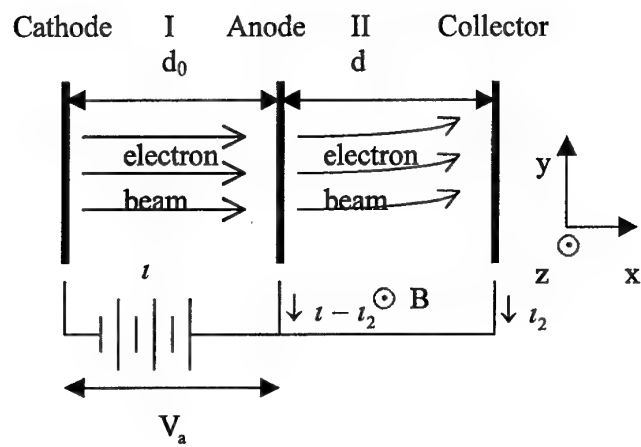
Figure 3 The model consisting of a space-charge limited diode I followed by a short-circuited crossed-field diode II.
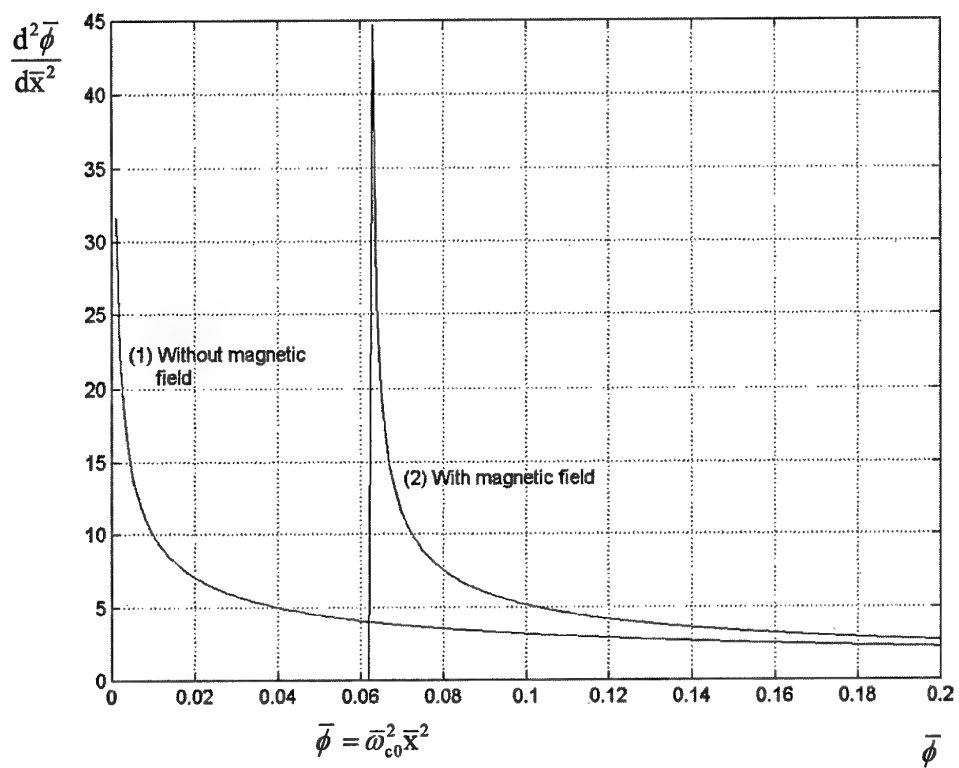
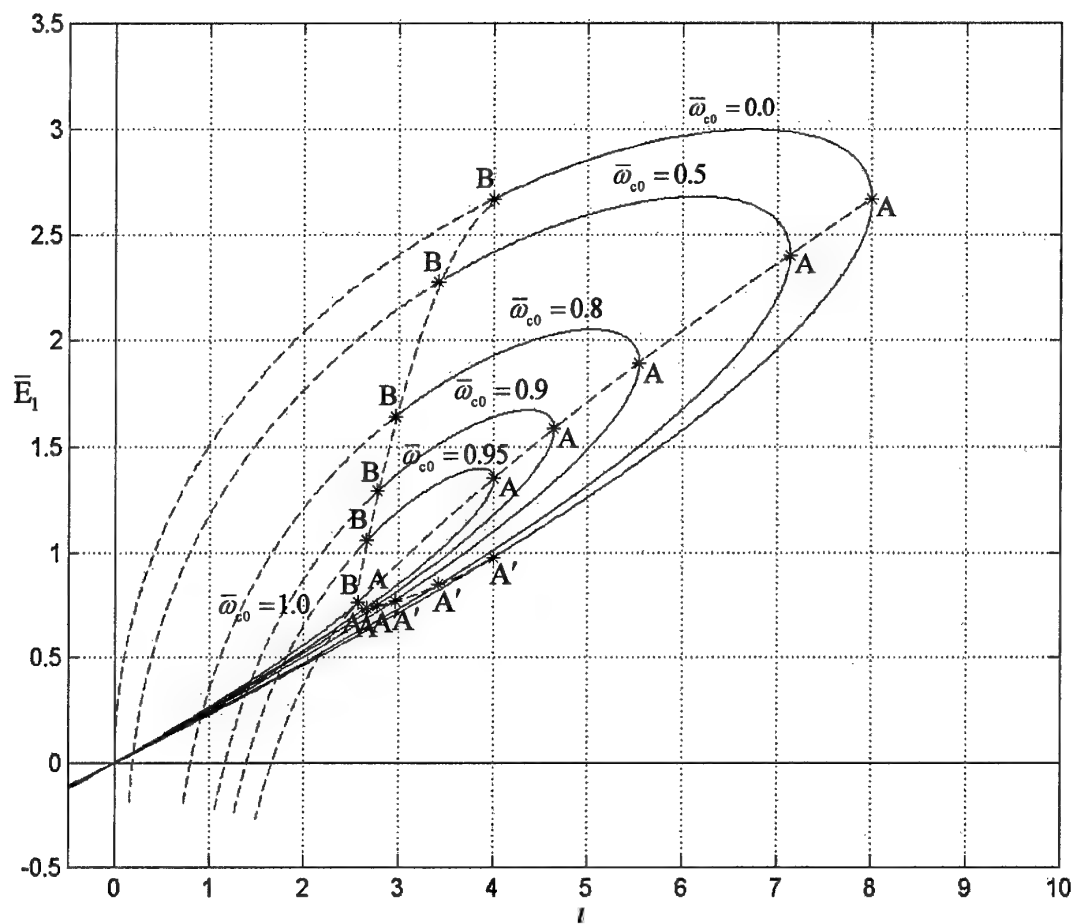Figure 4 Poisson equation without (1) and with (2) the magnetic field B expressed in terms of $\bar{\omega}_{c0}$.

Figure 5 The electric field at the entrance electrode $\bar{E}_1$ as a function of the injection current ι for different values of the magnetic field expressed by $\bar{\omega}_{c0}$.
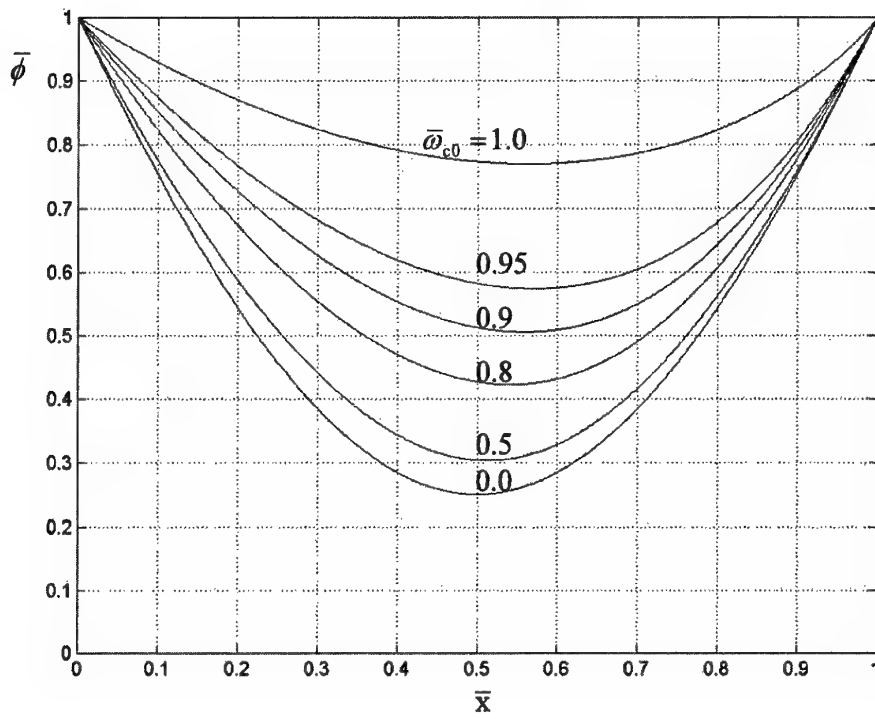
Figure 6a Potential distribution $\bar{\phi} = \bar{\phi}\left(\bar{x}\right)$ for $\iota = \iota_{max}$ and different values of $\bar{\omega}_{c0}$.
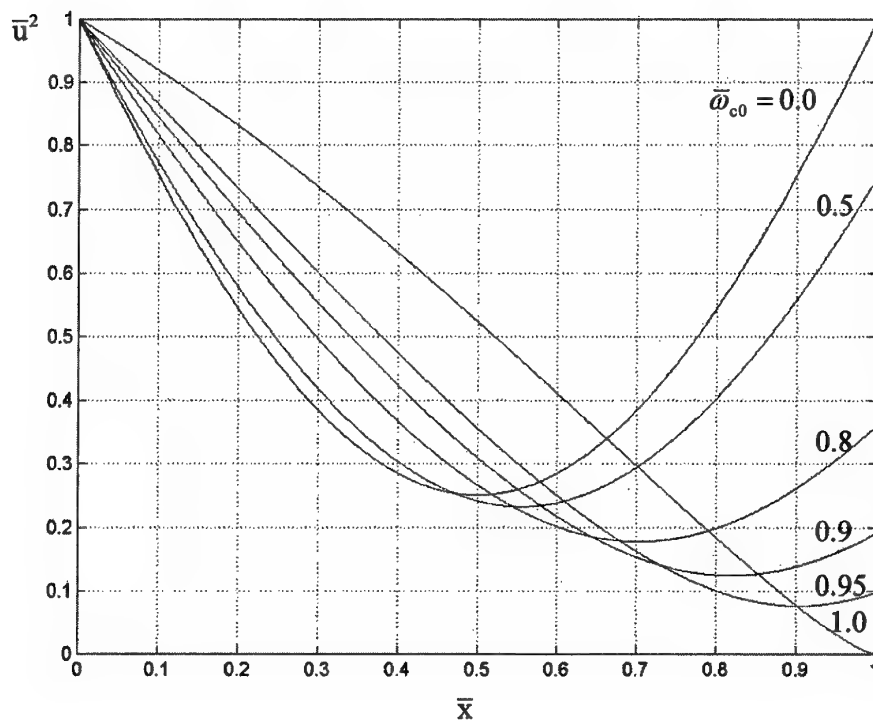
Figure 6b Velocity distribution $\bar{u}^2 = \bar{u}^2\left(\bar{x}\right)$ for $\iota = \iota_{max}$ and different values of $\bar{\omega}_{c0}$.

Figure 7 Electron trajectories for $\bar{\omega}_{c0} = 0.5$ and several values of the injection current ι.

Figure 8a A possible distribution of current for $\iota > \iota_{max}$.

Figure 8b Electron trajectories for $\bar{\omega}_{c0} = 0.5$ and three different values of the injection current ι.

Figure 9 Four critical $\bar{\phi} = \bar{u}^2$ distributions for $\bar{\omega}_{c0} = 0$.

Figure 10a Four critical velocity distributions for $\bar{\omega}_{c0} = 0.5$.

Figure 10b Four critical potential distributions for $\bar{\omega}_{c0} = 0.5$.

Figure 11a The dependence of the velocity function $\bar{u}^2\left(\bar{x}\right)$ on the injection current ι for $\bar{\omega}_{c0} = 0.5$.

Figure 11b The dependence of the velocity function $\bar{u}^2\left(\bar{x}\right)$ on the injection current ι for $\bar{\omega}_{c0} = 1.0$.

Figure 12 Following (2.48): the second derivative $d^2\bar{u}^2/d\bar{x}^2$ as a function of $\bar{u}$.

Figure 13a Real part of Φ_4 as a function of (x,y).

Figure 13b Imaginary part of Φ_4 as a function of (x,y).

Figure 14a Contours of Re $\Phi_4 = A_\phi$ (full line) and Im $\Phi_4 = 0$ (broken line) for point A; roots of (2.67) are marked by circles.

Figure 14b Contours of Re $\Phi_4 = A_\phi$ (full line) and Im $\Phi_4 = 0$ (broken line) for point A'; roots of (2.67) are marked by circles.

Figure 14c Contours of Re $\Phi_4 = A_\phi$ (full line) and Im $\Phi_4 = 0$ (broken line) for point B; roots of (2.67) are marked by circles.

Figure 15a Real part of Φ_{4c} as a function of (x,y) for $\bar{\omega}_{c0} = 0.8$.

Figure 15b Imaginary part of Φ_{4c} as a function of (x,y) for $\bar{\omega}_{c0} = 0.8$.

Figure 16a Point A: roots of (2.76) for six different values of the magnetic field (conditionally stable solutions).

Figure 16b Point A': roots of (2.76) for six different values of the magnetic field (stable solutions).

Figure 16c Point B: roots of (2.76) for six different values of the magnetic field (unstable solutions).

Figure 1 Cross-section of a typical coaxial vircator.

Figure 2 Radial electron velocity v_r in the middle plane of the anode as a function of radius r.

Figure 3 The model consisting of a space-charge limited diode I followed by a short-circuited crossed-field diode II.

Figure 4 Poisson equation without (1) and with (2) the magnetic field B *expressed in terms of* $\bar{\omega}_{c0}$.

Figure 5 The electric field at the entrance electrode $\overline{\mathrm{E}}_1$ as a function of the injection current $\imath$ for different values of the magnetic field expressed by $\overline{\omega}_{c0}$.

Figure 6a Potential distribution $\overline{\phi} = \overline{\phi}\left(\overline{x}\right)$ for $\iota = \iota_{max}$ and different values of $\overline{\omega}_{c0}$.

Figure 6b Velocity distribution $\overline{u}^2 = \overline{u}^2\left(\overline{x}\right)$ *for* $\imath = \imath_{max}$ *and different values of* $\overline{\omega}_{c0}$.

Figure 7 Electron trajectories for $\bar{\omega}_{c0} = 0.5$ and several values of the injection current ι.

Figure 8a A possible distribution of current for $\iota > \iota_{max}$.

Figure 8b Electron trajectories for $\overline{\omega}_{c0} = 0.5$ *and three different values of the injection current* $\imath$.

Figure 9 Four critical $\bar{\phi} = \bar{u}^2$ *distributions for* $\bar{\omega}_{c0} = 0$.

Figure 10a Four critical velocity distributions for $\bar{\bar{\omega}}_{c0} = 0.5$.

Figure 10b Four critical potential distributions for $\bar{\omega}_{c0} = 0.5$.

Figure 11a The dependence of the velocity function $\overline{u}^2(\overline{x})$ on the injection current ι for $\overline{\omega}_{c0} = 0.5$.

Figure 11b The dependence of the velocity function $\overline{u}^2\left(\overline{x}\right)$ *on the injection current* $\imath$ *for* $\overline{\omega}_{c0} = 1.0$.

Figure 12 Following (2.48): the second derivative $\mathrm{d}^2\overline{\mathrm{u}}^2/\mathrm{d}\overline{\mathrm{x}}^2$ *as a function of* $\overline{\mathrm{u}}$.

Figure 13a Real part of Φ_4 *as a function of (x,y).*
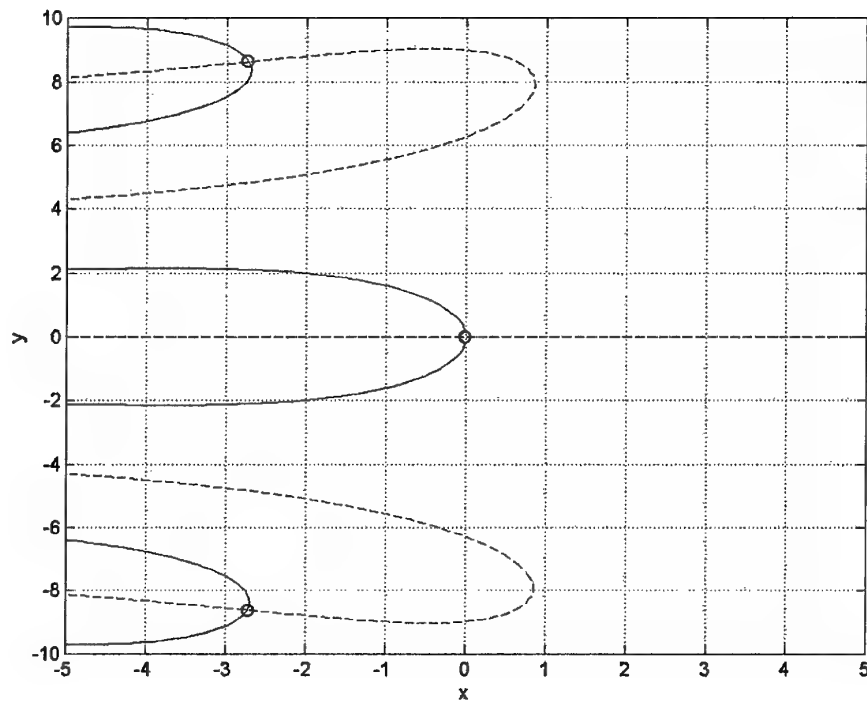
Figure 13b Imaginary part of Φ_4 *as a function of (x,y).*

Figure 14a Contours of Re $\Phi_4 = A_\phi$ *(full line) and* Im $\Phi_4 = 0$ *(broken line) for point A; roots of*

(2.67) are marked by circles.

Figure 14b Contours of Re $\Phi_4 = A_\phi$ *(full line) and Im* $\Phi_4 = 0$ *(broken line) for point A'; roots of (2.67) are marked by circles.*

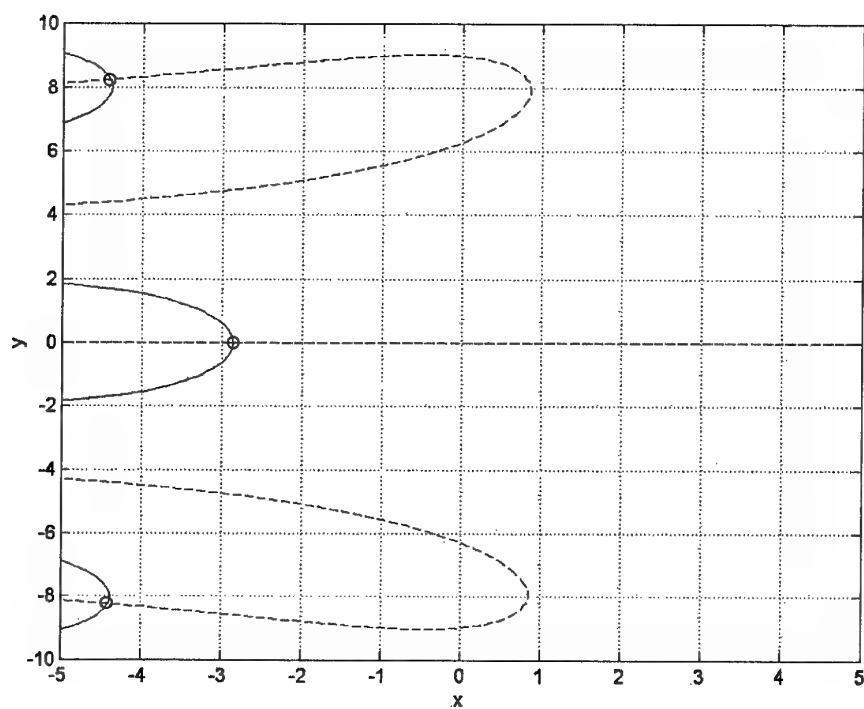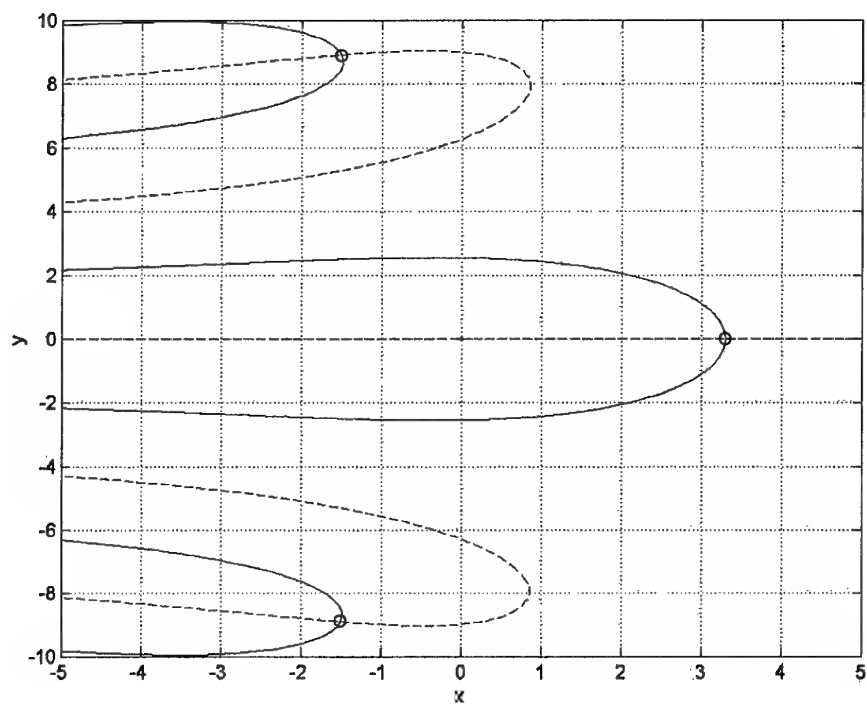*Figure 14c Contours of Re* $\Phi_4 = A_\phi$ *(full line) and Im* $\Phi_4 = 0$ *(broken line) for point B; roots of (2.67) are marked by circles.*
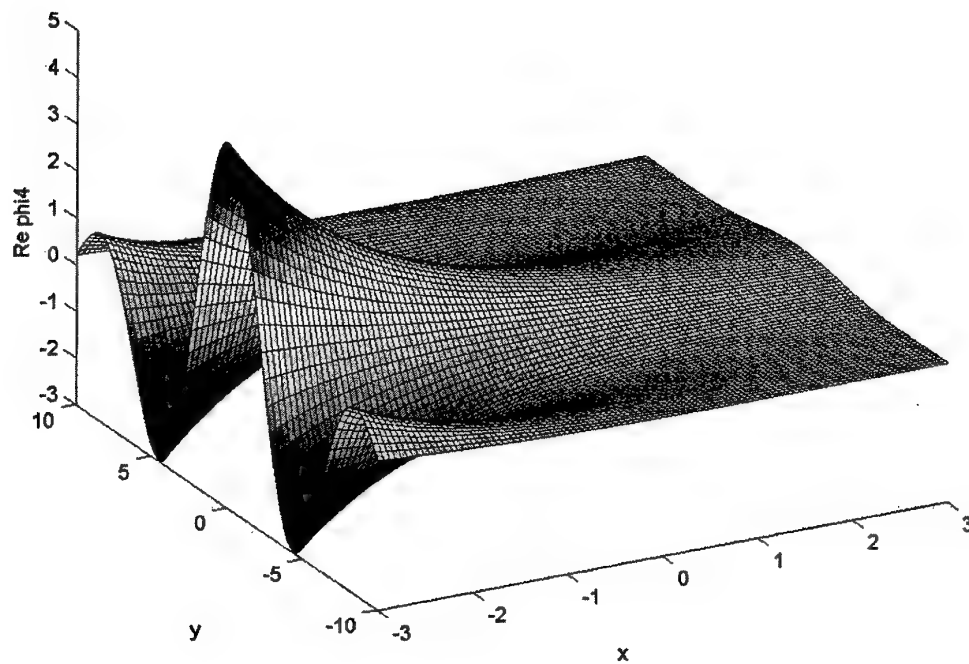
Figure 15a Real part of Φ_{4c} as a function of (x,y) for $\bar{\omega}_{c0} = 0.8$.
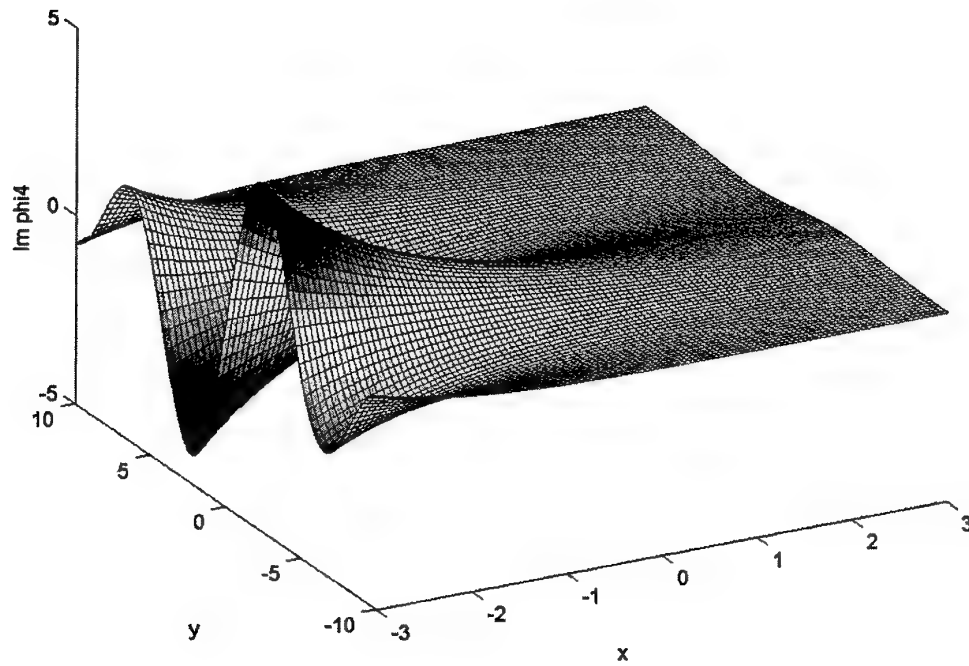
Figure 15b Imaginary part of Φ_{4c} *as a function of (x,y) for* $\bar{\omega}_{c0} = 0.8$.
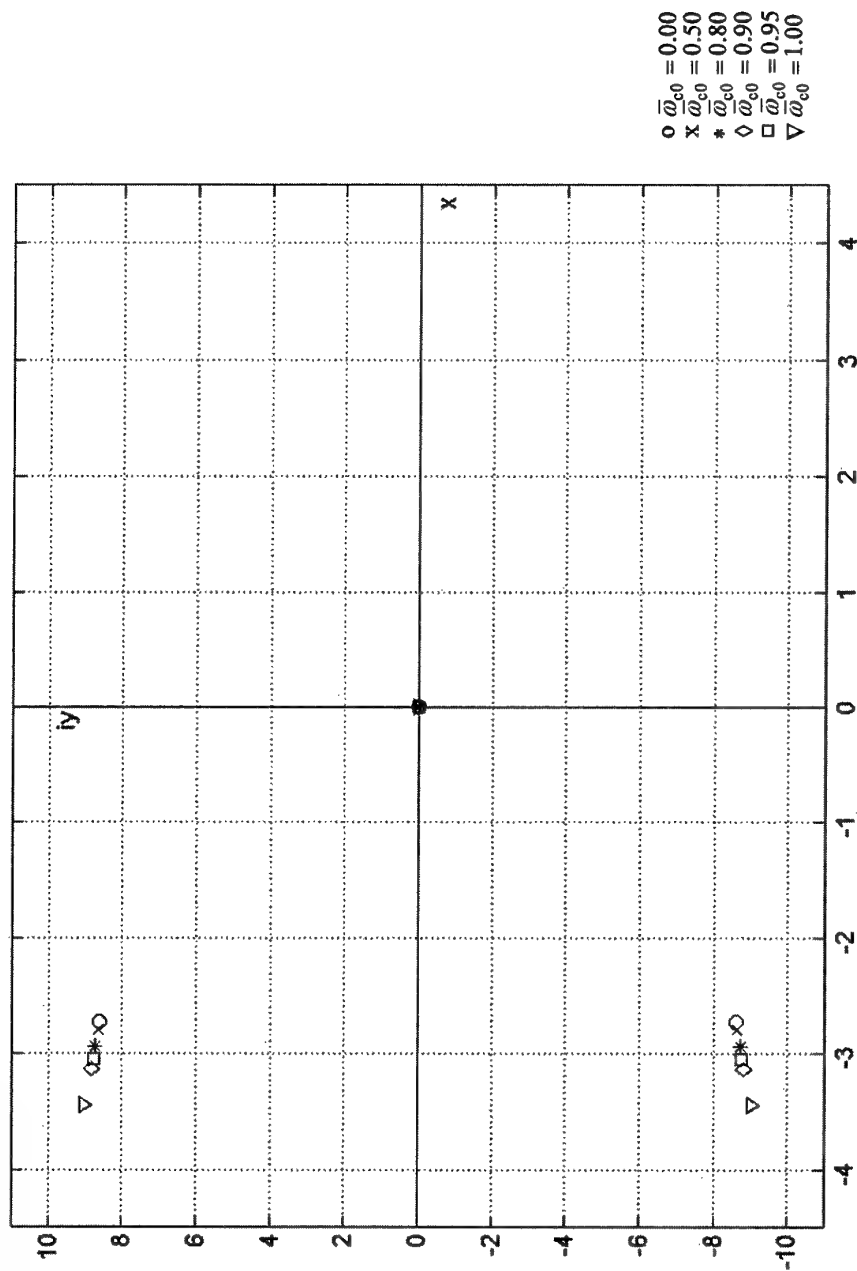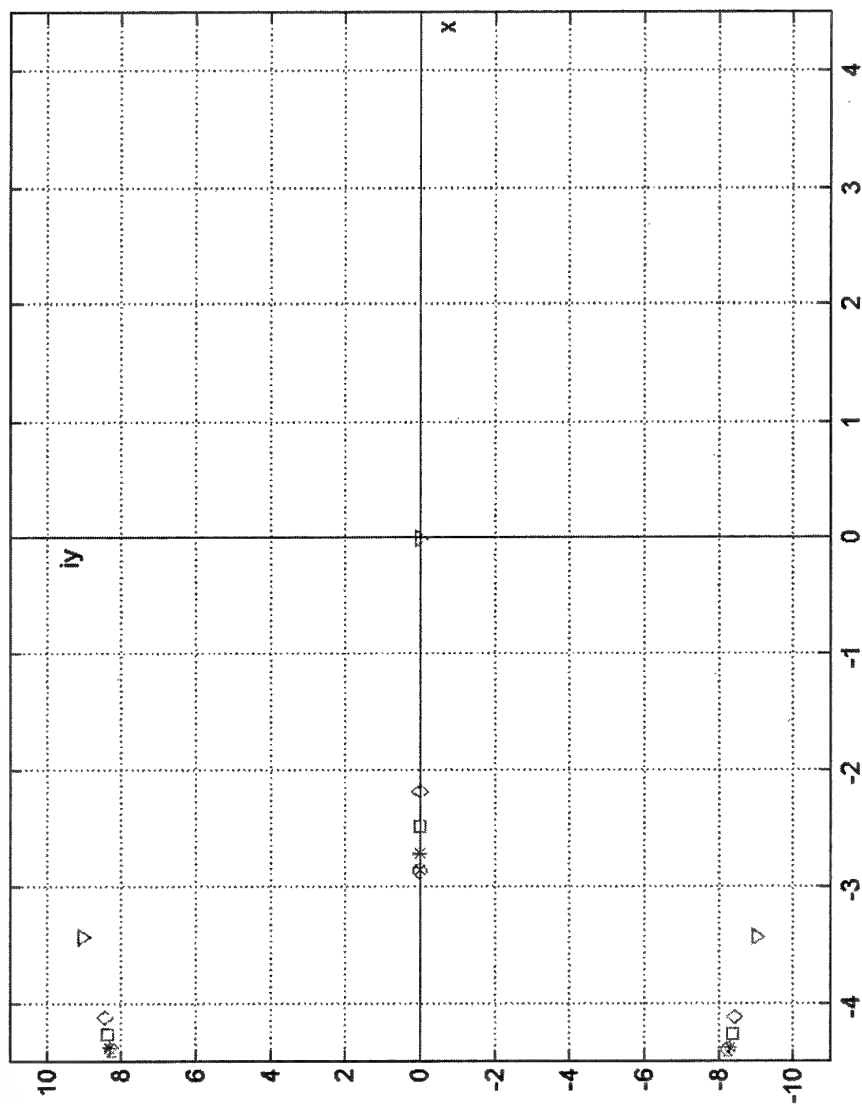
Figure 16a Point A: roots of (2.76) for six different values of the magnetic field (conditionally stable solutions).

Figure 16b Point A': roots of (2.76) for six different values of the magnetic field (stable solutions).
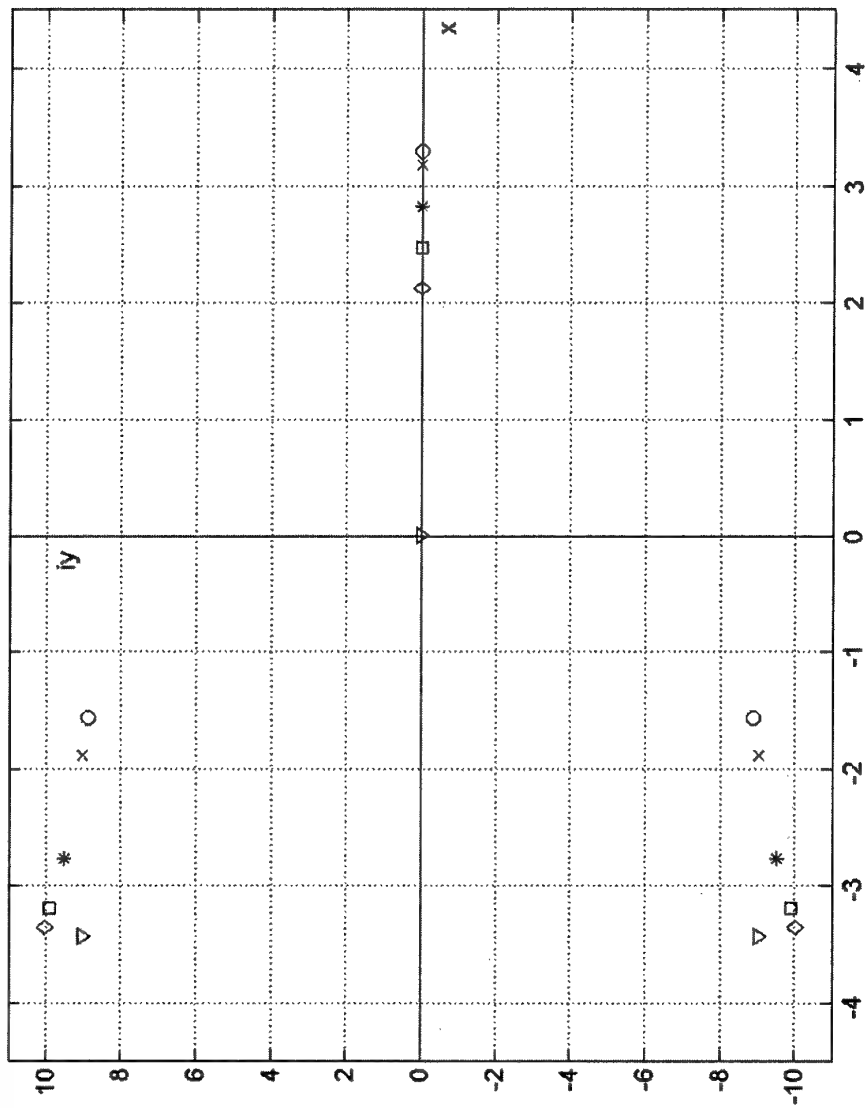
Figure 16c Point B: roots of (2.76) for six different values of the magnetic field (unstable solutions).

Future work

One area which in our opinion requires further investigation is the mode structure of the microwave output. Since the output waveguide is heavily overmoded and the frequency spectrum of the microwave pulse frequently shows the presence of additional resonances, a series of careful measurements using suitable waveguide probes would be required.

As far as the more general area of improving the performance of the vircator is concerned, then we have two suggestions to make:

1. In our opinion it is essential to pursue the investigations of the electron cloud formation in the important interaction region where the virtual cathode is being formed. This task is substantially facilitated by the technique of 'moving pictures' as developed by one of us (X. Chen) and described in the report.

2. Associated with this we feel it is necessary to investigate even more closely the design of the space still inside the anode drum, but nearer to the flange. It is there that a cleverly designed septum should catch stray electrons and thus improve the power output and electronic efficiency of the device. All this would invariably have a beneficial effect on improving the appearance of the frequency spectrum.

Appendix 1. 'Bar' notation

In order to reduce the number of independent variables it is convenient to use the following notation based on some earlier work [1].

$$\bar{x} = x/d, \quad \bar{t} = t/t_1, \quad \bar{v} = v/v_1, \quad \bar{\phi} = \phi/\phi_1,$$
$$\bar{\rho} = (d^2/\varepsilon_0\phi_1)\rho, \quad \bar{E} = (d/\phi_1)E = -\partial\bar{x}/\partial\bar{\phi} \qquad (A1.1)$$
$$\bar{J}_c = \bar{\rho}\bar{v} = (d^2/\varepsilon_0\phi_1 v_1)J_c < 0, \quad \bar{\omega}_{c0} = t_1\omega_{c0}$$

Here

d	–	separation of the electrodes
$t_1 = d/v_1$	–	electron transit time in the absence of fields
$\omega_{c0} = (e/m_0)B$	–	electron cyclotron (angular) frequency
B	–	axial magnetic field

Thus following (A1.1) we always have:

$\bar{\phi}_1 = 1$, $\bar{v}_1 = (d\bar{x}/d\bar{t})_1 = \bar{x}_1' = 1$ at the entrance electrode, $\bar{x}_1 = 0$ and $\bar{x}_2 = 1$ at the exit electrode. In addition for a short-circuited diode $\bar{\phi}_2 = 1$ at the exit electrode. It is also convenient to express the injection current in terms of a reduced current 'iota', where

$$\iota = (-J_c)/(-J_{spl}) = -\frac{9}{4}\bar{J}_c \qquad (A1.2)$$

and

$$-J_{spl} = \frac{4}{9} \varepsilon_0 \sqrt{\frac{2e}{m_0}} \frac{\phi_1^{3/2}}{d^2} = \frac{4}{9} \varepsilon_0 \frac{\phi_1 v_1}{d^2} \qquad (A1.3)$$

is the current density in an equivalent space-charged limited diode [1].

For purely algebraic reasons we have also introduced a 'curly' capital I defined as

$$\mathscr{I} = \frac{4}{9} \iota \qquad (A1.4)$$

This simplifies the notation in some cases.

Appendix 2. Summary of results for a short circuited diode when B=0

As a check on the analytical expressions derived in the presence of a magnetic field, B≠0, it is desirable to compare them with similar, but well-known expressions, for the case of B=0 [1]. The corresponding expressions are summarised here for the convenience of the reader. As is well known in the absence of a magnetic field the equation of motion and the energy balance equation acquire a simplified form; thus putting $\bar{\omega}_{c0} = 0$ in (3.2.1) and (3.2.13) we obtain

$$\bar{x}^{\cdot\cdot} = \bar{x}\frac{d\bar{x}^{\cdot}}{dx} = -\frac{1}{2}\bar{E} \qquad \text{Equation of motion} \qquad (A2.1)$$

$$\bar{x}^{\cdot^2} = \bar{\phi} \qquad \text{Energy balance} \qquad (A2.2)$$

However the Poisson equation (3.3.1) and the continuity equation (3.3.2) remain unaltered.

A2.1 Time-dependent solutions

Let us repeat the definition of the current density (3.2.3) by writing

$$\bar{J}_c = \bar{\rho}\bar{x}^{\cdot} = \frac{d\bar{E}}{d\bar{x}}\bar{x}^{\cdot} = \bar{E}^{\cdot} \qquad (A2.3)$$

Differentiating (A2.1) with respect to $\bar{t}$ and substituting from (A2.3) we obtain

$$\bar{x}''' = -\frac{1}{2}\bar{E}' = -\frac{1}{2}\bar{J}_c = \text{const} \tag{A2.4}$$

which is the steady-state part of the Llewellyn-Peterson equation [2]. The solution of (A2.4) is quite simple and is given by

$$\bar{x} = \bar{\tau} - \frac{1}{4}\bar{E}_1\bar{\tau}^2 + \frac{\iota}{27}\bar{\tau}^3 \tag{A2.5}$$

$$\bar{x}' = 1 - \frac{1}{2}\bar{E}_1\bar{\tau} + \frac{\iota}{9}\bar{\tau}^2 \tag{A2.6}$$

$$\bar{x}'' = -\frac{1}{2}\bar{E}_1 + \frac{2\iota}{9}\bar{\tau} \tag{A2.7}$$

Here we used the same variables as in (3.2.5) – (3.2.7), $\bar{\tau} = \dfrac{\tau}{t_1}$ being the reduced electron transit time. It is now necessary to obtain a relationship between the field at the entrance electrode $\bar{E}_1$ and the injection current ι. As the first step we express $\bar{E}_1$ and ι in terms of the reduced *total* transit time $\bar{\tau}_d$. Thus eliminating $\bar{E}_1$ from (A2.7), (A2.8) and bearing in mind that at the second electrode (collector) $\bar{x}_2 = 1$, $\bar{x}_2' = 1$ and $\bar{\tau} = \bar{\tau}_d$, we obtain:

$$\iota = \frac{54}{\bar{\tau}_d^3}\left(\bar{\tau}_d - 1\right) \tag{A2.8}$$

Similarly from (A2.6) we obtain

$$\overline{E}_1 = \frac{2}{9} \imath \overline{\tau}_d = \frac{12}{\overline{\tau}_d^2}(\overline{\tau}_d - 1) \tag{A2.9}$$

where we have used (A2.8) to eliminate $\imath$. The two equations (A2.8) and (A2.9) are shown in Fig. A1; they give us the required relationship between $\overline{E}_1$ and $\imath$ in a parametric form, the parameter being the total transit time $\overline{\tau}_d$. In the absence of the magnetic field we can go a step further and eliminate $\overline{\tau}_d$ altogether obtaining a direct relationship between $\overline{E}_1$ and $\imath$ in any of three forms:

$$27\overline{E}_1^3 = (72\overline{E}_1 - 16\imath)\imath \tag{A2.10}$$

or

$$\imath = \frac{9}{4}\overline{E}_1\left(1 \mp \sqrt{1 - \frac{1}{3}\overline{E}_1}\right) \tag{A2.11}$$

or

$$\mathscr{I} = \overline{E}_1\left(1 \mp \sqrt{1 - \frac{1}{3}\overline{E}_1}\right) \tag{A2.12}$$

The above equation is shown in Fig. A2 where the electric field at the entrance electrode $\overline{E}_1$ is plotted as a function of the injection current $\imath$. As we shall see later only some parts of the above curve are of physical significance. In particular point A indicates the maximum value of the injection current $\imath = \imath_{max} = 8.0$, which leads to a stable solution

148

[3]. Similarly point B corresponds to an unstable solution for which $\bar{x}_B^{\cdot\cdot} = \bar{x}_B^{\cdot} = 0$ or in this case $\bar{\phi}_B = 0$ and $\bar{E}_B = -\left(\dfrac{d\bar{\phi}}{d\bar{x}}\right)_B = 0$ from (A2.2) and (A2.1). If we now consider a curve which is obtained by putting $\bar{x}^{\cdot} = 0$ in (A2.6), $\bar{x}^{\cdot\cdot} = 0$ in (A2.7) and then eliminate the transit time $\bar{\tau}$, we obtain

$$\bar{E}_1 = \frac{4}{3}\sqrt{\iota} \tag{A2.13}$$

The curve, is shown dotted in Fig. A2 and it crosses the original $\bar{E}_1 = \bar{E}_1(\iota)$ curve at point B.

A2.2 Distance-dependent solutions

In order to obtain solutions in terms of the distance between the electrodes we substitute (A2.2) directly in the Poisson equation by writing:

$$\frac{d^2\bar{\phi}}{d\bar{x}^2} = \frac{d^2\bar{u}^2}{d\bar{x}^2} = -\bar{\rho} = -\frac{\bar{J}_c}{\bar{x}^{\cdot}} = \frac{\mathscr{I}}{\bar{u}} \tag{A2.14}$$

Here we have used $\bar{u} = \bar{x}^{\cdot}$ for convenience of comparison with the results obtained for the more general case of $B \neq 0$. Multiplying both sides of (A2.14) by $\dfrac{d\bar{u}^2}{d\bar{x}}$ and integrating we obtain

$$\frac{1}{2}\frac{d\bar{u}^2}{d\bar{x}} = \bar{u}\frac{d\bar{u}}{d\bar{x}} = \sqrt{\mathscr{I}\,\bar{u} + C_1}$$

(A2.15)

Integrating once again we obtain

$$\frac{2}{3\mathscr{I}^2}\left\{\left(\mathscr{I}\,\bar{u} + C_1\right)^{3/2} - 2C_1\sqrt{\mathscr{I}\,\bar{u} + C_1}\right\} = \frac{2}{3\mathscr{I}^2}\sqrt{\mathscr{I}\,\bar{u} + C_1}\left(\mathscr{I}\,\bar{u} - 2C_1\right) = \bar{x} + C_2$$

(A2.16)

Now by definition $\bar{u} = 1$ when $\bar{x} = 0$ and the C_2 constant can be easily eliminated by writing:

$$\bar{x}_{\mp} = \mp\frac{2}{3\mathscr{I}^2}\sqrt{\mathscr{I}\,\bar{u} + C_1}\left(\mathscr{I}\,\bar{u} - 2C_1\right) + \frac{2}{3\mathscr{I}^2}\sqrt{\mathscr{I} + C_1}\left(\mathscr{I} - 2C_1\right)$$

(A2.17)

Here $0 \le \bar{x}_- < \bar{x}_m$ and $\bar{x}_m < \bar{x}_+ \le 1$, where $\bar{x}_m$ gives the position of the potential minimum. Since we are primarily interested in a short circuited diode, we can go a step further and obtain a direct relationship between C_1 and ι by noting that in this case $\bar{u} = \bar{u}_2 = 1$ at the exit electrode as well. We then obtain:

$$1 = \frac{4}{3\mathscr{I}^2}\sqrt{\mathscr{I} + C_1}\left(\mathscr{I} - 2C_1\right), \quad \mathscr{I} = \frac{4\iota}{9}$$

(A2.18)

As it happens the curve $\iota = \iota\left(C_1\right)$ is somewhat unwieldy and in this case it is much more convenient to use a new constants defined by writing

$$\overline{u}_m = -\frac{C_1}{\mathcal{J}}$$

(A2.19)

Substituting in (A2.19) we obtain

$$1 = \frac{2}{\sqrt{\imath}}\sqrt{1-\overline{u}_m}\left(1+2\overline{u}_m\right)$$

(A2.20)

The function $\imath\!\left(\overline{u}_m\right)$ is shown in Fig. A3 and is a cubic. We find from (A2.15) that physically the new constant $\overline{u}_m$ represents the value of velocity at the potential minimum, where $d\overline{u}^2/d\overline{x} = d\overline{\phi}/d\overline{x} = 0$.

So far we have presented well known facts [1,3] in a form which is convenient for comparing the results with and without the magnetic field, the corresponding potential distributions being shown in Fig. A4. We find that as $\imath$ increases, the field at the entrance electrode also increases until it reaches a maximum value for $\imath = 8$. This corresponds to the lower branch of the curve between the origin and point A, Fig. A2. If we attempt to increase $\imath$ beyond this point, the potential minimum drops catastrophically down to zero, forming a virtual cathode point B, which instantly moves towards the entrance electrode (anode) in order to satisfy the Poisson equation for two space-charge-limited diodes back to back; at the same time $\imath$ splits into $2\imath - \imath_2$ and $\imath_2$, only the latter part reaching the second electrode (collector). By then the continuity of $\imath$ has broken down and (A2.4) which is based on it no longer applies.

We can now interpret Fig. A2 as follows: for $0 < \iota < 4.0$ only a single value of $\bar{E}_1$ satisfies the equations; for $4.0 < \iota < 8.0$ there are two possible values of $\bar{E}_1$ but it can be shown [3] that the upper part of the curve between A and B is unstable, i.e. it can never be reached in practice; in fact the sudden formation of a virtual cathode and its shift towards the entrance electrode gives rise to hysteresis effects [1]. The importance of the dotted-curve is that all points of the $\bar{E}_1(\iota)$ curve lying above it, i.e. all points between B and the origin are of no physical significance, since by then our simple equations no longer represent the system, a virtual cathode having formed between the electrodes and ι ceasing to be continuous.

References – Appendix 1 and 2

1. C. E. Fay, A. L. Samuel and W. Shockley, On the theory of space charge between parallel plane electrodes, BSTJ vol 17, 1938, pp. 49 – 79.

2. W. J. Kleen, *Electronics of Microwave Tubes*, Academic Press, New York 1958; Section 3.6.

3. C. K. Birdsall and W. B. Bridges, *Electron Dynamics of Diode Regions*, Academic Press, New York 1966; Chapter 2 and 3.